

Monte Carlo Simulations of Systematic Effects due to Inelastic Scattering in the KATRIN Tritium Source

Diplomarbeit
von

Johannes Karl Antoni

An der Fakultät für Physik
Institut für Experimentelle Kernphysik

Erstgutachter:	Prof. Dr. G. Drexlin
Zweitgutachter:	Prof. Dr. G. Quast
Betreuender Mitarbeiter:	Dr. M. Kleesiek
Zweiter betreuender Mitarbeiter:	Dr. K. Valerius

Bearbeitungszeit: 23. März 2014 – 20. März 2015

Hiermit versichere ich, die vorliegende Arbeit selbstständig angefertigt, alle dem Wortlaut oder Sinn nach entnommenen Inhalte anderer Werke an den entsprechenden Stellen unter Angabe der Quellen kenntlich gemacht und keine weiteren Hilfsmittel verwendet zu haben.

Karlsruhe, den 20. März 2015

.....
(Johannes Antoni)

Contents

1. Introduction	1
2. Neutrino Physics	3
2.1. History	3
2.2. The Standard Model of Particle Physics	4
2.3. Neutrino Oscillation	5
2.3.1. Mass Hierarchies	6
2.4. Neutrino Mass Experiments	6
2.4.1. Model-Dependent Neutrino Mass Measurements	7
2.4.2. Cosmological Neutrino Mass Determination	7
2.4.3. Direct Neutrino Mass Measurements	8
3. The Karlsruhe Tritium Neutrino (KATRIN) Experiment	11
3.1. The Measurement Principle	11
3.2. The Experimental Setup of the KATRIN Experiment	13
3.2.1. The Source and Transport Section (STS)	14
3.2.2. The Spectrometers and Detector Section (SDS)	15
3.3. Analytic Description of the Experiment	16
3.3.1. The Integrated Spectrum	17
3.3.2. The Transmission Function	17
3.3.3. The Energy Loss Function	19
3.3.4. The Response Function	22
3.3.5. Properties of the Rearsection Electron Gun	24
3.3.6. Unfolding of the Response Function	26
4. The KASPER Software Framework	27
4.1. SSC	27
4.1.1. Improved Calculation of Scattering Probabilities	28
4.2. KAFIT	29
4.2.1. The SPECTRUMSIMULATOR	29
4.2.2. The RUNGENERATOR	30
4.2.3. The FITTER	30
4.2.4. Ensemble Simulations	31
4.2.5. The Measuring Time Distribution	34
4.3. KASSIOPEIA	34
4.3.1. The Simulation of Scattering	36
5. Systematic Effects of Scattering in the WGTS	39
5.1. The Influence of σ_{inel} on the Neutrino Mass Measurement	39

5.2.	Required Precision of a Measurement of σ_{inel}	40
5.3.	Influence of the Analysis Interval on Systematic Effects	43
5.4.	Recommended Analysis Intervals	48
5.5.	Conclusion and Outlook	51
6.	Simulation of Electron Gun Measurements	53
6.1.	The Response Function of the Electron Gun	53
6.2.	Simulation of Electron Gun Response Functions	56
6.2.1.	Simulation Parameters	56
6.2.2.	Simulation Design	57
6.2.3.	Simulation Results	59
6.3.	Deriving the Total Inelastic Cross Section	62
6.4.	Conclusion and Outlook	66
7.	Conclusion and Outlook	67
8.	German Summary	71
8.1.	Einleitung	71
8.2.	Neutrino-physik	72
8.3.	Das KARlsruher TRitium Neutrino (KATRIN) Experiment	73
8.4.	Die KASPER Softwareumgebung	73
8.5.	Systematische Effekte von Streuung in der WGTS	74
8.6.	Simulation von Messungen mit der Elektronenkanone	75
8.7.	Ausblick	75
	Bibliography	77
	Appendix	83
A.	Measuring Time Distributions	83
B.	Kassiopeia Configuration Files	93
	Acknowledgments	109

1. Introduction

The postulation of the neutrino in 1930 [Pau30] marks the start of a whole new field of physics. Although W. Pauli worried that he might have predicted a particle that could never be detected, three types of neutrinos have been discovered so far. Through manifold evidence for the existence of neutrino flavor oscillations [Wen10], [Aha13] neutrinos are also known to have a non-vanishing, yet unknown, mass.

In the quest for measuring the neutrino mass, many experimental approaches are currently pursued. Cosmological models based on observations of large scale structures in the universe have been able to set upper limits to the sum of light neutrino masses. However, these results strongly depend on the complexity of the model and the data used. Lowest upper limits on the sum of light neutrino masses go down to 0.23 eV [Pla13]. Another approach is the search for the neutrinoless double β -decay. The detection of such a decay would allow to infer information on the neutrino mass. However, the existence of this decay mode depends on the assumption that neutrinos are of Majorana type. Model-independent neutrino mass measurements do not require the neutrino to be of either Majorana or Dirac type. Experiments of this type based on the kinematics of β -decay in Mainz [Kra05] and Troitsk [Ase11] have set up upper limits of 2.3 eV and 2.05 eV, respectively, for the mass of the electron antineutrino.

The KATRIN experiment presently under construction at the Karlsruhe Institute of Technology is a next generation neutrino mass experiment with the goal of improving the neutrino mass sensitivity of direct measurements to 0.2 eV at 90 % C.L.. The setup of the KATRIN experiment is similar to previous experiments in Mainz and Troitsk which used a so-called MAC-E filter as a spectrometer to measure the electron energy spectrum of the tritium β -decay. Nevertheless, the ambitious goal of increasing the neutrino mass sensitivity by one order of magnitude requires a large and technically complex experimental setup. This also means that statistical and systematic uncertainties have to be controlled meticulously. Due to the measurement principle KATRIN is based on, they even have to be reduced by two orders of magnitude, compared to predecessor experiments. The experimental setup can be divided into two functional units: the source section delivering a large β -decay activity, and the spectrometer and detector section which is responsible for the precise

measurement of the beta-decay spectrum.

One of the parts of the Source and Transport Section is the Windowless Gaseous Tritium Source (WGTS). Electrons are emitted here and transported to the spectrometer and the detector. On their way, they may scatter off the gaseous tritium in the source and lose energy. Any unaccounted for energy loss of the signal electrons will cause a systematic uncertainty on the determination of the neutrino mass. Apart from the column density of the tritium gas, the major factor determining the energy loss due to inelastic scattering is the total inelastic scattering cross section. It is included in the model of the integrated β -spectrum at KATRIN which will be fitted to measured data. Currently, the absolute value for the total inelastic scattering cross section is based on a measurement at the Troitsk experiment where a gaseous tritium source has been used, too [Ase00].

However, the accuracy of the current value is not sufficient to meet the KATRIN design goal [KC05]. Therefore, a calibration measurement using an electron gun is planned in order to determine the total inelastic scattering cross section sufficiently well. It is the first aim of the work at hand to quantify how precise such a measurement has to be. For this purpose, Monte Carlo simulations have been performed.

The second aim of the work at hand builds upon the requirements set for the precision of the total inelastic scattering cross section. Through Monte Carlo particle tracking simulations, the calibration measurement of the electron gun is simulated. Based upon the simulation of various angles and energy spreads of the electron gun as well as various column densities in the source, recommendations for the settings under which the electron gun should be operated are given. Above this, the duration of such calibration measurements is estimated.

This work is structured as follows: chapter 2 gives an overview on the field of neutrino physics with a focus on topics which are of special interest for KATRIN. It concludes with an overview on current neutrino mass experiments and gives an outlook to future efforts. Chapter 3 describes the KATRIN experiment itself. This chapter is subdivided into a description of the technical setup and an analytic description of the experimental setup. Chapter 4 explains the KASPER software framework which has been used and extended in the course of this work. The chapter includes a description of the concept of measuring time distributions which are important for studies performed in the following chapter. In chapter 5 the systematic influence of the total inelastic scattering cross section is analyzed. This chapter also gives an estimate to what precision this parameter should be known in order to meet the requirements on systematic uncertainties of the technical design report of KATRIN. In the following chapter 6 simulations of the Rearsection electron gun are explained and recommendations on how it should be used in future calibration and monitoring measurements are given. Chapter 7 presents conclusions and gives an outlook on further research.

2. Neutrino Physics

Postulated and discovered during the 20th century (see section 2.1) neutrinos have accompanied the formation of the field of particle physics. Hence, these particles play a major role in the standard model (see section 2.2). However, there is overwhelming evidence that the way neutrinos are described in the standard model, especially their treatment as massless particles, has to be reconsidered (see section 2.3). The KATRIN experiment is only one out of many experiments which search for a better understanding of the neutrino mass (see section 2.4).

2.1. History

The experimental finding that the spectrum of β -decay is continuous (which has first been measured around 1914¹ [Cha14]) cannot be explained when the process is considered a two-body problem formed by the emitted electron and the nucleus. In fact, this would violate the conservation of energy and momentum. In 1930 W. Pauli suggested a way out of this dilemma by postulating the neutrino [Pau30]. Taking this particle into account the β -decay becomes a three-body problem with the decay energy being distributed to the kinetic energy and mass of the electron and the neutrino.

It took the physics community about 25 years to verify Pauli's hypothesis in the scope of the so-called "Poltergeist" experiments [Rei56]. The experimenters used electron antineutrinos emitted by a nuclear reactor to induce an inverse β -decay:

$$\bar{\nu}_e + p^+ \rightarrow n + e^+ . \quad (2.1)$$

The positron from the decay quickly finds a free electron and annihilates into two photons. The delayed coincidence between this signal and the signal of the photon emitted after the capture of the neutron by ^{108}Cd in the target material served as signature for the inverse β -decay. By detecting all three of these signals, the first neutrinos ever were detected, in this case, electron antineutrinos.

¹The first reporting of continuous β -decay spectra triggered a long debate in the physics community whether the β -decay spectrum is continuous or discrete. This controversy was not cleared out until the late 1920s [Ell27].

In 1962, a second type of neutrino, the muon neutrino, was discovered at the Brookhaven Alternating Gradient Synchrotron [Dan62]. The pion-decay

$$\pi^+ \rightarrow \mu^+ + \nu_\mu \quad (2.2)$$

was used to produce muon neutrinos. Assuming that these neutrinos are the same as electron neutrinos, they should react with protons and neutrons to produce electrons and muons. However, only the latter were detected at the experiment showing that muon neutrinos and electron-neutrinos are different particles and that there are so-called families of electrically charged and uncharged leptons. Thus, the second type of neutrino (or “neutrino flavor”), the muon-neutrino had been discovered.

Since the late 1980s, experiments at the Large Electron Positron Collider (LEP) at CERN had shown that there is most likely a total of three neutrino flavors [LEP06]. Later experiments confirmed these results so that the discovery of a third neutrino was merely a question of time. This discovery was finally made in 2000 at the DONUT experiment [Kod01]. Here, the decay of D_s -mesons

$$D_s \rightarrow \tau^- + \bar{\nu}_\tau \quad (2.3)$$

was used to generate tauons and tau antineutrinos. The tauons and further decay products of the meson decay were blocked by 36 m of shielding so that only the barely interacting tau antineutrinos could pass. After the shielding the tau antineutrinos were used to likewise generate tauons. The detection of these tauons was the proof for the existence of the tau neutrino.

2.2. The Standard Model of Particle Physics

Neutrinos are part of the so-called standard model of particle physics which summarizes all known elementary particles. An illustration of the standard model can be seen in figure 2.1.

Fermionic matter depicted on the left hand side is divided into quarks and leptons. Fermions have a spin of $S = \frac{1}{2}$. On the right hand side fermionic anti-matter is depicted, comprising of anti-quarks and anti-leptons. Furthermore, quarks and leptons (and their anti-particles) can be categorized into three generations (sometimes also called families). In the middle, there are the so-called gauge bosons which describe interactions among elementary particles. They are bosons and therefore have integer spins. These are $S = 1$ for all gauge bosons except for the Higgs-boson with $S = 0$.

The up-, charm- and top-quarks have an electric charge of $\frac{2}{3}e$ while their respective corresponding anti-particles are charged with $-\frac{2}{3}e$. Here, e is the elementary electric charge, the charge of an electron. The down-, strange- and bottom-quark are charged with $\frac{1}{3}e$ and their corresponding anti-particles are charged with $-\frac{1}{3}e$.

The gauge bosons represent (apart from gravitation) the known types of interaction: Photons (γ) mediate the electromagnetic force between charged particles. Gluons (g) mediate strong interactions between particles with color charge (quarks and antiquarks). W^\pm - and Z^0 -bosons mediate interactions between particles with weak charge. Additionally, the Higgs-boson is also part of the standard model. It is part of the Higgs mechanism [Hig64], [Eng64] which explains why the W^\pm - and Z^0 -bosons

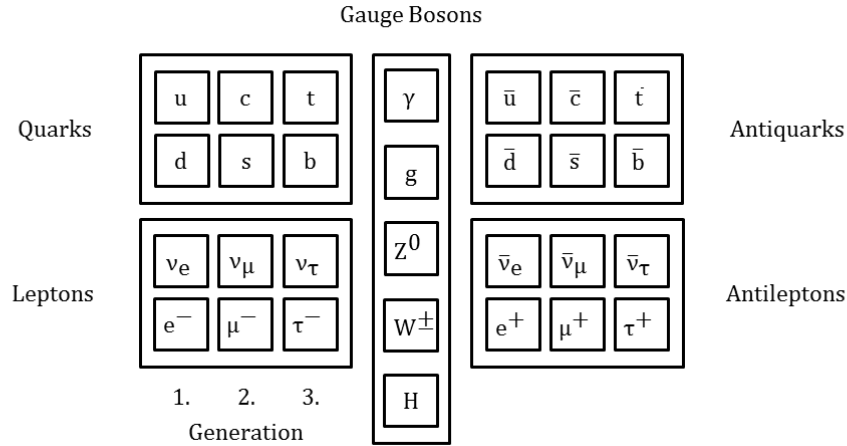


Figure 2.1.: **The standard model of particle physics.** The illustration shows the ordering principle of the standard model of particle physics.

have a mass while the photon stays massless and why other elementary particles with a mass are not massless. The Higgs-boson has been discovered at CERN in 2012 [CC12], [AC12], which was a milestone for particle physics and rewarded with the Nobel Prize for P. Higgs and F. Englert in 2013.

2.3. Neutrino Oscillation

Due to solar fusion processes, the sun is a strong neutrino source. Since they are barely interacting, these particles are considered ideal messengers to validate theories about the solar fusion processes. However, when the Homestake experiment [Dav94] set out to measure the solar neutrino flux, it turned out to be significantly lower than predicted, e. g. [Bah68]. The experiment thereby raised the so-called “solar neutrino problem”.

One explanation was offered by the concept of neutrino oscillation which was predicted by B. Pontecorvo [Pon67]. Further work on this topic was carried out by Z. Maki, M. Nakagawa and S. Sakata [Mak62] which is why the matrix aggregating their work is called the PMNS-matrix:

$$\begin{pmatrix} |\nu_e\rangle \\ |\nu_\mu\rangle \\ |\nu_\tau\rangle \end{pmatrix} = \begin{pmatrix} U_{e1} & U_{e2} & U_{e3} \\ U_{\mu1} & U_{\mu2} & U_{\mu3} \\ U_{\tau1} & U_{\tau2} & U_{\tau3} \end{pmatrix} \begin{pmatrix} |\nu_1\rangle \\ |\nu_2\rangle \\ |\nu_3\rangle \end{pmatrix}. \quad (2.4)$$

The PMNS-matrix with the unitary matrix U shows how neutrino flavor eigenstates ($|\nu_e\rangle, |\nu_\mu\rangle, |\nu_\tau\rangle$) are related to the neutrino mass eigenstates ($|\nu_1\rangle, |\nu_2\rangle, |\nu_3\rangle$).

Simplified for only two neutrino generations and two neutrino mass states the PMNS matrix simplifies to

$$\begin{pmatrix} |\nu_e\rangle \\ |\nu_\mu\rangle \end{pmatrix} = \begin{pmatrix} \cos \theta & \sin \theta \\ -\sin \theta & \cos \theta \end{pmatrix} \begin{pmatrix} |\nu_1\rangle \\ |\nu_2\rangle \end{pmatrix}. \quad (2.5)$$

Neutrino oscillation is then shown by

$$|\nu_e(t)\rangle = \cos \theta e^{-iE_{\nu_1}t/\hbar} |\nu_1\rangle + \sin \theta e^{-iE_{\nu_2}t/\hbar} |\nu_2\rangle \quad (2.6)$$

with E_{ν_i} the neutrino energy and the mixing angle θ . However, the entire concept only holds if neutrinos have a mass and if it differs for at least two neutrinos. Therefore, the evidence of neutrino oscillation is an indirect proof for neutrinos having a non-vanishing mass.

Sticking with the example of two neutrino flavors the probability of an electron neutrino to convert into a muon neutrino after having covered a distance L is

$$P(\nu_e \rightarrow \nu_\mu) = \sin^2(2\theta) \sin^2\left(\frac{\Delta m^2 L}{4E}\right). \quad (2.7)$$

Early experiments which analyzed neutrino oscillation chose the oscillation length L too low for the respective energy range to allow for a conversion of one flavor to another. They therefore failed to see the effect [Mac05]. Proof for neutrino oscillations was finally found by the Super-Kamiokande- [Wen10] and the SNO-experiment [Aha13]. This raises the need for an extension of the standard model where neutrinos are still considered to be massless.

2.3.1. Mass Hierarchies

Based on the observation of neutrino oscillations it is only possible to measure the differences (“mass splittings”) between squared neutrino masses

$$\Delta m_{ij}^2 = m_i^2 - m_j^2 \quad (2.8)$$

with $i, j = 1, 2, 3$. As they dominate solar neutrino oscillations, the first mass splitting Δm_{12}^2 and the corresponding mixing angle θ_{12} are usually referred to as “solar”. The same holds for Δm_{23}^2 and θ_{23} which govern the oscillation of atmospheric neutrinos and therefore are referred to as “atmospheric”.

Since neutrino oscillations only allow for calculations of the mass splittings, it is still unknown if the neutrino mass eigenstates are quasi degenerate, i. e. almost equal

$$m_1 \approx m_2 \approx m_3 \quad (2.9)$$

or if they can be ordered hierarchically. Furthermore, for Δm_{23}^2 only the absolute value can be determined. Therefore, in the case of hierarchical ordering, two principles are possible. Masses can be ordered either hierarchically

$$m_1 \ll m_2 < m_3 \quad (2.10)$$

with m_1 being the lowest neutrino mass. Or they can be ordered according to an “inverse” hierarchy

$$m_3 \ll m_1 < m_2 \quad (2.11)$$

with m_3 being the lowest neutrino mass.

2.4. Neutrino Mass Experiments

The following three subsections describe various experiments which are currently investigating the neutrino mass. There are so-called model-dependent experiments which require the neutrino to be of Majorana type (see subsection 2.4.1), cosmological approaches (see subsection 2.4.2) and direct neutrino mass experiments such as KATRIN itself (see subsection 2.4.3).

2.4.1. Model-Dependent Neutrino Mass Measurements

Currently, experiments like GERDA [Abt04], EXO-200 [EXO14], NEMO-3 [Arn14] and CUORICINO [And11] are searching for the neutrinoless double β -decay ($0\nu\beta\beta$). This is a theoretical decay where two neutrons in the same nucleus are simultaneously converted into two protons without the emission of any neutrinos ($0\nu\beta\beta$)

$$(A, Z) \rightarrow (A, Z + 2) + e_1^- + e_2^- . \quad (2.12)$$

Here, A is the nuclear mass number and Z is the nuclear charge. The process is strongly suppressed and would produce a discrete peak at the end of the continuous energy spectrum of the ($2\nu\beta\beta$)-decay. This is the same process as in equation 2.12 but with the emission of two neutrinos

$$(A, Z) \rightarrow (A, Z + 2) + e_1^- + e_2^- + \bar{\nu}_{e1} + \bar{\nu}_{e2} . \quad (2.13)$$

The detection of the ($0\nu\beta\beta$)-peak would be strong evidence for the neutrino being of Majorana type. Neutrinos of Dirac type as they are currently described in the standard model fail to explain the process.

Furthermore, the detection of the ($0\nu\beta\beta$)-peak could be used for a determination of the neutrino mass. This approach is called model-dependent as it requires neutrinos to be of Majorana type. The decay rate for the neutrinoless double β -decay is

$$\Gamma^{0\nu} = G^{0\nu}(E_0, Z) |M_{\text{GT}}^{0\nu} - \frac{g_V^2}{g_A^2} M_{\text{F}}^{0\nu}|^2 \langle m_{\beta\beta} \rangle^2 . \quad (2.14)$$

Here, $G^{0\nu}(E_0, Z)$ is the phase space integral, $M_{\text{GT}}^{0\nu}$ the nuclear matrix element for Gamov-Teller transitions and $M_{\text{F}}^{0\nu}$ the nuclear matrix element for Fermi transitions. g_V and g_A are the vector- and axial-vector weak coupling constants. The calculation of the nuclear matrix elements is a challenge to experimental as well as to theoretical physicists. Finally, $\langle m_{\beta\beta} \rangle^2$ is the effective Majorana neutrino mass. It comprises of a sum over light neutrinos

$$\langle m_{\beta\beta} \rangle = \left| \sum_i |U_{ei}|^2 m_{\nu i} e^{i\alpha_i} \right| \quad (2.15)$$

with the mixing matrix U (see equation 2.4) and so-called Majorana phases α_i . These phases can lead to a cancellation of terms which could result in a situation where $\langle m_{\beta\beta} \rangle$ is smaller than any of the neutrino mass eigenstates [Aal04]. Under consideration of measured values of the three neutrino mixing angles and calculations for nuclear matrix elements upper limits for the three possible mass ordering scenarios can be calculated. The first phase of the GERDA experiment has set an upper limit between 0.2 and 0.4 eV for the effective Majorana neutrino mass [Ago13].

2.4.2. Cosmological Neutrino Mass Determination

Due to their non-vanishing mass, neutrinos play an important role in the evolution of large-scale structures in the universe. A broad overview on this field is given by [Les06] and summarized in this subsection. As so-called hot dark matter (HDM),

neutrinos have an influence on the formation of cosmological perturbations. Therefore, it is possible to use cosmological observations to draw conclusions on the upper limit of the sum of light neutrinos

$$m_{\text{tot}} = \sum_i m_{\nu_i} . \quad (2.16)$$

However, these conclusions are not only dependent on the combination of the individual data sets used for the analysis but also model-dependent in the sense that best-fits for the neutrino mass strongly depend on the underlying multi-parameter cosmological model.

One approach for cosmological fits is the analysis of small anisotropies in the cosmic microwave background radiation (CMB). In this approach the influence of the neutrino mass (especially if it is smaller than approximately 0.5 eV) is very weak so that the effect can easily be veiled by instrumental noise. Nevertheless, by using CMB data alone, the WMAP satellite experiment was able to set an upper limit on the sum of light neutrino masses of 1.3 eV. Taking further data into account, the limit was even pushed down to 0.3 eV [Kom11]. The Planck Collaboration set an upper limit of 0.93 eV using their own and CMB data from WMAP. Furthermore, they were able to push this limit to as low as 0.23 eV when taking into account other than solely CMB data [Pla13]. However, it is important to again emphasize the model-dependence of these results.

Another method to derive neutrino masses from cosmological observations is the analysis of galaxy redshifts. Due to their non-vanishing mass, neutrinos can influence the formation of cosmological structures at intermediate scales. Therefore, it is possible to use redshift surveys, i.e. surveys which map the 3-D distribution of remote galaxies, in order to draw conclusions on the neutrino mass. Research on this field has been conducted, for example, by the 2 degree field (2dF) galaxy redshift survey [Col05] and the Sloan Digital Sky Survey (SDSS) [Ahn14]. Redshift data is frequently used as auxiliary data in combination with CMB-data.

Finally, in order to find upper boundaries for the neutrino mass, photons emitted by quasars are analyzed. Due to the expansion of the universe, seen from earth, these photons are redshifted and get absorbed by neutral hydrogen clouds on their way to earth. Seen from earth, the hydrogen clouds are redshifted at various degrees themselves. As a consequence, on earth, multiple different redshifted absorption lines are observed. Since these are Lyman- α absorptions and since there are so many different ones of them, the lines in the spectrum form a so-called Lyman- α forest. Through a thorough analysis of the absorption lines it is possible to draw conclusions on density fluctuations and therefore on possible influences of a neutrino mass. By applying this method, an upper limit of 5.5 eV has been set [Cro99].

2.4.3. Direct Neutrino Mass Measurements

The measurement principle of direct neutrino mass experiments solely relies on purely kinematical observations of the endpoint of β -decay electron spectra. Furthermore, these experiments do not require the neutrino mass to be of either Majorana or Dirac type and are therefore called model-independent. The following two paragraphs give an insight into two direct neutrino mass measurements experiments before chapter 3 focuses on KATRIN.

The Electron Capture ^{163}Ho Experiment (ECHO)

For the determination of the neutrino mass, the **Electron Capture ^{163}Ho experiment (ECHO)** aims to use the calorimetric measurement of the energy spectrum of the electron capture of ^{163}Ho as suggested by [De 82]. This is different from the KATRIN approach where the β -decay electron spectrum of tritium is used. In the process of electron capture, an electron from an inner atomic shell is captured by the nucleus where a proton is converted into a neutron under the emission of an electron neutrino

$$p + e^- \rightarrow n + \nu_e . \quad (2.17)$$

After this process, the atom is left in an excited state. The energy spectrum for the disexcitation-process is

$$\frac{dN}{dE_C} = A(Q_{\text{EC}} - E_C)^2 \sqrt{1 - \frac{m_{\nu_e}^2}{(Q_{\text{EC}} - E_C)^2}} \sum C_{\text{H}} n_{\text{H}} B_{\text{H}} \phi_{\text{H}}^2(0) \frac{\frac{\Gamma_{\text{H}}}{2\pi}}{(E_C - E_{\text{H}})^2 + \frac{\Gamma_{\text{H}}^2}{4}} . \quad (2.18)$$

The term on the right of the equation shows a Breit-Wigner resonance with a width Γ_{H} at approximately the binding energy of the captured electron E_{H} . The index H indicates from which level the electron has been captured. The nuclear shape factor C_{H} , the fraction of occupied states at the H-th level n_{H} , the squared wave-function of the captured electron at the nucleus $\phi_{\text{H}}^2(0)$ and the correction factor B_{H} determine the intensity of the Breit-Wigner resonances. $\phi_{\text{H}}^2(0)$ can be seen as the probability to find the electron at the position of the nucleus. Q_{EC} is the energy available for the decay. It is given by the mass difference between the mother and daughter nucleus. $m_{\nu_e}^2$ is the squared neutrino mass which according to equation 2.4 comprises from the neutrino mass eigenvalues through

$$m_{\nu_e}^2 = \sum_i |U_{ei}|^2 m_{\nu_i}^2 . \quad (2.19)$$

A is a constant factor comprising electroweak interactions which can be considered as constant in the energy regions analyzed at ECHO. ECHO wants to gain a thorough understanding of the electron capture process for ^{163}Ho . By using so-called metallic magnetic calorimeters (MMCs), which are operated below < 100 mK, the energy spectrum can be measured. Finally, the spectrum model for ^{163}Ho can be fitted to the measured data in order to obtain the squared neutrino mass. By running the experiment at full scale, a sensitivity in the sub-eV-range is aimed for as a long-term perspective [Gas14].

Further direct neutrino mass experiments using β -spectra of molecules other than tritium include HOLMES (like ECHO based on the electron capture decay of ^{163}Ho) [Alp15] and MARE (based on the β -decay of ^{187}Re) [Mon06].

The Project 8 Experiment

As it will be shown in the following chapter, the measurement of the electron energy spectrum of tritium β -decay can be used to infer the neutrino mass. The Project 8 experiment intends to use a spectroscopy approach based on the detection of

cyclotron radiation. Electrons emitted by tritium gas in a solenoidal magnetic field start a cyclotron motion around the field lines and emit cyclotron radiation at a frequency of

$$\omega = \frac{eB}{E_{\text{kin,e}} + m_e} . \quad (2.20)$$

This radiation will be detected by a very sensitive antenna array and allows to infer the energy of the electron [Mon09]. Preliminary measurements with ^{83m}Kr have succeeded in measuring the energy of single electrons through the detection of cyclotron radiation. Results showed the decrease in energy due to cyclotron radiation and due to scattering of the electron off residual gas molecules [Asn14].

While Project 8 is an experiment at a very early stage, other experiments using the β -decay of tritium have set up the lowest upper limits on the neutrino mass in direct and model-independent measurements so far. These are the experiments in Mainz [Kra05] and Troitsk [Ase11] which are in their setup very similar to the KATRIN experiment which is explained in the following chapter.

3. The Karlsruhe TRitium Neutrino (KATRIN) Experiment

As the next generation direct neutrino mass measurement experiment using β -decay, KATRIN is designed to improve the neutrino mass sensitivity by one order of magnitude. This requires a demanding technical setup of the experiment as well as sophisticated analytic tools to extract the squared neutrino mass from a measured β -decay energy spectrum. In section 3.1 this chapter starts with an overview on the measurement principle KATRIN is based on. In the following section 3.2 the experimental setup is described. An analytic description of the experiment is necessary (section 3.3) to allow for an estimation of the squared neutrino mass by fitting the analytic model to measured data. Further details on this procedure can be found in section 4.2.

3.1. The Measurement Principle

Currently, the most sensitive experiments for measuring the neutrino mass in Mainz [Kra05] and Troitsk [Ase11] are based on the analysis of the electron energy spectrum of tritium β -decay. These experiments as well as KATRIN comprise of a tritium source, an energy filter and a detector which are spatially separated and connected through an electromagnetic transport system. The electrons emitted in the source are filtered by the electromagnetic energy filter. Therefore, the detector only has to record a count rate. The separation of source and detector allows to use an electromagnetic energy filter of unprecedented energy resolution for measuring the electron energy spectrum.

The shape of the electron energy spectrum looks different for a scenario with a vanishing and for a scenario with a non-vanishing neutrino mass (see figure 3.1). Consequently, a thorough understanding of the electron energy spectrum is of utmost

importance. The energy spectrum for the β -decay electrons is given by

$$\frac{d\dot{N}}{dE} = C \cdot F(Z, E) \cdot p \cdot (E + m_e c^2)(E_0 - E) \sqrt{(E_0 - E)^2 - m_\nu^2} \cdot \Theta(E_0 - E - m_\nu) . \quad (3.1)$$

Here, \dot{N} is the count rate of electrons, E is the kinetic energy of an electron with mass m_e and a momentum of p . E_0 is the endpoint energy which is the maximum energy an electron can have in case that the kinetic energy of the neutrino is close to zero. $F(Z, E)$ represents the Fermi function which considers Coulomb interactions of the outgoing electron. The step function $\Theta(E_0 - E - m_\nu)$ is included to ensure the conservation of energy. Finally, C is given by

$$C = \frac{G_F^2}{2\pi^3} \cos^2 \theta_C |M|^2 \quad (3.2)$$

and comprises the Fermi constant G_F , the Cabibbo angle θ_C and the nuclear matrix element M [KC05]. It is due to the structure of formula 3.1 that later fitting procedures to measured data (see section 4.2) will only yield a squared neutrino mass m_ν^2 . According to equation 2.4 this is a weighted sum over neutrino mass eigenvalues

$$m_{\nu_e}^2 = \sum_i |U_{ei}|^2 m_{\nu_i}^2 . \quad (3.3)$$

For reasons of readability, the following chapters will usually only use the expression m_ν^2 instead of $m_{\nu_e}^2$.

The analysis of β -decay spectra has two major advantages compared to other methods of neutrino mass determination (see section 2.4): first, the analysis of β -decay spectra is model-independent in the sense that the measurement principle is applicable to both, Dirac or Majorana type neutrinos. Second, it is a direct measurement which means that only well-understood kinematic processes are involved. Furthermore, tritium is an almost ideal β -emitter for neutrino mass measurements [Sch14], [Bor08]:

- The β -decay of tritium is super-allowed and the nuclear matrix element M is energy independent which simplifies calculations of the energy spectrum.
- The endpoint energy of tritium $E_0 \approx 18.6$ keV is relatively low. Therefore, count rates close to the endpoint are higher than for β -emitters with a wider energy spectrum.
- The relatively short half life of tritium of 12.3 y leads to a high specific activity. This decreases scattering probabilities in the source compared to β -emitters with a lower specific activity.
- The low nuclear charge of tritium decreases scattering probabilities in the source.
- Tritium has a comparatively simple and therefore well-understood atomic shell structure.

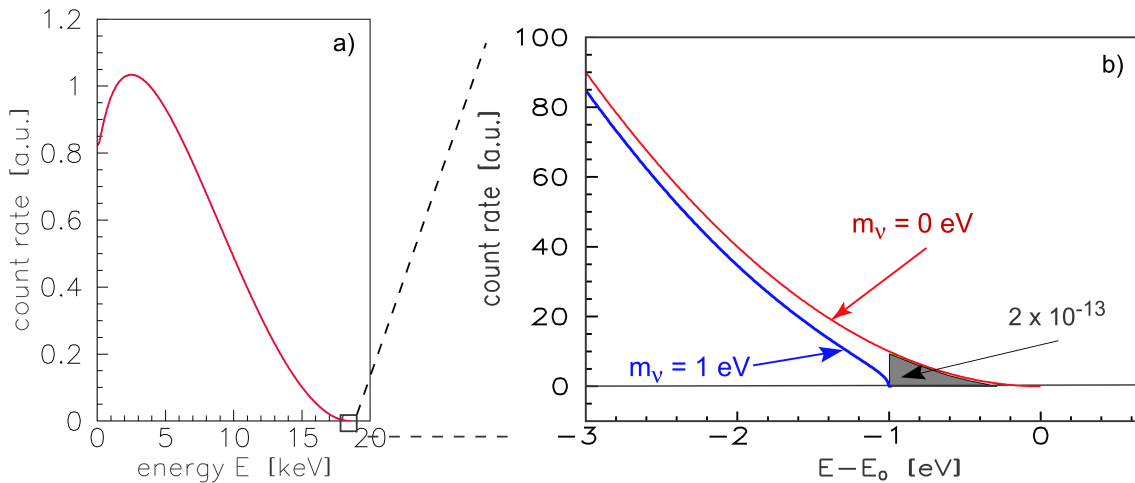


Figure 3.1.: **The differential electron energy spectrum for tritium β -decay.**

This illustration depicts the electron energy spectrum for tritium β -decay for the case of a neutrino mass of $m_\nu = 1$ eV and for the case of $m_\nu = 0$ eV. The graph on the right (b) highlights the important region close to the endpoint where the signature of a non-vanishing neutrino mass is most pronounced. It is important to note that KATRIN will not measure a differential but an integrated spectrum due to the usage of an integrating spectrometer (see subsection 3.3.1). Illustration taken from [KC05].

The analysis of tritium β -spectra has led to the so far most precise model-independent neutrino mass measurements at the Mainz experiment [Kra05]

$$m_{\nu_e} < 2.3 \text{ eV (95 \% C. L.)} \quad (3.4)$$

and the Troitsk experiment [Ase11]

$$m_{\nu_e} < 2.05 \text{ eV (95 \% C. L.)} . \quad (3.5)$$

It is the design goal of the KATRIN experiment [KC05] to improve the neutrino mass sensitivity by one order of magnitude to

$$m_{\nu_e} < 0.2 \text{ eV (90 \% C. L.)} . \quad (3.6)$$

Since the measured parameter is the squared neutrino mass $m_{\nu_e}^2$ the sensitivity on the parameter itself even has to be improved by two orders of magnitude.

3.2. The Experimental Setup of the KATRIN Experiment

The KATRIN experiment uses a similar setup as its predecessor experiments in Troitsk and Mainz. However, to achieve the ambitious sensitivity goal, the dimensions of KATRIN significantly exceed the dimensions of the latter. The full KATRIN setup will measure 70 m in length and on its widest point the main spectrometer has a diameter of 10 m. The complete setup as depicted in figure 3.2 can be broken

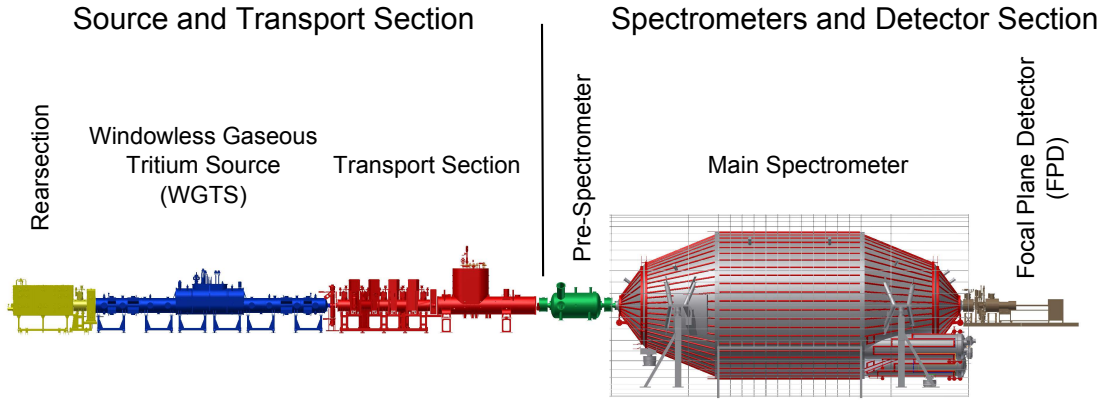


Figure 3.2.: **The setup of the KATRIN experiment.** This illustration based on [KC05] depicts the main components and sections of the KATRIN experiment.

down into the Source and Transport Section (STS) (see subsection 3.2.1) and the Spectrometers and Detector Section (SDS) (see subsection 3.2.2). These sections can be subdivided into further parts which are described in the respective subsections. While many aspects of the experiment have been optimized over time, the basic setup of the KATRIN experiment still follows the technical design report [KC05] and is explained in the following sections.

3.2.1. The Source and Transport Section (STS)

The Source and Transport Section (STS) can be subdivided into the Windowless Gaseous Tritium Source (WGTS), the Rearsection and the transport section which are explained in the following subsections.

The Windowless Gaseous Tritium Source (WGTS)

In order to achieve sufficient count rates on the detector, the KATRIN experiment requires a tritium source of sufficient activity with as low as possible systematic uncertainties. For this purpose, the neutrino mass experiment in Mainz [Bon01] has used quench condensed tritium. However, due to systematic effects like self-charging of the tritium film [Bor03] this source type is not used at KATRIN. Instead, KATRIN is operated with a gaseous tritium source. This concept has been pioneered at Los Alamos [Wil87] and at Troitsk [Bel95].

The Windowless Gaseous Tritium Source is a cylindrical tube of 10 m length and a diameter of 90 mm to which gaseous tritium of high purity is injected at the center. A magnetic field of $B_S = 3.6$ T is generated by superconducting magnets throughout the entire source to guide the β -electrons to the transport section which is connected to the main spectrometer. In the transport section, a highly sophisticated pumping system is required in order to avoid any contamination of the main spectrometer with tritium and yet allow for the unhindered transport of electrons.

The source is operated at a temperature of 27 – 30 K to minimize any Doppler-effects at higher temperatures while keeping the tritium in its gaseous phase. At an injection pressure of tritium to the WGTS of $3.4 \cdot 10^{-3}$ mbar this corresponds to a column density of $\rho d = 5 \cdot 10^{17}$ cm⁻². The column density and the total inelastic

scattering cross section σ_{inel} are the most important parameters defining scattering and energy loss of the signal electrons in the WGTS.

The Rearsection

The Rearsection of the KATRIN experiment is attached to the WGTS on the opposite side of the transport section and the main spectrometer. It is designed to fulfill several important calibration and monitoring tasks for the KATRIN experiment (a detailed description can be found in [Bab14]). An especially important component for the work at hand is the Rearsection electron gun which can be used to monitor the column density in the WGTS and to determine the total inelastic scattering cross section of tritium. The determination of the total inelastic scattering cross section from electron gun measurements is simulated in chapter 6. Key parameters for the simulation of the electron gun in that chapter are described in subsection 3.3.5.

The Transport Section

The transport section fulfills three main objectives. First, it reduces the gas flow from the WGTS to the spectrometers. By setting up the gas tubes as a chicane, a direct line from the WGTS to the spectrometer is prohibited which ensures that neutral molecules hit the walls at least six times and can be pumped off. Four turbomolecular pumps in the differential pumping section (DPS) are designed to achieve a gas flow reduction by the order of 10^5 . Preliminary simulations have yielded a factor of $2.5 \cdot 10^4$ [Luk12]. An additional reduction by the order of at least 10^7 is supposed to be achieved by cryogenic pumps (CPS). Recent investigations show that an increase of this factor to 10^{10} is possible [Jan15]. Second, the transport section has to adiabatically guide electrons from the source to the spectrometer section. For this purpose, superconducting magnets are used. However, this guiding effect also applies to charged ions from the source. To avoid these ions from entering the spectrometer is the final requirement on the transport section. For this, a dipole system is implemented at the DPS. It is supposed to reflect ions (but not electrons) from the WGTS and protects the spectrometers from contamination [Win11].

3.2.2. The Spectrometers and Detector Section (SDS)

The Spectrometers and Detector Section (SDS) can be subdivided into the pre-spectrometer, the main spectrometer and the focal plane detector (FPD) which are explained in the following subsections.

The Pre-Spectrometer

The pre-spectrometer operates at a potential of about +300 V relative to the main spectrometer and is designed to block the low-energy bulk of the β -spectrum which bears little information on the neutrino mass. For this purpose, it reduces the flux of electrons by a factor of approximately 10^6 . The reduced amount of electrons limits the risk of interactions and therefore background effects in the main spectrometer. The functionality principle of the pre-spectrometer very much resembles the main spectrometer. However, it is significantly smaller and has an energy resolution of $\Delta E = 100 \text{ eV}$.

The Main Spectrometer

The KATRIN main spectrometer works according to the MAC-E filtering principle which has originally been proposed by [Bea80]. The acronym stands for “magnetic adiabatic collimation with an electrostatic filter” which summarizes the concept illustrated in figure 3.3: electrons in the WGTS are emitted isotropically and their momentum can be split into a longitudinal and a perpendicular component relative to the magnetic field. Due to the Lorentz force these electrons will start a cyclotron motion. Accordingly, electrons also have a longitudinal and a perpendicular energy component (E_{\parallel} and E_{\perp}). The electrostatic filter, however, can only filter by the longitudinal energy component E_{\parallel} . Therefore, the perpendicular energy component E_{\perp} of the electron has to be converted into a longitudinal energy component E_{\parallel} . The conversion of momentum is realized through exploiting the conservation of the magnetic moment

$$\mu = \frac{E_{\perp}}{B} = \text{const} \quad (3.7)$$

in an adiabatic transition and the conversion of energy. By letting the magnetic field drop from $B_{\text{max}} = 6 \text{ T}$ at the entrance of the spectrometer to $B_{\text{A}} = 3 \cdot 10^{-4} \text{ T}$ at the so-called analyzing plane, E_{\perp} is reduced by four orders of magnitude. Due to the conservation of energy, this leads to an increase of longitudinal energy E_{\parallel} . Nevertheless, the finite ratio $B_{\text{A}}/B_{\text{max}}$ determines the maximal remaining perpendicular energy of the electron

$$\Delta E = \frac{B_{\text{A}}}{B_{\text{max}}} \cdot E_0 = 0.93 \text{ eV} \quad (3.8)$$

which represents the energy resolution of the MAC-E filter. To achieve this very high energy resolution, the dimensions of the main spectrometer have to be built accordingly: a length of 23.3 m and a diameter of 10 m are required to house the magnetic fluxtube. The magnetic fluxtube is likewise given by the source diameter and the desired field strengths at the entrance and at the analyzing plane of the spectrometer. In order to minimize scattering and background due to stored particles the main spectrometer is operated at an ultra high vacuum of $\leq 10^{-11} \text{ mbar}$.

The Focal Plane Detector (FPD)

The focal plane detector is a radially and azimuthally segmented silicon detector with 148 pixels mounted at the very end of the experimental setup. By detecting electrons which have surpassed the retarding potential of the main spectrometer it yields the count rate at various retarding potentials. Due to its segmentation the position of the detection can be recorded and the track of the electron through the main spectrometer can be inferred. A thorough description of the focal plane detector can be found in [Sch14].

3.3. Analytic Description of the Experiment

In order to develop a probabilistic model, allowing for a fit of theoretical parameters to measured data, the experimental setup as described in section 3.2 needs to be reflected in an analytic description. As a consequence of the experimental setup, the energy spectrum of equation 3.1 is integrated (see subsection 3.3.1) and subject to fundamental experimental influences (see subsections 3.3.2 - 3.3.4).

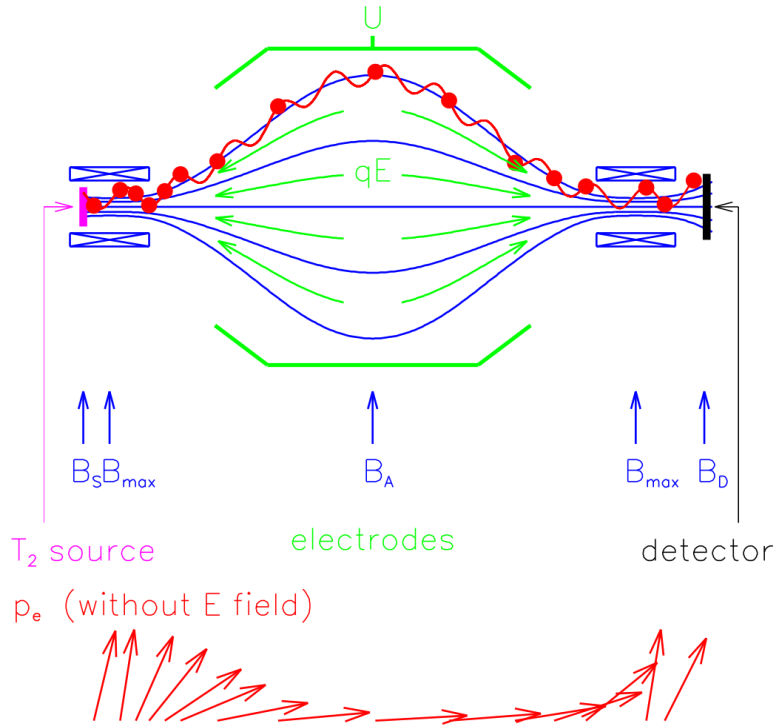


Figure 3.3.: **The MAC-E filtering principle.** The schematic sketch at the top illustrates the MAC-E filtering principle described in the main text. The red arrows at the bottom show the transformation of electron momentum. Illustration taken from [KC05].

3.3.1. The Integrated Spectrum

The main spectrometer of the KATRIN experiment works according to the MAC-E filtering principle. As a consequence, it records an integrated β -spectrum instead of the differential spectrum given by equation 3.1. Accordingly, the number of electrons detected at a given retarding potential U is

$$N(qU) \propto t_{qU} \int_{qU}^{E_0} \frac{d\dot{N}}{dE}(E, m_\nu^2) \cdot R(E, qU) dE \quad (3.9)$$

with t_{qU} the measuring time at qU , the differential spectrum $\frac{d\dot{N}}{dE}(E, m_\nu^2)$ and the Response Function $R(E, qU)$. The response function (see 3.3.4) comprises the transmission function (see 3.3.2) and the energy loss function (see 3.3.3). The transmission function describes which electrons can pass the MAC-E filter while the energy loss function describes scattering processes in the WGTS [KC05].

3.3.2. The Transmission Function

The transmission function describes in an analytic way which electrons with kinetic energy E_S and starting polar angle θ_{tr} are transmitted through the MAC-E filter. However, not all electrons generated in the WGTS will even reach the filter. Due to the magnetic mirror effect between the source and transport section B_S and the beginning of the MAC-E filter B_{max} , only electrons below a starting polar angle θ_{max}

enter the MAC-E filter¹. This makes sure that electrons with a high emission polar angle and therefore a long path length through the source are not considered any further. Such electrons are not desirable for analysis as they have higher probabilities to have had undergone scattering in the WGTS [KC05]. According to [Bea80] the maximum accepted polar angle θ_{\max} is

$$\sin \theta_{\max} = \sqrt{\frac{B_S}{B_{\max}}}. \quad (3.10)$$

For KATRIN, this is approximately

$$\theta_{\max} = \arcsin \sqrt{\frac{3.6 \text{ T}}{6 \text{ T}}} \approx 51^\circ \quad (3.11)$$

for electrons starting at the source at $B_S = 3.6 \text{ T}$ and for $B_{\max} = 6 \text{ T}$. A comprehensive derivation of the transmission function including relativistic effects and findings from SDS commissioning measurements can be found in [Gro15]. The work at hand focuses on a summary of the derivation of the transmission function². In the main spectrometer, transmission can only occur if the starting kinetic energy E_S of the electrons exceeds the transmission energy

$$E_{\text{tr}} = \frac{q(U_A - U_S)}{1 - \sin^2 \theta_S \cdot \frac{B_A \cdot (\gamma_S + 1)}{B_S \cdot (\gamma_A + 1)}}. \quad (3.12)$$

The transmission energy depends on the retarding potential U_A and the magnetic field B_A at the analyzing plane as well as U_S and B_S . U_S is the potential at the source which is currently planned to be zero. The values of γ_S and γ_A denote the relativistic Lorentz factor of the electron in the source and the analyzing plane respectively. This description only holds for a source at a certain fixed polar angle θ_S relative to the magnetic field. However, equation 3.12 can easily be rearranged to reflect arbitrary angular distributions of the source. In this case, an individual electron at energy E_S passes the filter if its polar angle θ_S is below

$$\theta_{\text{tr}}(E_S) = \arcsin \sqrt{\frac{E_S - q(U_A - U_S) \frac{B_S \cdot (\gamma_A + 1)}{B_A \cdot (\gamma_S + 1)}}{E_S}}. \quad (3.13)$$

This relation leads to the general form of the transmission function

$$T(U_A) = \int_{E_{\text{tr}}(U_A)}^{\infty} \int_0^{\theta_{\text{tr}}(E_S)} \omega(\theta) d\theta \cdot F(E_S) dE_S \quad (3.14)$$

where an arbitrary angular distribution for emitted electrons in the source $\omega(\theta)$ can be considered as a weighting factor for the energy distribution $F(E_S)$. In the case of KATRIN these angular distributions will usually be isotropic for the decaying tritium or fixed polar angles for calibration sources like an electron gun.

¹The index S for a magnetic field always denotes “source” while it means “start” for angles and energies throughout this thesis.

²The original derivation of the transmission function was already shown in [KC05]. However, this was a non-relativistic derivation. [Gro15] shows the importance of considering relativistic effects to improve the analytic description of the KATRIN experiment. For reasons of computation time the work at hand uses an analytic transmission function in addition to Monte Carlo simulations to simulate the electron gun in chapter 6. Following the recommendations of [Gro15], the analytic transmission function used, accounts for relativistic effects.

Transmission Function of an Isotropic Source

As shown in [Gro15] an isotropic distribution

$$\omega(\theta) = \sin(\theta) \quad (3.15)$$

subdivides the transmission function into three cases:

$$T(E_S, q\Delta U) = \begin{cases} 0 & E_S - q\Delta U < 0 \\ 1 - \sqrt{1 - \frac{E_S - q\Delta U}{E_S} \cdot \frac{B_S \cdot (\gamma_A + 1)}{B_A \cdot (\gamma_S + 1)}} & 0 \leq E_S - q\Delta U \leq \frac{B_S \cdot (\gamma_A + 1)}{B_A \cdot (\gamma_S + 1)} \cdot E_S \\ 1 & E_S - q\Delta U > \frac{B_S \cdot (\gamma_A + 1)}{B_A \cdot (\gamma_S + 1)} \cdot E_S \end{cases} \quad (3.16)$$

In the first case, no electrons pass the filter since their energy is below the retarding energy. In the second case, electrons have enough surplus energy to pass the filter if their starting polar angle θ_S is below the transmission polar angle $\theta_{tr}(E_S)$. For surplus energies $q\Delta U > \frac{B_S \cdot (\gamma_A + 1)}{B_A \cdot (\gamma_S + 1)} E_S$ the electron will pass the filter regardless of its starting polar angle as long as it is below $\theta_{max} = 51^\circ$.

Furthermore, the magnetic mirror effect (equation 3.10) has to be considered: there are electrons with a starting polar angle below θ_{tr} which will still not be transmitted as their polar angle is higher than θ_{max} . The transmission function becomes:

$$T(E_S, q\Delta U) = \begin{cases} 0 & E_S - q\Delta U < 0 \\ \frac{1 - \sqrt{1 - \frac{E_S - q\Delta U}{E_S} \cdot \frac{B_S \cdot (\gamma_A + 1)}{B_A \cdot (\gamma_S + 1)}}}{1 - \sqrt{1 - \frac{B_S \cdot (\gamma_A + 1)}{B_{max} \cdot (\gamma_S + 1)}}} & 0 \leq E_S - q\Delta U \leq \frac{B_A \cdot (\gamma_S + 1)}{B_{max} \cdot (\gamma_A + 1)} \cdot E_S \\ 1 & E_S - q\Delta U > \frac{B_A \cdot (\gamma_S + 1)}{B_{max} \cdot (\gamma_A + 1)} \cdot E_S \end{cases} \quad (3.17)$$

Figure 3.4 shows an illustration of the non-relativistic version of this equation. An explanation of a transmission function for a non-isotropic source, namely the electron gun, can be found in section 6.1.

3.3.3. The Energy Loss Function

The energy loss function is an analytic description of the probability of an electron to lose energy ϵ . Energy losses occur due inelastic scattering processes of electrons with tritium molecules. The effect applies to electrons from tritium decay as well as to electrons from the Rearsection electron gun. This is exploited in calibration measurements. For KATRIN standard parameters, i. e. the source column density $\rho d = 5 \cdot 10^{17} \text{ cm}^{-2}$, the average probability of a β -decay electron to pass the source unscattered is about 41.33%. If inelastic scattering occurs it will lead to relatively large energy losses ϵ of at least 10 eV for single scattering [KC05]. However, this also means that the region right below the endpoint of the spectrum is not affected by any inelastic scattering effects. In this region only elastic scattering effects might occur. Elastic effects lead to an average energy loss of 16 meV and have a comparatively small influence on the response function [KC05].

Analytically, the energy loss function is a normalized probability distribution

$$f(\epsilon) = \frac{1}{\sigma_{inel}} \frac{d\sigma_{inel}}{d\epsilon} \quad (3.18)$$

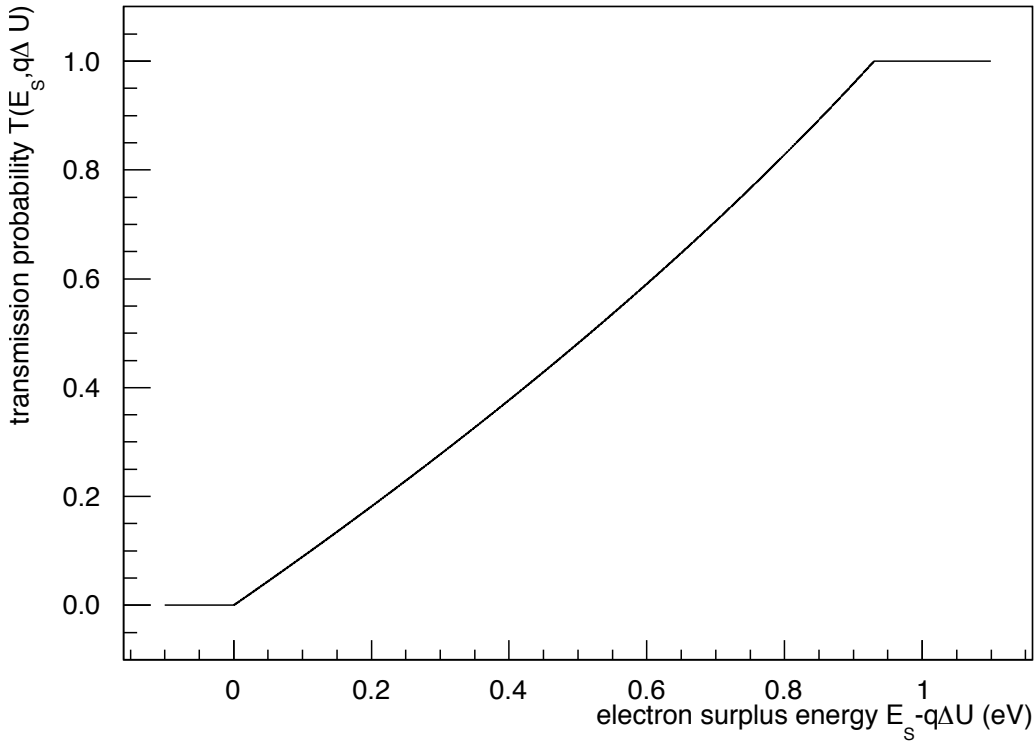


Figure 3.4.: **The transmission function for an isotropic source.** The figure shows a non-relativistic approximation of the transmission function for an isotropic source. To generate this plot KATRIN standard parameters were used: $E_S = 18600$ eV, $B_S = 3.6$ T, $B_A = 0.3$ mT and $B_{\max} = 6$ T. The energy resolution $\Delta E = \frac{B_A}{B_{\max}} \cdot E_S = 0.93$ eV can be clearly seen.

which describes the probability of an electron to lose an absolute amount ϵ of its energy. It is normalized such that

$$\int_0^{\infty} f(\epsilon) d\epsilon = 1. \quad (3.19)$$

Figure 3.5 shows the parameterized energy loss function according to [Ase00]. The following subsection will describe how this parameterization was realized.

The Energy Loss Function According to Aseev

For determination of the total inelastic scattering cross section, measurements with gaseous tritium and an electron energy of 18.6 keV have been conducted by [Ase00]. It is not possible to directly derive the energy loss function which is why it is parameterized by a Gaussian and a Lorentzian distribution

$$f(\epsilon) = \begin{cases} A_1 \exp\left(-\frac{2(\epsilon-\epsilon_1)^2}{\omega_1^2}\right) & \epsilon < \epsilon_C \\ A_2 \frac{\omega_2^2}{\omega_2^2 + 4(\epsilon-\epsilon_2)^2} & \epsilon \geq \epsilon_C \end{cases}. \quad (3.20)$$

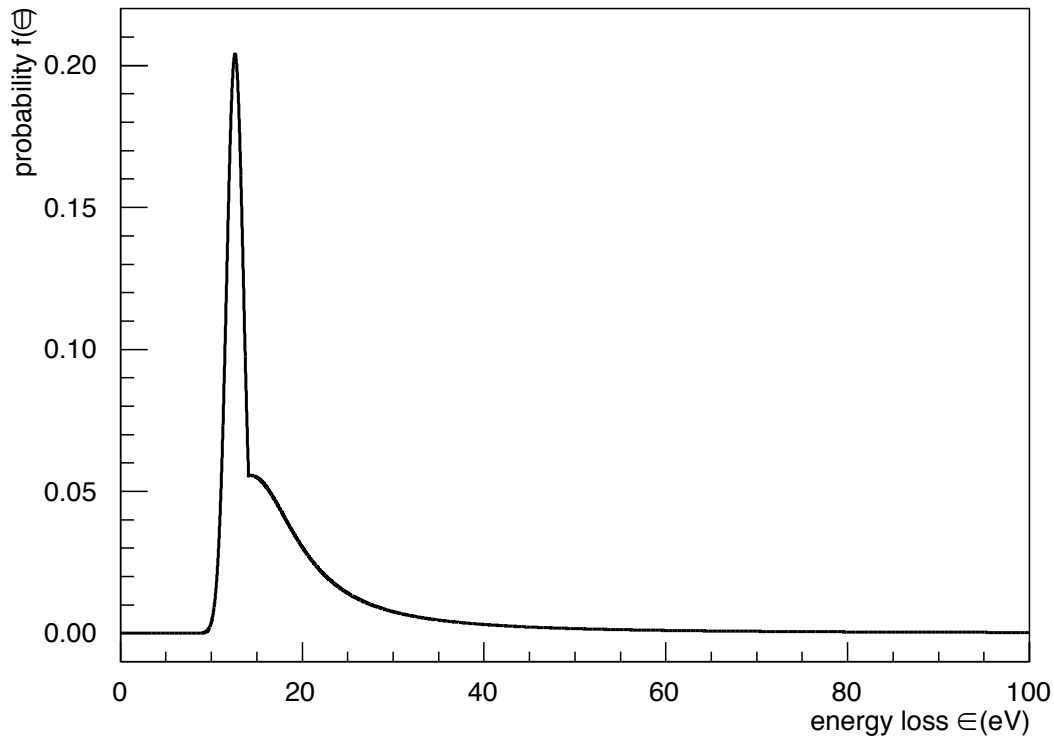


Figure 3.5.: **The parameterized energy loss function for the KATRIN experiment.** The plot depicts the energy loss function $f(\epsilon)$ which gives the probability for an energy loss of energy ϵ when electrons in the source scatter inelastically with molecular tritium. This form of the function has been generated based on a parameterization by [Ase00]. Details on the parameters can be found in the main text. The model resembles prominent features of energy loss such as the rising curve at 10 eV which shows that there is no inelastic scattering below this threshold, inelastic scattering in a region of about 11 – 15 eV and continuous ionization processes for energies beyond 15.4 eV.

The Gaussian function (coefficient A_1) provides the best fit for excited states whereas the Lorentzian function (coefficient A_2) is attributed to ionization processes. The fitted parameters, averaged over four measurements, are

$$\begin{aligned}
 A_1 &= 0.204 \pm 0.001 \\
 \omega_1 &= 1.85 \pm 0.02 \\
 \epsilon_1 &= 12.6 \\
 A_2 &= 0.0556 \pm 0.0003 \\
 \omega_2 &= 12.5 \pm 0.1 \\
 \epsilon_2 &= 14.30 \pm 0.02.
 \end{aligned}
 \tag{3.21}$$

The transition between the two fit functions was chosen to be at $\epsilon_C = 14.09$. Finally, the total inelastic scattering cross section as reported by [Ase00] is

$$\sigma_{\text{inel}} = (3.40 \pm 0.07) \cdot 10^{-18} \text{cm}^2.
 \tag{3.22}$$

This form of the energy loss function has been implemented into the “Source and Spectrum Calculation” package (SSC) by [Hoe12] (see section 4.1). However, the program code neither accounts for uncertainties in the form of the energy loss function as shown in figure 3.5 nor for uncertainties in the normalization factor σ_{inel} . In particular, the experimental uncertainties on the total inelastic scattering cross section are not sufficient for the KATRIN design requirements which is why there will be electron gun calibration measurements to obtain more accurate results for this parameter. It is one of the aims of the work at hand to quantify how precise these measurements have to be, in order to meet the requirements by the technical design report [KC05]. Such measurements will not only yield new results on the total inelastic scattering cross section but also on the shape and therefore the parameterization of the energy loss function. However, since the total inelastic scattering cross section is the most important one among these parameters, this thesis focuses on it. Besides an analytic description it is also possible to quantify the energy loss through Monte Carlo simulations which is described in subsection 4.3.1.

Scattering Probabilities

When passing the WGTS, electrons can not only scatter once but multiple times. As a consequence, energy loss functions for these cases need to be folded accordingly ($f(\epsilon) \otimes f(\epsilon) \otimes \dots$). The probabilities for an electron to be scattered i times is Poisson distributed [Ase00]. In the case of the KATRIN experiment it is

$$P_i(z, \theta) = \frac{(\lambda(z, \theta) \cdot \sigma_{\text{inel}})^i}{i!} e^{-\lambda(z, \theta) \cdot \sigma_{\text{inel}}} \quad (3.23)$$

where $\lambda(z, \theta)$ is the effective column density for an electron at position z under a polar angle θ . It is a measure for the path that an electron at position z has yet to pass under density $\rho(z')$ in a source of total length L . It is calculated as

$$\lambda(z, \theta) = \frac{1}{\cos \theta} \int_z^L \rho(z') dz' \quad (3.24)$$

which shows that electrons under a higher polar angle θ and with a small z , i. e. a starting position at the beginning of the source, have to pass a longer path and are therefore more likely to scatter. The average scattering probabilities for the WGTS are

$$P_i^{\text{WGTS}} = \frac{1}{\rho d (1 - \cos \theta_{\text{max}})} \int_0^L dz \int_0^{\theta_{\text{max}}} d\theta \rho(z) P_i(z, \theta) \sin \theta. \quad (3.25)$$

Through P_i this formula is dependent on the total inelastic scattering cross section and the corresponding uncertainties as laid out in subsection 3.3.3. So far, it has not been possible to test for the influence of a wrongly assumed total inelastic scattering cross section and an implementation that allows for this analysis has been part of the work at hand (see section 4.1.1).

3.3.4. The Response Function

The response function $R(E, qU)$ comprises all experimental effects on the electron from its start (either in an electron gun or in the WGTS) up to its passage of the

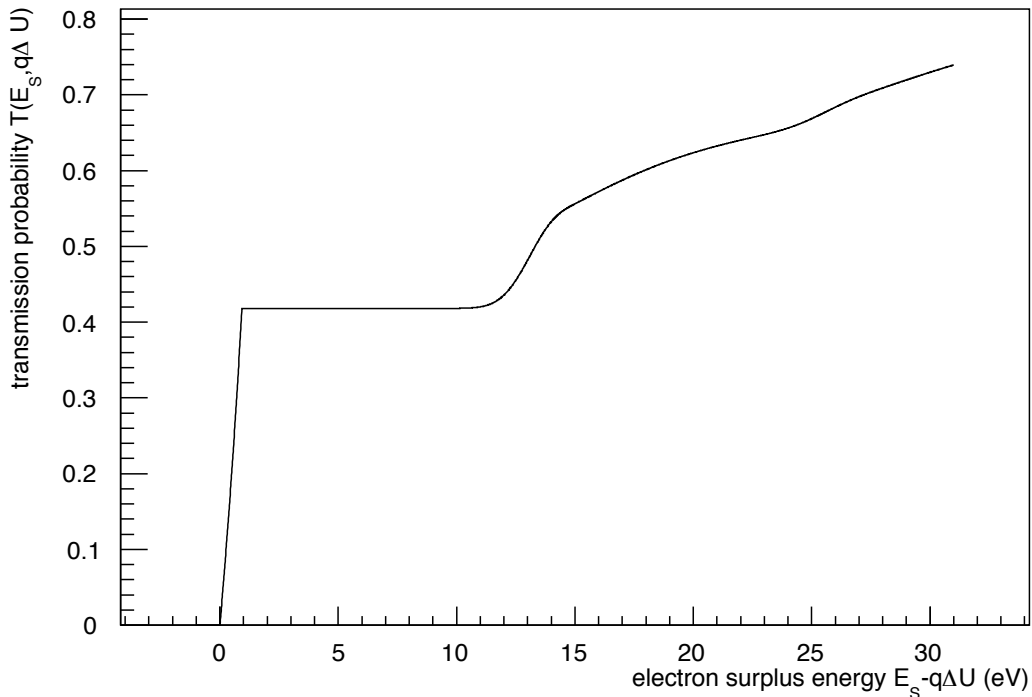


Figure 3.6.: **The response function for the KATRIN experiment.** The plot depicts an analytically calculated response function for KATRIN standard parameters. It shows the transmission probability of electrons for varying electron surplus energies above the retarding potential of the main spectrometer.

integrating MAC-E filter. A thorough understanding of this function is therefore crucial for a later fit of the β -spectrum aiming to derive the squared neutrino mass. Analytically, the response function is an integral over all electron energies and combines the effects of the transmission function (see subsection 3.3.2) and the energy loss function considering the different scattering probabilities (see subsection 3.3.3). Just like the transmission function it is normalized to one and can be interpreted as a probability. In the case of the response function, namely, the probability of an electron to reach the detector. For an electron at energy E and a retarding energy qU , the response function is [KC05]

$$R(E, qU) = \int_0^E T(E - \epsilon, qU) \cdot (P_0\delta(\epsilon) + P_1f(\epsilon) + P_2(f \otimes f)(\epsilon) + \dots) d\epsilon. \quad (3.26)$$

Figure 3.6 shows an exemplary analytical response function for electrons emitted in the WGTS. Since energy losses from inelastic scattering do not start below 10 eV, the response function has a plateau in this range which develops after a steep rise due to the transmission function. It is important to point out that the response function in figure 3.6 differs from the response functions shown in chapter 6 (figures 6.3 to 6.5) because the latter are generated for electrons from an electron gun with well defined energies and angles.

3.3.5. Properties of the Rearsection Electron Gun

The Rearsection electron gun fulfills several calibration and monitoring tasks for the KATRIN experiment described in detail in [Bab14]. The work at hand focuses on the determination of the total inelastic scattering cross section which is simulated in chapter 6. For this purpose, the electron gun is designed with a sharp intrinsic energy spread below 0.2 eV and a well-defined angular emission behavior over $0 - 51^\circ$ with an angular spread below 4° at a source magnetic field strength of $B_S = 3.6$ T. Furthermore, the emission rate of the electron gun is in the order of $10^4 - 10^6$ cps with a stability of at least 0.1 % over several hours. These parameters are defined as requirements in the Rearsection technical design report [Bab13].

The work at hand uses preliminary commissioning measurement data of the electron gun [Mon15] in order to work with most recent data on the energy spreads and count rates. Data on the angular behavior is based on simulations in [Bab14]: angular spreads are lower for small emission angles and higher for high emission angles. The lowest possible emission angle is $\theta_S = (1.80 \pm 0.73)^\circ$ and the maximum angle is $\theta_S = (51.20 \pm 2.16)^\circ$ at the WGTS magnetic field strength of 3.6 T. It is reasonable to assume that the spreads of θ_S can be linearly interpolated.

The Rearsection electron gun works by emitting electrons from a metal plate based on the photoelectric effect [Ein05]. By shining ultraviolet light on a gold plate, electrons are emitted if the photon energy exceeds the work function of the gold. In preliminary measurements the electron count rates for different wavelengths have been analyzed [Mon15]. The rate of emitted electrons can be increased (respectively decreased) at the cost (respectively gain) of beam energy precision. For the work at hand three combinations of precisions in electron beam energy and electron rate have been identified for further analysis. Figure 3.7 depicts electron count rates on a detector after the emitted electrons have been energy-filtered. Since the electron energy distribution can be approximated by a Gaussian distribution [Bab14], an error function can be fitted to the integrated spectrum [Gro15]

$$\frac{dN}{dEdt}(U_R) = \frac{p0}{2} \cdot \operatorname{erfc}\left(\frac{U_R - p2}{\sqrt{2} \cdot p3}\right) + p1 . \quad (3.27)$$

$p0$ to $p3$ are scaling factors. $p0$ is the amplitude and $p1$ denotes background effects. Therefore, the count rate of the electron beam is in good approximation

$$\frac{dN}{dt} = p0 - p1 . \quad (3.28)$$

Since a Gaussian distribution of electron energies has been assumed for this special form of the error function, $p2$ denotes the mean value μ_E and $p3$ the uncertainty σ_E of the Gaussian distribution.

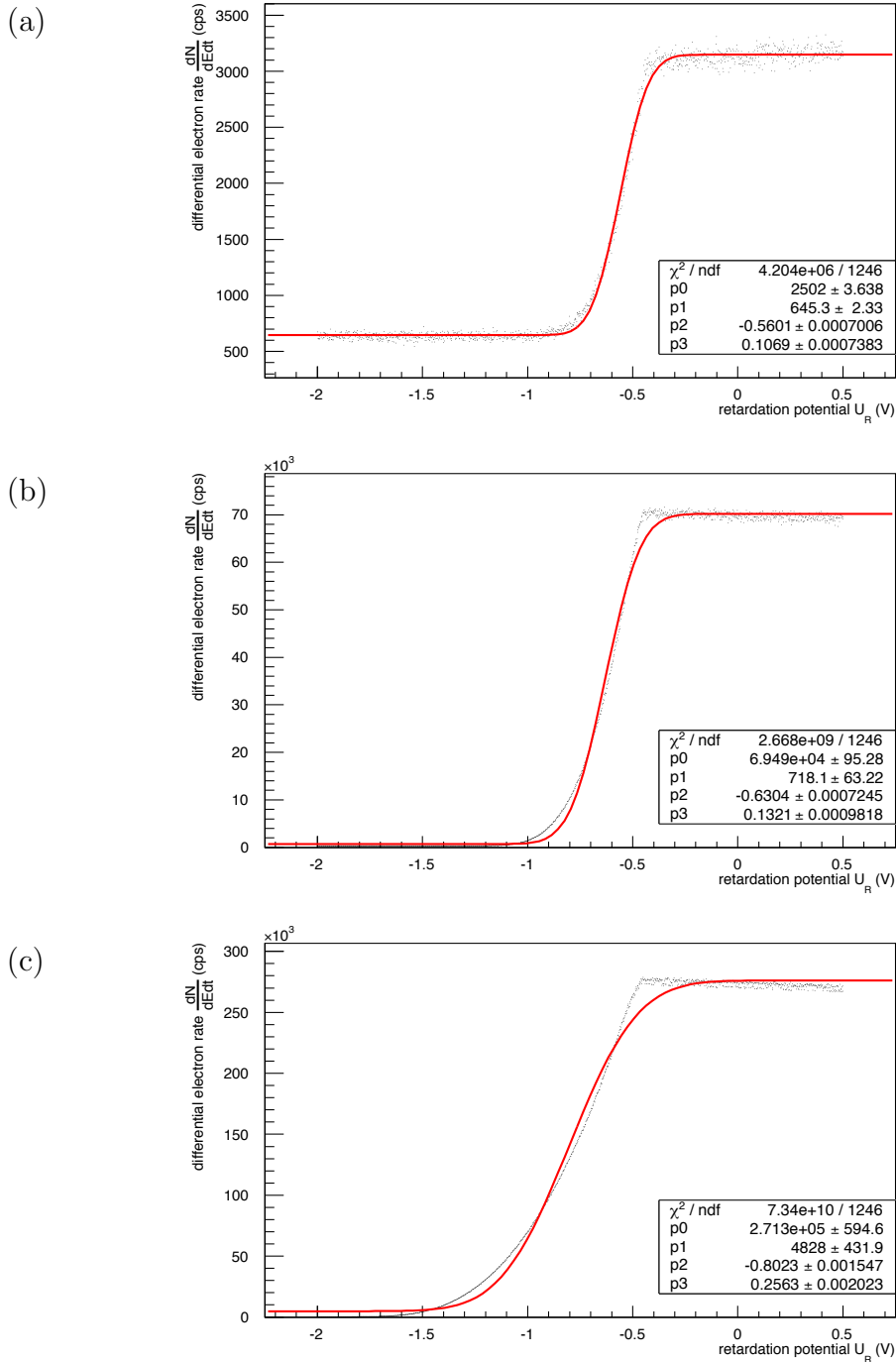


Figure 3.7.: **Electron count rates obtained with the electron gun for different UV-filters.** Data for these graphs has been provided by [Mon15]. The graphs depict electron count rates on a detector as a function of a retardation potential (i. e. energy filtering). From top to bottom different filters have been applied to the UV light leading to different energy distributions of emitted electrons. It is apparent that the fit function deviates from measured data in the transition regions at the top and the bottom of the curve. This can most likely be explained by the only approximately Gaussian distribution of electron energies. Furthermore, data provided by [Mon15] did not provide any error estimates. As a consequence, there is a mismatch between χ^2 and the number of degrees of freedom. However, conclusions drawn from these fits can be seen as an estimate.

An analysis of figure 3.7 yields three combinations of spreads in the electron gun beam energy³ and count rates⁴

$$\sigma_E = (107 \pm 1) \text{ meV} \approx 107 \text{ mV} , \frac{dN}{dt} = (1857 \pm 2) \text{ cps} \approx 2 \text{ kcps} \quad (3.29)$$

$$\sigma_E = (132 \pm 1) \text{ meV} \approx 132 \text{ mV} , \frac{dN}{dt} = (68,772 \pm 32) \text{ cps} \approx 69 \text{ kcps} \quad (3.30)$$

$$\sigma_E = (256 \pm 2) \text{ meV} \approx 256 \text{ mV} , \frac{dN}{dt} = (266,472 \pm 163) \text{ cps} \approx 266 \text{ kcps} . \quad (3.31)$$

3.3.6. Unfolding of the Response Function

As pointed out earlier, the work at hand will focus on the total inelastic scattering cross section which normalizes the energy loss function according to [Ase00] (see equation 3.18) and plays an important role in the calculation of scattering probabilities (see equation 3.23). Nevertheless, the shape of the energy loss function, i. e. the inelastic cross section in its differential form, does also play a very important role for the KATRIN experiment. For this reason previous work investigated how the energy loss function could be extracted [Zie13] or deconvolved [Wol08], [Kra11] from the response function measured with the Rearsection electron gun:

- For the extraction method [Zie13], it is only necessary to measure the response function of the electron gun for one column density of $\rho d \approx 3 \cdot 10^{17} \text{ cm}^{-2}$. After its measurement, the response function is subdivided into intervals. For each interval, one higher scattering order of inelastic scattering is considered. The parts of the response function for each interval are derived consecutively so that each energy loss function for an interval is based on the energy loss function of the previous interval.
- The deconvolution approach [Wol08] requires the measurement of the response function of the electron gun at four column densities. Recommended values are $\rho d = 0, 0.5, 3, 6 \cdot 10^{17} \text{ cm}^{-2}$ [Kra11]. The resulting functions yield an equation system from which the energy loss function can be deconvolved by matrix inversion. Various methods for an inversion have been tested [Wol08] and optimized [Kra11].

A comparison of both methods showed that the deconvolution methods results in smaller systematic uncertainties on the squared neutrino mass. Due to the close relation between the energy loss function and the total inelastic scattering cross section the findings described in chapter 6 are of great interest for the extraction and deconvolution of the energy loss function as well.

³For completeness, spreads on the beam energy are listed with uncertainties resulting from the fit procedure. However, for analyses performed in chapter 6 only mean values are used.

⁴For completeness, uncertainties on the electron gun rate have been calculated. However, the fits in figure 3.7 only yield estimates so that the use of rounded values seems reasonable.

4. The KASPER Software Framework

The KASPER analysis and simulation framework comprises major parts of the software which is required to prepare and analyze the KATRIN experiment. It consists of a variety of packages and is programmed in C++. Among these packages are the “Source and Spectrum Calculation” (SSC) for analytic calculations of the differential and integrated spectrum (see section 4.1), KAFIT for statistical analyses (see section 4.2) and KASSIOPEIA for Monte Carlo particle tracking simulations of the experiment (see section 4.3). As these packages played a major role for the work at hand, an introduction is given in the following sections. Furthermore, contributions made in the scope of the work hand will be explained.

4.1. SSC

Section 3.3 has given an overview of the cornerstones for an analytic description of the response function of the KATRIN experiment. To allow for productive work based on these findings they have to be reflected in the KASPER software environment. Accordingly, it is the purpose of SSC to calculate integrated and differential spectra based on the equations from section 3.3. The foundation for this code has been laid by [Hoe12] and [Kae12], and a number of additions has been made since.

Figure 4.1 gives a schematic overview on the most important parts of the SSC package:

- **SSCWGTS**
This class uses the concept of voxelization to describe the source [Hoe12]. For this purpose the beamtube is divided into a selectable number of axial slices of variable width which can be subdivided into radial rings and azimuthal segments. Each of these three-dimensional segments is called a voxel and stores information on its volume (e. g. magnetic and electric field strength or tritium gas density) in a class called SSCSEGMENT. Using this approach allows for modeling of non-homogeneous gas profiles and the calculation of gas dynamics in the WGTS. When voxelization is deactivated the source is considered to be homogeneous.

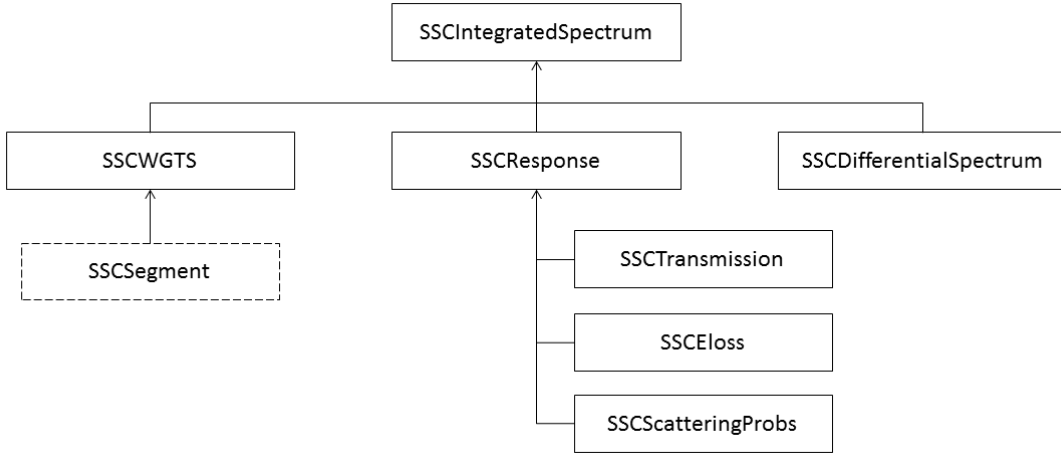


Figure 4.1.: **Schematic description of the SSC package.** A description of individual classes is given in the main text.

- **SSCRESPONSE, SSCTRANSMISSION and SSCELOSS**
These classes are responsible for calculating the functions with their corresponding names as explained in section 3.3.
- **SSCSCATTERINGPROBS**
The calculation of scattering probabilities according to subsection 3.3.3 used to be part of SSCWGTS. After an update to the calculation procedure (compare subsection 4.1.1) the new class SSCSCATTERINGPROBS has been established in the course of this thesis. This also included speed improvements on the calculation of scattering probabilities and easier access to the total inelastic cross section as a fit parameter. This code-reorganization significantly facilitated the work performed in chapter 5.
- **SSCDIFFERENTIALSPECTRUM**
In this class, the differential energy spectrum according to section 3.1 is calculated.
- **SSCINTEGRATEDSPECTRUM**
This class ultimately calculates the integrated spectrum by folding the response function with the differential spectrum and integrating the result (see subsection 3.3.1). For this purpose, the previously explained classes are used.

4.1.1. Improved Calculation of Scattering Probabilities

The calculation of scattering probabilities in the WGTS follows equation 3.25:

$$P_i^{\text{WGTS}} = \frac{1}{\rho d(1 - \cos \theta_{\max})} \int_0^L dz \int_0^{\theta_{\max}} d\theta \rho(z) P_i(z, \theta) \sin \theta . \quad (4.1)$$

However, since gas profiles in the source are not homogeneous it is necessary to account for this aspect through voxelization where each voxel can have its own density. So far, this has been realized through a distinction of two cases: For a homogeneous WGTS scattering probabilities calculated in [KC05] were used. Once voxelization

was turned on, scattering probabilities per voxel were calculated according to

$$P_i^{\text{Voxel}} = \frac{1}{1 - \cos \theta_{\text{max}}} \int_0^{\theta_{\text{max}}} d\theta \cdot \sin \theta \cdot \exp(-\sigma_{\text{inel}} \cdot \lambda(z, \theta)) \frac{(\sigma_{\text{inel}} \cdot \lambda(z, \theta))^i}{i!} \quad (4.2)$$

(compare equation 3.23) and averaged over slices. Here, θ_{max} is the maximum accepted polar angle, σ_{inel} the total inelastic scattering cross section, i the number of scattering processes and $\lambda(z, \theta)$ the effective column density as defined by equation 3.24. The latter can be seen as the column density in front (i.e. towards the detector) of the current voxel. To avoid an unnecessary discontinuity between a segmented and a non-segmented WGTS a two-dimensional integration has been implemented in the course of this work: A calculation of scattering probabilities according to

$$P_i^{\text{Voxel}} = \frac{1}{\rho_V d_V (1 - \cos \theta_{\text{max}})} \int_0^{d_V} dy \int_0^{\theta_{\text{max}}} d\theta \cdot \sin \theta \cdot \rho_V \cdot \exp\left(-\sigma_{\text{inel}} \cdot \left(\frac{\rho_V(d_V - y)}{\cos \theta} + \lambda(z, \theta)\right)\right) \frac{(\sigma_{\text{inel}} \cdot \left(\frac{\rho_V(d_V - y)}{\cos \theta} + \lambda(z, \theta)\right))^i}{i!}. \quad (4.3)$$

considers the density within a voxel ρ_V and integrates over its width d_V . This also covers the case of a homogeneous source which corresponds to a single voxel.

4.2. KaFit

The KAFIT package is the major tool for statistical analyses within the KATRIN collaboration. This work will focus on a summary of the concept of ensemble simulations. They can be performed by KAFIT and are the foundation for the work detailed in chapter 5. The summary in the current section is based on [Hoe12] and [Kle14] who performed major upgrades to a program package described by [Kae12].

In a nutshell, ensemble simulations with KAFIT work as follows: The SPECTRUMSIMULATOR (see subsection 4.2.1) calculates a theoretical rate for the integrated spectrum. Using the FITTER (see subsection 4.2.3) the theoretical rate will be fitted to measured data or data emulated by the RUNGENERATOR (see subsection 4.2.2). When this process is repeated many times (i.e. for many KATRIN experiments, equivalent to three full years of data taking) one speaks of ensemble simulations (see subsection 4.2.4). Usually this means repetitions in the order of 10^5 . Obviously, the repetition of the KATRIN experiment on such a scale is only possible in simulations. For this reason, ensemble simulations will always be based on emulated measurements by the RUNGENERATOR.

4.2.1. The SpectrumSimulator

The SPECTRUMSIMULATOR holds the theoretical background of the KATRIN experiment. All knowledge about the experimental setup and systematic effects is included into this class. Later, this model will be fitted to experimental data so that a squared neutrino mass can be inferred. The accuracy and completeness of the model are of paramount importance. According to subsection 3.3.1, detected

events N at the detector for a count rate \dot{N}_S of electrons emitted by tritium behave according to equation 3.9:

$$N(qU) \propto t_{qU} \int_{qU}^{E_0} \frac{d\dot{N}_S}{dE}(E, m_\nu^2) \cdot R(E, qU) dE . \quad (4.4)$$

In addition, a free parameter for the signal amplitude R_S is considered for normalization. To account for an unknown background rate, dedicated classes are implemented in KASPER to calculate \dot{N}_{bg} . Again, a free parameter for the background amplitude R_{bg} is included. Altogether, this describes a theoretical number of events occurring during a measuring time t_{qU} at retarding energy qU :

$$N^{\text{theo}}(qU) = \left(R_S \cdot \dot{N}_S(qU, E_0, m_\nu^2) + R_{bg} \cdot \dot{N}_{bg} \right) \cdot t_{qU} . \quad (4.5)$$

The measuring times t_{qU} are distributed according to a measuring time distribution (see section 4.2.5). There are four fitting parameters: The parameter of interest, the squared neutrino mass m_ν^2 , and three so-called nuisance parameters R_S , E_0 and R_{bg} . Nuisance parameters are actually of no direct interest to the experimenter but since they are not sufficiently well known and furthermore show strong correlations with the parameter of interest, they can only be treated as free fit parameters.

4.2.2. The RunGenerator

The RUNGENERATOR is set up very similar to the SPECTRUMSIMULATOR. Just like with the SPECTRUMSIMULATOR the whole analytic model for KATRIN can be accessed with this class. However, it serves a different purpose as it emulates an actual measurement. This means that once the experiment is up and running the data from the RUNGENERATOR is replaced by actual measured data. The emulated experimental number of counts $N^{\text{exp}}(qU)$ is assumed to be Poisson-distributed around an expectation value

$$\tilde{N}(qU) = \left(\dot{N}_S(qU, E_0, m_\nu^2) + \dot{N}_{bg} \right) \cdot t_{qU} . \quad (4.6)$$

Therefore it is

$$N^{\text{exp}}(qU) = \text{Poisson}(\tilde{N}(qU)) . \quad (4.7)$$

This means that, by construction, the SPECTRUMSIMULATOR and the RUNGENERATOR are set up in the same way. However, in a consecutive step the RUNGENERATOR emulates measurements at different retarding potentials based on the measuring time distributions introduced in section 4.2.5 and through smearing expectation values by a Poisson distribution.

4.2.3. The Fitter

The FITTER is the routine which performs the fit between the expected number of counts from the SPECTRUMSIMULATOR and the emulated number of counts from the RUNGENERATOR. Thereby it estimates the free fit parameters which now serve as model input through the SPECTRUMSIMULATOR. Using the maximum-likelihood

method (e. g. [Cow98]) the estimates for the parameters $\vec{\theta}$ are the so-called best-fit values $\hat{\vec{\theta}}$ for a maximized likelihood function

$$L(\vec{\theta}|\vec{X}) = \prod_i p(X_i|\vec{\theta}). \quad (4.8)$$

p is the probability density function which gives the probability of a measurement result X_i to occur given a specific realization of the parameters $\vec{\theta}$. For KATRIN, it is the best-fit estimator for the squared neutrino mass \hat{m}_ν^2 which is of interest. Instead of maximizing the likelihood function it is common practice to minimize the negative logarithm $-2\log L(\vec{\theta}|\vec{X})$ instead. This is due to the fact that numerical methods for minimization are well-established. Furthermore, if p is Gaussian distributed the term $-2\log L(\vec{\theta}|\vec{X})$ equals the Chi-square function:

$$-2\log L(\vec{\theta}|\vec{X}) = \chi^2. \quad (4.9)$$

As mentioned above, in the case of KATRIN probability distributions are not Gaussian but Poissonian. However, for sufficiently high statistics equation 4.9 also holds for Poissonian distributions. Therefore, it is

$$\chi^2(E_0, m_\nu^2, R_S, R_{\text{bg}}|\vec{N}) = \sum_i \left(\frac{N_i^{\text{exp}}(qU_i) - N_i^{\text{theo}}(qU_i, E_0, m_\nu^2, R_S, R_{\text{bg}})}{\sigma_i} \right)^2. \quad (4.10)$$

Here, σ_i are the uncertainties on measurement results N_i^{exp} with $\sigma_i = \sqrt{N_i^{\text{exp}}}$ in the case of the KATRIN experiment. The minimization tasks for this work were performed by the ROOT MINUIT2 package [ROO15].

4.2.4. Ensemble Simulations

Ensemble simulations are a Monte-Carlo approach to estimate statistical and systematic uncertainties on a parameter of interest. In the KATRIN context this is m_ν^2 . Ensemble Simulations are realized by performing the same fitting procedure over and over again with varying emulated measured data for each fit. For KATRIN, these emulated data will be created by the RUNGENERATOR. To achieve workable results ensemble simulations for KATRIN require repetitive runs in the order of 10^5 . Each run will yield a best-fit estimator for the squared neutrino mass \hat{m}_ν^2 which will be stored in a histogram like in figure 4.2. The standard deviation of a Gaussian which is fitted to such a histogram will show the statistical uncertainty of the KATRIN experiment σ_{stat} . Assuming that the ensemble simulation does not consider any systematic effects the Gaussian curve will have its mean value right at the point which has been fed as model input to the SPECTRUMSIMULATOR and the RUNGENERATOR. Therefore, in the context of this work, the absolute value for m_ν^2 is arbitrary and for reasons of simplicity chosen to be $m_\nu^2 = 0.0 \text{ eV}^2$. However, if the SPECTRUMSIMULATOR and the RUNGENERATOR are modeled with different assumptions, e. g. for the value of the total inelastic scattering cross section σ_{inel} , this will cause a shift of the Gaussian distribution away from $m_\nu^2 = 0.0 \text{ eV}^2$. The resulting shift Δm_ν^2 is the systematic uncertainty which arises from the different assumptions for both models. The KATRIN design report [KC05] has anticipated a total systematic uncertainty budget of

$$\sigma_{\text{sys,tot}} = \Delta m_\nu^2 \leq 0.017 \text{ eV}^2. \quad (4.11)$$

This value is broken down into five major systematic effects which means that a single systematic influence must not exceed

$$\Delta m_{\nu}^2 \leq 0.0075 \text{ eV}^2. \quad (4.12)$$

However, this value was an estimation at an early stage of the experiment which aggregated effects known at that time. With an ongoing progress on the preparation, construction and commissioning of the experiment further effects have been discovered which must be considered. Nevertheless, the given limits must not be exceeded. The systematic influence of the total inelastic scattering cross section is one of these factors which do not have their individual uncertainty budget. Therefore, the following paragraph gives an estimation on an acceptable systematic uncertainty induced by this parameter. Given an adequate benchmark value through an uncertainty budget, ensemble simulations are a good way to determine to which degree of precision certain relations need to be known and understood in order not to violate this requirement. In chapter 5 such an analysis is performed for the total inelastic scattering cross section.

Acceptable Systematic Uncertainty on the Total Inelastic Scattering Cross Section

Among the systematic effects which are explicitly mentioned in the design report the unfolding¹ of the energy loss function of electrons passing through the experimental setup and the monitoring of the column density ρd of the gaseous tritium are the ones which are most closely related to the total inelastic scattering cross section. This relation is mostly due to the importance of the total inelastic scattering cross section in the unfolding procedure (see subsection 3.3.6). The systematic uncertainty budgets for the unfolding procedure and the column density are

$$\Delta m_{\nu}^2(\text{unfolding}) < 6 \cdot 10^{-3} \text{ eV}^2 \quad (4.13)$$

$$\Delta m_{\nu}^2(\rho d) < \frac{\sqrt{5} \cdot 6.5}{10} \cdot 10^{-3} \text{ eV}^2 \approx 1.45 \cdot 10^{-3} \text{ eV}^2. \quad (4.14)$$

In total, this is a systematic uncertainty of

$$\sigma_{\text{sys}}(m_{\nu}^2) = 6.2 \cdot 10^{-3} \text{ eV}^2 \quad (4.15)$$

after a quadratic addition. The technical design report lists six individual effects for this uncertainty so the total inelastic cross section would be the seventh effect. Therefore, it is a reasonable assumption that the total inelastic cross section must at maximum contribute one seventh to this uncertainty. Consequently, the uncertainty budget for the total inelastic cross section is

$$\sigma_{\text{sys,max},\sigma_{\text{inel}}} \approx 2.3 \cdot 10^{-3} \text{ eV}^2 \quad (4.16)$$

in the scope of this work. This is very similar to the value estimated by [Gro15] for a single parameter using a different approach. In that work, the assumption was made that a single systematic effect (which is a sub-effect of one of the five major systematic effects) must not increase the total systematic uncertainty of the experiment by a fraction greater than 1 %.

¹The unfolding could either be a deconvolution or an extraction, see subsection 3.3.6.

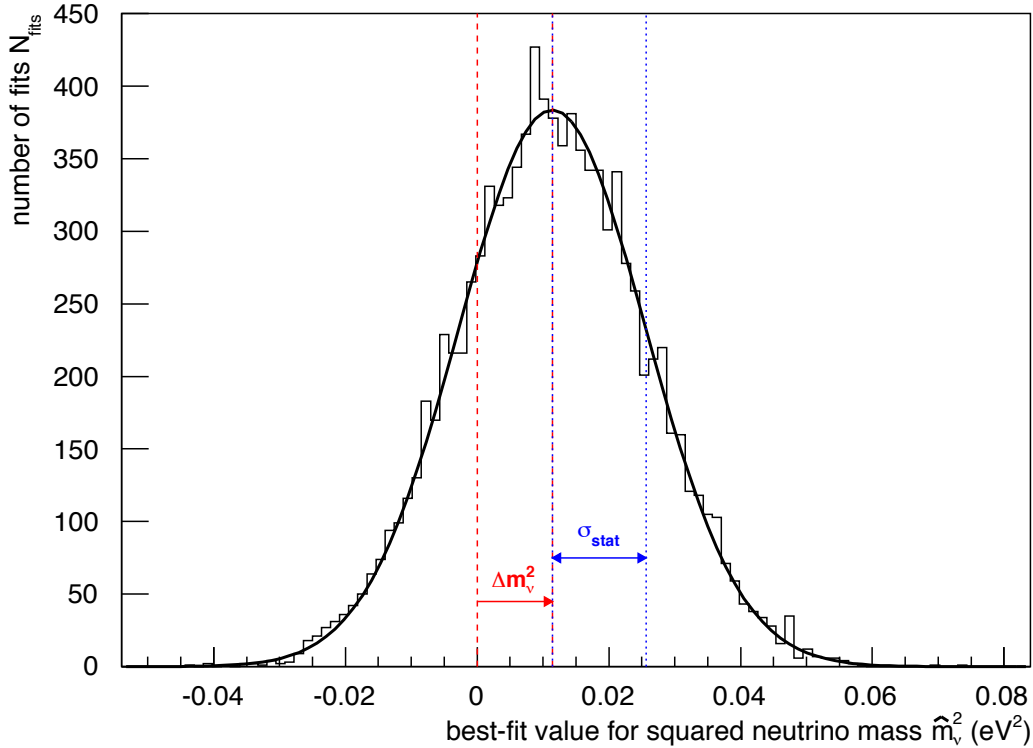


Figure 4.2.: **Exemplary histogram for a simulation of 10,000 KATRIN experiments.** This figure, which has been created according to [Hoe12], shows how statistic and systematic uncertainties can be read from a Gaussian fit to a histogram which has been generated as described in the main text. The histogram comprises the best-fit estimators \hat{m}_ν^2 for 10,000 simulations of the KATRIN experiment (equivalent to 30,000 full years of measuring time). To show the influence of a systematic effect the cross section σ_{inel} for inelastic scattering of electrons off tritium in the WGTS was intentionally set to different values for the SPECTRUMSIMULATOR and the RUNGENERATOR. The setup $\sigma_{\text{inel,spec}} = 3.40 \cdot 10^{-18} \text{cm}^2$ and $\sigma_{\text{inel,run}} = 3.37 \cdot 10^{-18} \text{cm}^2$ resembles a case where the experimenter assumes the total inelastic cross section to be $\sigma_{\text{inel}} = 3.40 \cdot 10^{-18} \text{cm}^2$ while the true value is $\sigma_{\text{inel}} = 3.37 \cdot 10^{-18} \text{cm}^2$. All other values were set according to design values as described in [KC05]. The false assumption regarding the value of the total inelastic scattering cross section will cause a systematic error of $\Delta m_\nu^2 \approx 0.011 \text{eV}^2$ to the experimenter's measurement result. The statistic error of $\sigma_{\text{stat}} \approx 0.014 \text{eV}^2$ in this example is not affected by the false assumption.

4.2.5. The Measuring Time Distribution

It has been shown that the squared neutrino mass is obtained through a minimization of equation 4.10. Free parameters of this minimization are the signal level R_S , the background level R_{bg} , the endpoint of the β -spectrum E_0 and the desired squared neutrino mass m_ν^2 . One way to optimize this fitting procedure (i.e. to reduce the uncertainty on m_ν^2) is to optimize the distribution of measuring time t_{qU} at different retarding energies qU . Preliminary simulations showed that there are better measuring time distributions than evenly allocating the full measurement time of three years to all retarding potentials. Three regions were identified [KC05] to which measurement time should be mostly allocated. Firstly, measurement time at high count rates at low retarding potentials was identified as best mean to determine the tritium endpoint of the integrated spectrum and the amplitude of the signal rate. Secondly, the region some eV below the endpoint, where the signal-to-background ratio is about 2:1, is suited best for an extraction of the squared neutrino mass parameter. Finally, measurements beyond the endpoint are required to determine the background rate. The top chart in figure 4.3 depicts the measuring time distribution as suggested by [KC05].

Recently, more research on the topic of an optimal measuring time distribution has been conducted by [Kle14]. The three rather extensive regions proposed by [KC05] were reduced to four more specific regions which are indicated in the middle chart of figure 4.3. Measuring at position (1) was identified as most efficient to determine the endpoint E_0 and signal amplitude R_S . Position (2) is used to break the correlation between R_S and E_0 . As suggested by [KC05] the new distribution also suggests to spend most measurement time close to the endpoint E_0 . Finally, the region above the endpoint (4) is, again, used to determine the background rate R_{bg} . To take into account that the endpoint is not precisely known to the current date, a Gaussian smearing has been applied to the measuring time distributions. This has led to the bottom chart in figure 4.3 with somewhat less distinct peaks in measuring time, especially around the endpoint region.

The measuring interval starting 30 eV below the endpoint has been chosen by [KC05] as it was considered the best trade-off between statistic and systematic uncertainties. A measuring interval of greater length would decrease statistic uncertainties but increase systematic uncertainties and vice versa. This assumption has been made for the total of all systematic uncertainties which has been assumed to be mainly dominated by background effects. In chapter 5 the work at hand will analyze if this assumption holds for the single systematic parameter σ_{inel} , the total inelastic scattering cross section. For this purpose, optimized measuring time distributions following the concept of [Kle14] are used. However, it is important to note that these distributions are optimized for statistical effects and have not considered any systematic influences yet.

4.3. KASSIOPEIA

The KASSIOPEIA simulation package can be considered the Monte Carlo counterpart to the analytic description of the KATRIN experiment which is modeled in the SSC package. Based on geometric structures provided by the KGEOBAG package and field simulations based on KEMFIELD, KASSIOPEIA is capable of tracking simulated

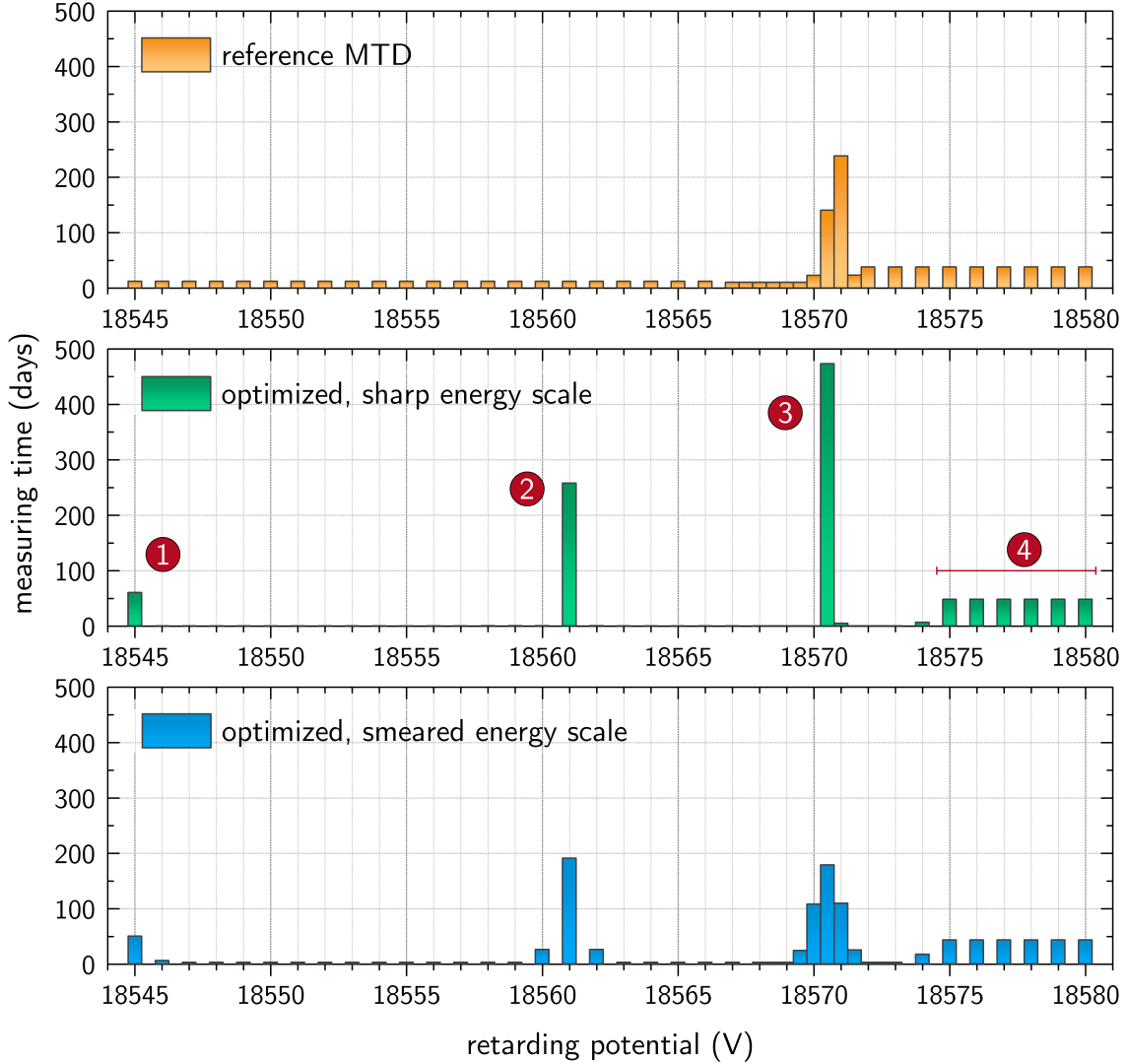


Figure 4.3.: **Comparison of different measuring time distributions.** The top illustration depicts the measuring time distribution as proposed in [KC05] for a measurement interval $[-30\text{ eV}, +5\text{ eV}]$. The second illustration shows the optimized distribution for a sharp energy scale as suggested by [Kle14] and points out the most important measurement points which are explained in the main text. Finally, the bottom chart shows the measuring time distribution optimized for a smeared energy scale. Illustrations taken from [Kle14].

electrons from the source to the detector. An exhaustive description of effects considered by KASSIOPEIA can be found in [Gro15]. The Monte Carlo simulations with KASSIOPEIA offer a powerful means to investigate different aspects of the KATRIN experiment in great detail. However, this gain in precision comes at the cost of computation time. As a compromise it is good practice to simulate parts of the experiment and refine the analytic model accordingly. In [Gro15] seven physical effects and their influence on the response function have been analyzed and the analytic model has been adjusted to reflect these effects.

The work at hand uses KASSIOPEIA to simulate scattering in the WGTS to generate the response function of the Rearsection electron gun (see chapter 6). An overview of how KASSIOPEIA simulates scattering is given in the following subsection.

4.3.1. The Simulation of Scattering

The KASSIOPEIA scattering package is written in a modular way. This way, elastic and inelastic processes can be turned on and off individually. For elastic scattering, the module relies on experimental data from [Nis85], [Liu94] and [Tra83]. Inelastic scattering can be either be simulated based on the analytic parameterization according to [Ase00] or simulations can be subdivided into excitation and ionization processes. In the latter case, excitation processes are simulated based on experimental data from [Arr80] and [Che95] while ionization is based on data from [Rud91]. The modularization allows for a very specific analysis in simulation runs.

Previous work [Pom14] has found that analytic response functions based on parameterizations from [Ase00] significantly deviate from response functions based on Monte Carlo simulations using experimental data as input for the total inelastic scattering cross sections. The difference persists even after adjusting the analytic function to the cross section based on experimental results (see fig. 4.4). In conclusion, [Pom14] found that a measurement of the inelastic cross section and an adjustment of the scattering module is necessary. The work at hand is preparing such a measurement by simulating the required electron gun analyses in chapter 6.

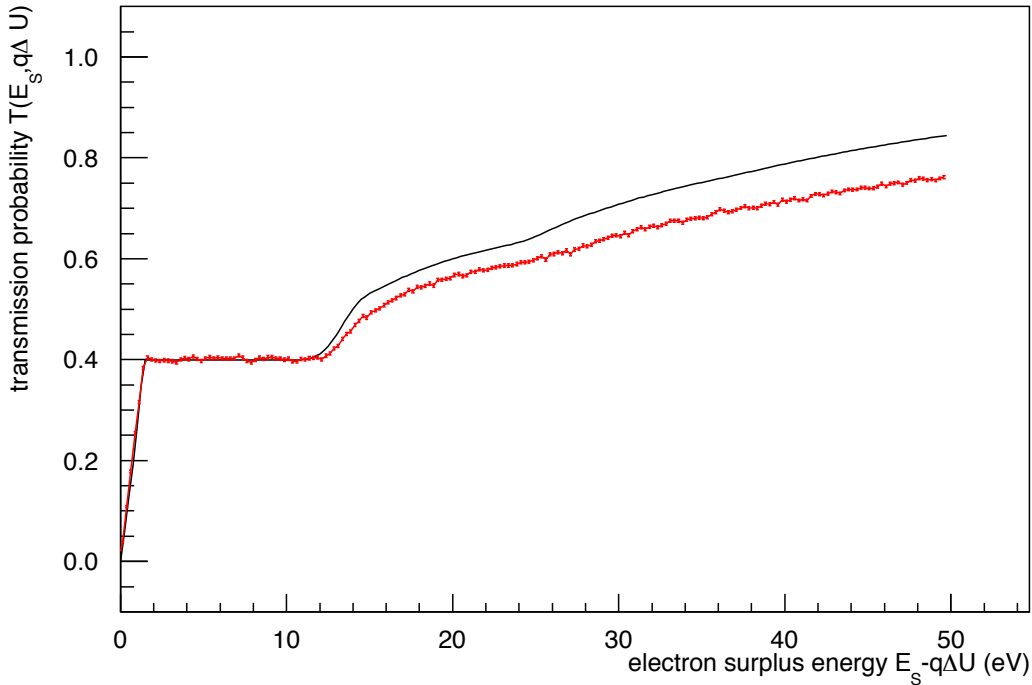


Figure 4.4.: **Comparison of a Monte Carlo-simulated response function (red dots) to an analytically calculated response function (black line).** The chart, which has been adapted from [Pom14], shows two response functions. The black line depicts an analytically calculated curve based on the parameterization by [Ase00] while the red dotted curve is based on Monte Carlo simulations. Both curves are based on a total inelastic scattering cross section of $\sigma_{\text{inel}} = 3.62 \cdot 10^{-18} \text{cm}^2$ based on multiple experimental sources, a column density $\rho d = 5 \cdot 10^{17} \text{cm}^{-2}$ and a maximum angle $\theta_{\text{max}} = 50.77^\circ$. The good agreement between both curves at the plateau level is due to the fact that inelastic scattering only occurs for electron surplus energies above 11 eV. Deviations between both curves show the necessity of further measurements regarding the energy loss through scattering.

5. Systematic Effects of Scattering in the WGTS

One of the most complex components of the KATRIN experiment in terms of systematic effects is the WGTS. Here, electrons emitted in the tritium β -decay scatter off other tritium molecules. The most important property regarding the scattering process is the inelastic cross section¹. In its differential form $\frac{1}{\sigma_{\text{inel}}} \frac{d\sigma_{\text{inel}}}{d\epsilon}$ it yields the energy loss function and in its integrated form σ_{inel} it determines the scattering probabilities. The work at hand focuses on the integrated form, the total inelastic cross section. It is of paramount importance to understand scattering processes as they will severely influence the shape of the integrated spectrum and therefore the final neutrino mass fit. Previous work has determined the total inelastic cross section with an precision of 2% [Ase00]. Since this degree of precision does not meet the KATRIN design requirements, the Rearsection electron gun has been designed to obtain a value of higher accuracy. Section 5.1 gives an overview of how wrong assumptions of the value of the total inelastic cross section can negatively influence the neutrino mass measurement. The following section 5.2 investigates how precise the measurement of the total inelastic cross section has to be in order to fulfill the KATRIN design requirements. It will turn out that the requirements on the precision of the total inelastic cross section are very ambitious. Thus, section 5.3 presents an approach to somewhat relax these requirements by adapting the lower boundaries of the analysis interval below the tritium endpoint. Section 5.4 uses the approach of section 5.3 and gives recommendations on the most suitable analysis intervals depending on the precision of a measurement of the total inelastic cross section. Section 5.5 concludes and gives an outlook on further research.

5.1. The Influence of σ_{inel} on the Neutrino Mass Measurement

The total inelastic cross section σ_{inel} of electrons scattering off tritium gas in the source is a systematic parameter of the KATRIN experiment. As described in section 3.3 it is the normalization factor for the energy loss function and determines

¹For reasons of readability the attribute “scattering” is omitted in the following chapter.

the scattering probabilities of electrons. In combination with the transmission function both of these parameters determine the response function of the KATRIN experiment. The response function on the other hand is of major importance for describing the integrated spectrum and fitting the experimental model to the measured data as described in section 4.2. It needs to be known precisely to achieve the desired degree of precision for the final neutrino mass measurement. Therefore, all experimental parameters must fulfill minimum requirements on their degree of uncertainty as described in subsection 4.2.4. The current literature value of $\sigma_{\text{inel}} = (3.40 \pm 0.07) \cdot 10^{-18} \text{cm}^2$, however, does not fulfill these requirements.

This section shows how the total inelastic cross section can influence the systematic uncertainty on the final neutrino mass measurement. For this purpose, ensemble simulations according to subsection 4.2.4 were performed and compared. Each ensemble simulation has been based on KATRIN standard parameters except for the total inelastic cross section. Additionally, the measuring time distribution has been optimized according to [Kle14] (see section 4.2.5). While the theoretical model in the SPECTRUMSIMULATOR fixes the total inelastic cross section at a reference value of $\sigma_{\text{inel}} = 3.40 \cdot 10^{-18} \text{cm}^2$, the RUNGENERATOR simulates the experiment with an unaccounted for shift in the total inelastic cross section of $\frac{\Delta\sigma_{\text{inel}}}{\sigma_{\text{inel}}}$. Thereby, it emulates a measurement where the true value for the total inelastic cross section is $\sigma_{\text{inel}} + \Delta\sigma_{\text{inel}}$. For each magnitude of the unaccounted for shift a histogram as in figure 4.2 has been generated for which the mean value of a Gaussian fit yields the resulting shift in the squared neutrino mass Δm_ν^2 . The evolution of the shifts in squared neutrino mass for different unaccounted for shifts in the total inelastic cross section is presented in figure 5.1. It shows that if the analytic model fixes the total inelastic cross section at a too high (low) reference value, the squared neutrino mass value derived from the spectral fit will be too high (low). The highest and lowest value of $\frac{\Delta\sigma_{\text{inel}}}{\sigma_{\text{inel}}} \approx \pm 2\%$ represent the “worst case scenario” for a shift in squared neutrino masses based on the reported values for the total inelastic cross section by [Ase00]. The dashed lines in the plot represent the acceptable systematic shift on the squared neutrino mass Δm_ν^2 induced by σ_{inel} as estimated in subsection 4.2.4. It is obvious that the fitted line for shifts in squared neutrino mass goes far beyond the acceptable range which emphasizes the need for a more precise measurement of the total inelastic cross section. The following section motivates how precise this measurement has to be.

5.2. Required Precision of a Measurement of σ_{inel}

As seen in section 5.1, the fitted line for shifts in squared neutrino masses crosses the limits according to subsection 4.2.4. Therefore, the intersection between the fitted curve across all systematic shifts and the dashed lines gives a limit on how precise the measurement result for σ_{inel} has to be at least in order to reduce the shift in squared neutrino mass to an acceptable limit. If the uncertainty on σ_{inel} was higher it would exceed the allowed limits.

At this point it seems reasonable to give a short distinction of symbols used throughout this chapter: The symbol Δ will always be used to denote the deviation of a value from its default value. An example is the shift of the squared neutrino mass Δm_ν^2 from its chosen value of 0.0eV^2 . As shown in subsection 4.2.4, this shift is

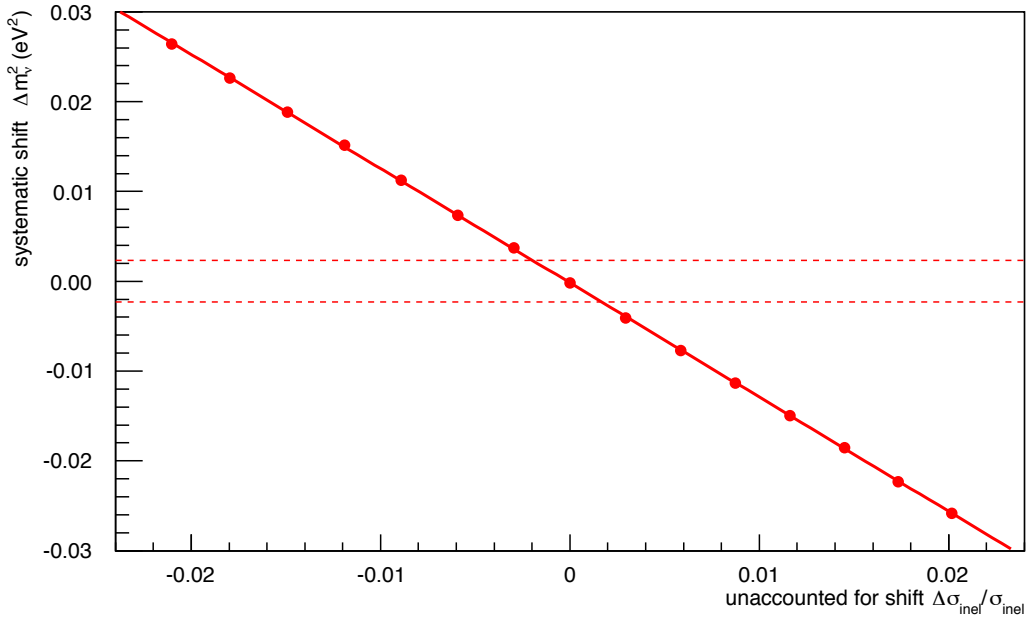


Figure 5.1.: **Systematic influence of σ_{inel} on the squared neutrino mass m_ν^2 for a lower boundary of the analysis interval at -30 eV .** This plot shows the systematic influence of a wrongly assumed σ_{inel} on the squared neutrino mass. The dashed lines depict the acceptable shift in the squared neutrino mass according to subsection 4.2.4. The intersection between the linear fit and the dashed lines is at approximately 0.002. For each point in the diagram the KATRIN experiment has been simulated at standard parameters for 100,000 times (equivalent to 300,000 full years of measuring time). This was sufficient to decrease the error bars on the simulated points to an extent which is not visible in this plot.

equivalent to the systematic uncertainty of the KATRIN experiment which is denoted by σ_{sys} . Accordingly, the statistical uncertainty of KATRIN is denoted by σ_{stat} . This statistical uncertainty can be reduced by adding more measuring time or by optimizing the measuring time distribution. It is not to be confused with the statistical uncertainty which arises from limited statistics of Monte Carlo simulations performed in the work at hand which is labeled with a δ . This can lead to an expression like $\delta\sigma_{\text{stat}}$, denoting the uncertainty (due to a limited number of Monte Carlo simulations) on the uncertainty (due to limited measurement time) on the measurement of the squared neutrino mass. Finally, there is the total inelastic cross section σ_{inel} which is commonly denoted by the same symbol, σ , and which must not be confused with statistical and systematic uncertainties.

To determine the intersections between the fitted curve across all systematic shifts and the dashed line the one-polynomial fitting function of ROOT [ROO15] was used to fit the data points. With b being the y-intercept and m being the slope of the fitted line it is

$$(\Delta m_{\nu}^2)_{\text{acceptable}} = m \cdot \left(\frac{\Delta\sigma_{\text{inel}}}{\sigma_{\text{inel}}} \right)_{\text{max}} + b \quad (5.1)$$

$$\left(\frac{\Delta\sigma_{\text{inel}}}{\sigma_{\text{inel}}} \right)_{\text{max}} = \frac{(\Delta m_{\nu}^2)_{\text{acceptable}} - b}{m} \quad (5.2)$$

with an uncertainty of

$$\delta \left(\frac{\Delta\sigma_{\text{inel}}}{\sigma_{\text{inel}}} \right)_{\text{max}} = \sqrt{\frac{1}{m^2}(\delta b)^2 + \left(\frac{(\Delta m_{\nu}^2)_{\text{acceptable}} - b}{m^2} \right)^2 (\delta m)^2}. \quad (5.3)$$

Here, $(\Delta m_{\nu}^2)_{\text{acceptable}}$ denotes the acceptable shift according to subsection 4.2.4 and $\left(\frac{\Delta\sigma_{\text{inel}}}{\sigma_{\text{inel}}} \right)_{\text{max}}$ is the maximally acceptable relative uncertainty on σ_{inel} which allows to stay within the acceptable range for a shift in the squared neutrino mass. It is important to point out that the uncertainty $\delta \left(\frac{\Delta\sigma_{\text{inel}}}{\sigma_{\text{inel}}} \right)_{\text{max}}$ only arises from the simulation. It results from the statistical uncertainty of individual data points. This uncertainty is based on the Monte Carlo simulations and can be reduced by an increased number of simulations. However, the corresponding error bars are so small that they are not visible in most of the plots of this chapter. Since there is an upper and a lower limit to the acceptable range for a shift of the squared neutrino mass there are two intersections, too. Consequently, there are always two values for $\left(\frac{\Delta\sigma_{\text{inel}}}{\sigma_{\text{inel}}} \right)_{\text{max}}$. However, if a measurement result for σ_{inel} will be reported it will most likely have a symmetric uncertainty. For this reason, the higher absolute value will be used as the maximally acceptable uncertainty on the total inelastic cross section. For figure 5.1 this is

$$\left(\frac{\Delta\sigma_{\text{inel}}}{\sigma_{\text{inel}}} \right)_{\text{max}} = (195 \pm 0.9) \cdot 10^{-5}. \quad (5.4)$$

In other words, the total inelastic cross section needs to be known to a precision of at least 0.2% in order not to exceed the limit on the shift in the squared neutrino mass. This is one order of magnitude more precise than the current literature value from [Ase00]. It is planned to use the Rearsection electron gun to determine the total

inelastic cross section with such a precision. To use the electron gun in an optimal way, simulations of this measurement process are performed in chapter 6. However, this aim is very ambitious. In case that future measurements cannot reach the necessary degree of precision it might be useful to somewhat relax the requirements on this precision. Therefore, the next section presents such an approach which eases the requirements on the precision of σ_{inel} at the cost of a somewhat higher statistical uncertainty.

5.3. Influence of the Analysis Interval on Systematic Effects

As shown in subsection 5.2 the Rearsection electron gun faces the challenging task of determining the total inelastic cross section with a precision of $\pm 0.2\%$. This requirement is based on an analysis interval starting 30 eV below the endpoint of the β -decay of tritium [KC05]. This value has been chosen as a trade-off between systematic and statistical effects. In this subsection it is shown how this choice might have to be adapted with regard to the impact of the total inelastic cross section.

Section 11.6 of the technical design report [KC05] states that shorter lengths for analysis intervals will decrease systematic uncertainties as displayed in figure 5.2 for an exemplary relative shift in the total inelastic cross section of $\frac{\Delta\sigma_{\text{inel}}}{\sigma_{\text{inel}}} \approx -2\%$. This is due to the fact that for greater analysis interval lengths systematic effects have a stronger influence on the response function. For example, do intervals of greater length account for electrons which have scattered more often than electrons accounted for in intervals with a shorter length. However, it is important not to neglect the statistical effects which result from a reduction of the length of the analysis interval. Figure 5.2 confirms the negative influence of shorter analysis interval lengths on statistical uncertainties.

To further investigate a potential trade-off between statistical and systematic uncertainties, simulations with different measuring time distributions have been performed to assess their influence on the requirements on the precision of the total inelastic cross section. Again, measurement times have been optimized with respect to statistical aspects according to [Kle14] and provided by Dr. Marco Kleesiek. Figure 5.3 shows optimized distributions for different analysis intervals. Appendix A lists all measuring time distributions used in this chapter.

For the work at hand analysis intervals have been varied by fixing the upper boundary at 5 eV above the tritium endpoint and only varying the lower boundary. Preliminary analyses have shown that lower boundaries between -30 eV and -15 eV are most promising. For this reason lower boundaries for simulations have been varied in steps of 1 eV within this region. In addition, lower boundaries of -40 eV, -35 eV, -10 eV and have been added. For each analysis interval the analysis described in subsection 5.2 has been repeated. The resulting systematic uncertainties for each interval are reported in figure 5.4. There is a trend towards higher acceptable uncertainties for shorter analysis interval lengths. In other words, when only looking on the systematic effect of the total inelastic cross section it is very desirable to have analysis intervals of shorter length in order to lower the need for very precise measurements of the total inelastic cross section. However, it is also notable that for analysis intervals of shorter length the statistical uncertainty (caused by Monte

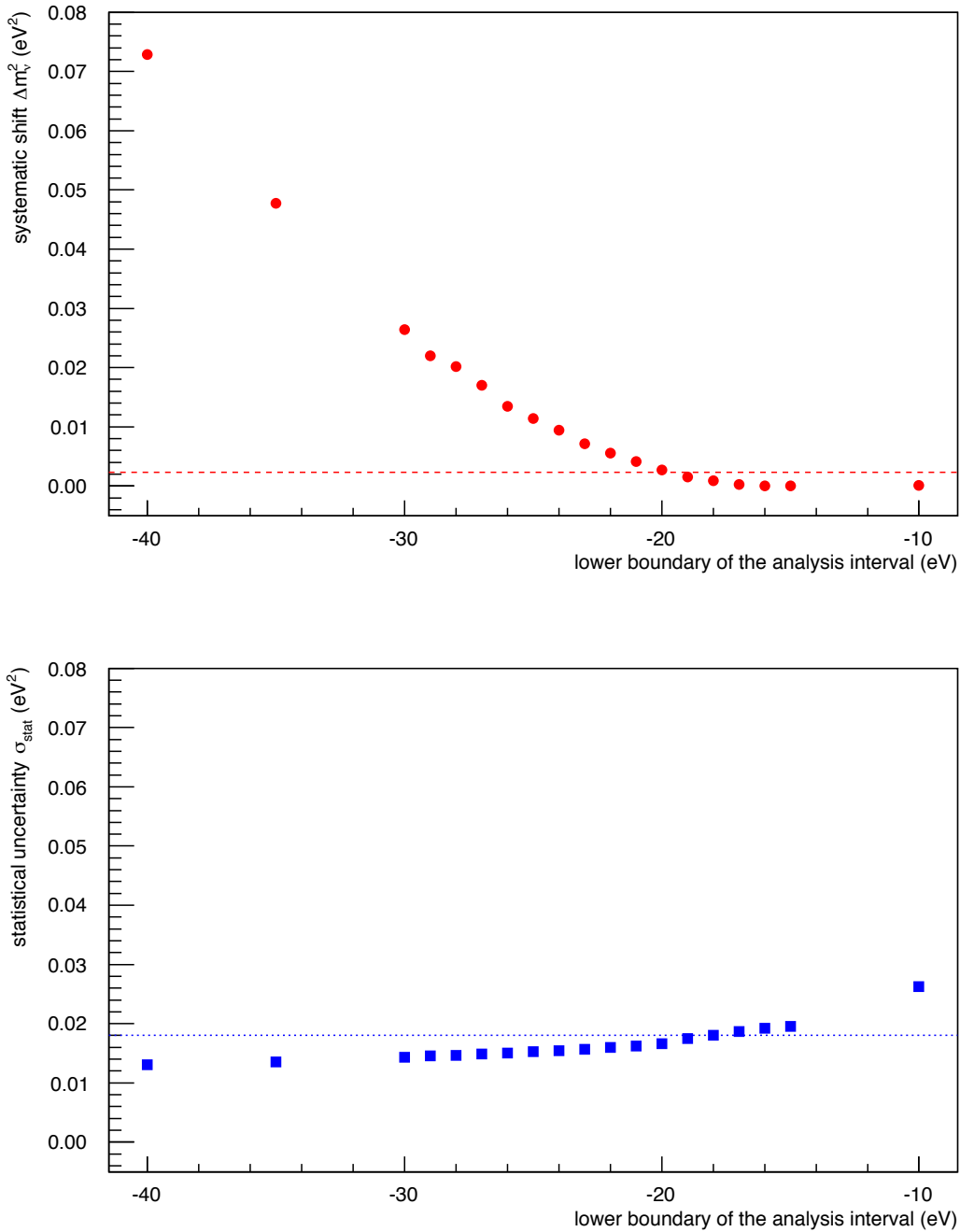


Figure 5.2.: **Systematic (top) and statistical (bottom) uncertainty on m_n^2 due to an unaccounted for relative shift on σ_{inel} of -2% for varying lower boundaries of the analysis interval.** The upper plot depicts the systematic effect of an unaccounted for relative shift of $\frac{\Delta\sigma_{\text{inel}}}{\sigma_{\text{inel}}} = -2\%$ for varying lower boundaries of the analysis interval. The lower plot shows the corresponding statistical uncertainty. The dashed line represents the acceptable limit for the systematic respectively statistical influence of the total inelastic cross section as derived in subsection 4.2.4. Each data point is based on 100,000 simulated KATRIN experiments (equivalent to 300,000 full years of measuring time). This was sufficient to decrease the error bars on the simulated points to an extent which is not visible in this plot.

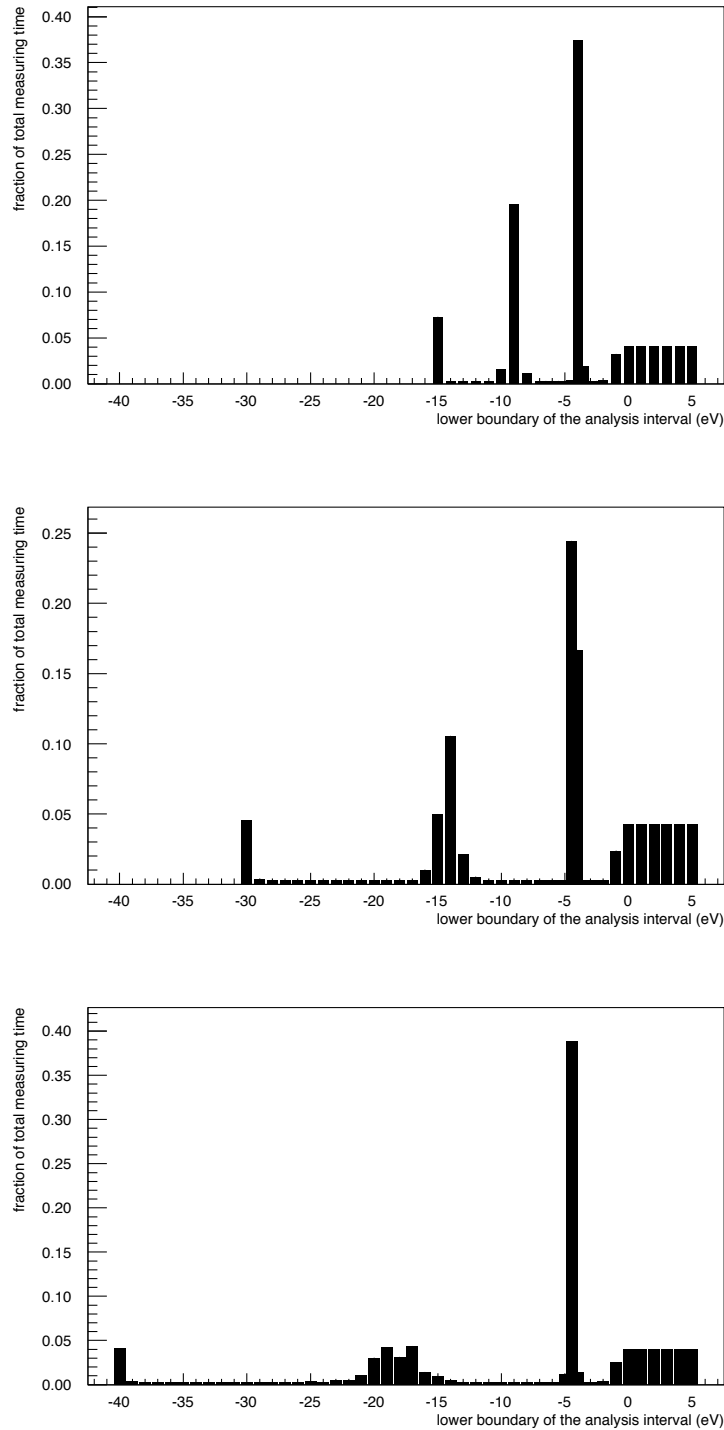


Figure 5.3.: **Comparison of measuring time distributions optimized for varying lower boundaries of the analysis interval.** The diagrams depict the distribution of the effective three years of measurement time for a lower boundary of the analysis interval of -15 eV (top), -30 eV (middle) and -40 eV (bottom) and an upper boundary of 5 eV above the endpoint of tritium β -decay. The four distinct regions to spend most of the available measuring time on (see section 4.2.5) are clearly visible. An exhaustive listing of measuring time distributions used in this work can be found in appendix A.

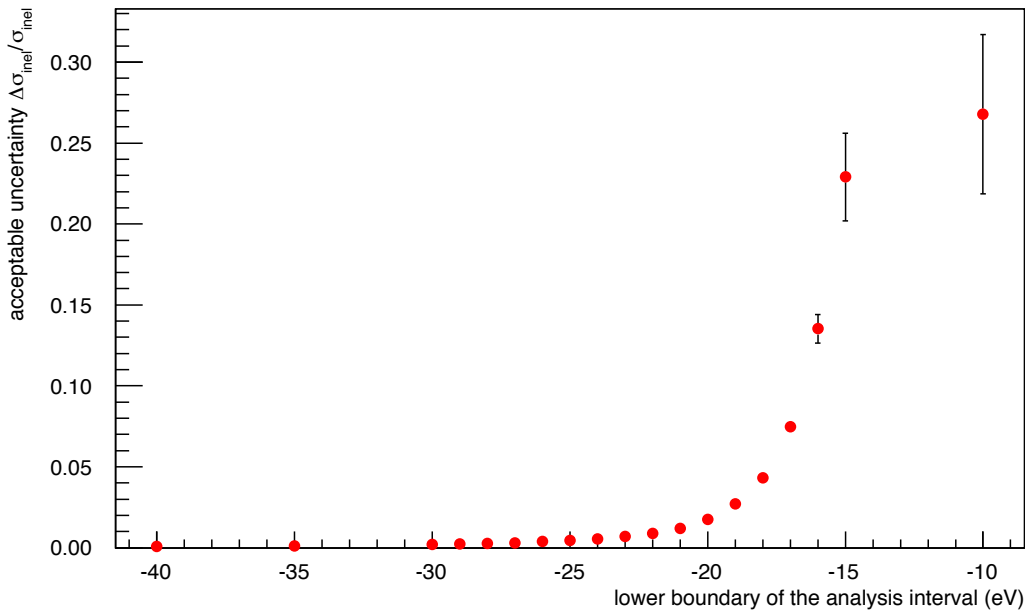


Figure 5.4.: **Acceptable uncertainty for varying lower boundaries of the analysis interval.** This figure shows how precise the measurement of the total inelastic cross section must be for varying lower boundaries of the analysis interval. For every point in the diagram the analysis described in section 5.1 was repeated, i. e. each point is based on 100,000 simulated KATRIN experiments (equivalent to 300,000 full years of measuring time). A trend towards higher acceptable uncertainties of σ_{inel} for shorter analysis intervals can be seen. The uncertainty for analysis intervals with a lower boundary above -17 eV is considerably higher due to the limited amount of simulations.

Carlo simulations) on the acceptable uncertainty rises. This is due to the method of fitting a line to the data points: with reduced lengths of the analysis intervals the influence of the total inelastic cross section diminishes whereas at the same time statistical uncertainties due to Monte Carlo simulations become more prominent compared to the value of the shift in the squared neutrino mass. This makes it harder for the ROOT fitting algorithm to find a definitive trend. Therefore, fitting results are reported with a higher uncertainty (see figure 5.5).

Overall, figure 5.4 is in accordance with the statements of the design report which have been reproduced in figure 5.2: if the systematic influence of the total inelastic cross section on the squared neutrino mass is comparatively low then it is acceptable to know it to a lesser degree of precision.

Finally, it is most important for the KATRIN experiment to know the combined uncertainty for different lower boundaries of the analysis intervals. This is plotted in figure 5.6 where the contributions of statistical and systematic uncertainty have

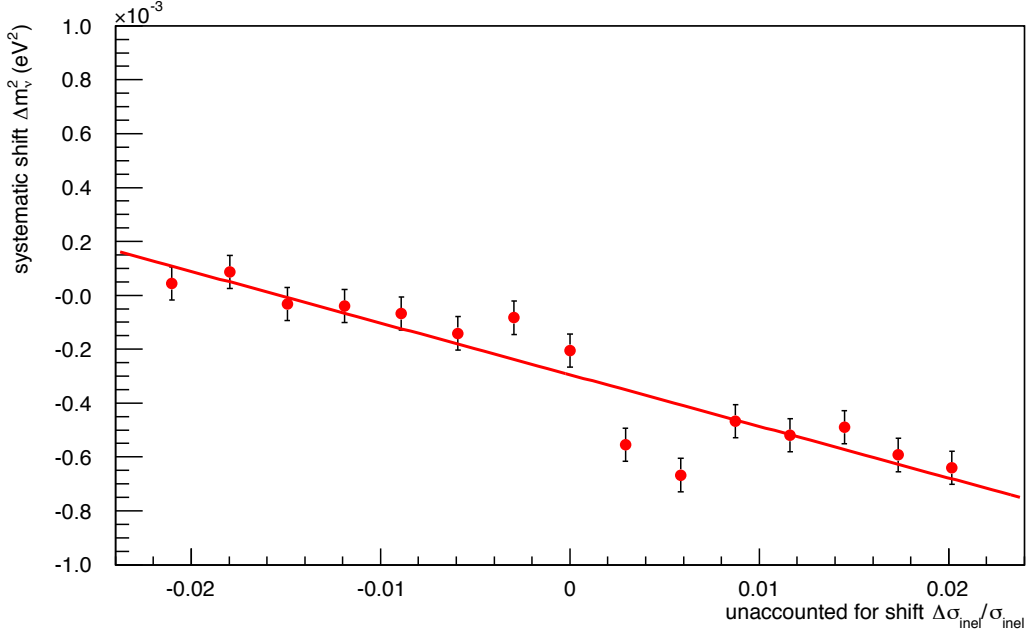


Figure 5.5.: **Systematic influence of σ_{inel} on m_ν^2 for a lower boundary of the analysis interval of -16 eV.** This plot is the equivalent to the analysis for figure 5.1 but with lower boundary of the analysis interval of -16 eV. Mind the scale of the y-axis. It can be seen that statistical uncertainties due to Monte Carlo simulations become more prominent compared to the value of the shift in the squared neutrino mass.

been added quadratically:

$$\sigma_{\text{com}} = \sqrt{\sigma_{\text{sys}}^2 + \sigma_{\text{stat}}^2} , \quad (5.5)$$

$$\delta\sigma_{\text{com}} = \sqrt{\frac{\sigma_{\text{sys}}^2 \cdot (\delta\sigma_{\text{sys}})^2}{\sigma_{\text{sys}}^2 + \sigma_{\text{stat}}^2} + \frac{\sigma_{\text{stat}}^2 \cdot (\delta\sigma_{\text{stat}})^2}{\sigma_{\text{sys}}^2 + \sigma_{\text{stat}}^2}} . \quad (5.6)$$

Furthermore, it is important to see the influence of the total inelastic cross section on the upper limit for the neutrino mass L . This has not only to consider the systematic effects of the total inelastic cross section alone but the remaining systematic effects as well. For a conservative estimation, these effects are considered to be at the upper limit of their uncertainty budget

$$\sigma_{\text{sys,tot}} = \sqrt{\sigma_{\text{remaining}}^2 + \sigma_{\text{sys,max},\sigma_{\text{inel}}}^2} = 0.017 \text{ eV}^2 \quad (5.7)$$

where $\sigma_{\text{sys,max},\sigma_{\text{inel}}} = 2.3 \cdot 10^{-3} \text{ eV}^2$ is the maximal acceptable systematic uncertainty due to the total inelastic cross section (see subsection 4.2.4). Consequently, it is $\sigma_{\text{remaining}} \approx 16.8 \cdot 10^{-3} \text{ eV}^2$. Statistical uncertainties are not influenced by further systematic effects. They only dependent on the lower boundary of the analysis interval. Consequently, for the statistical uncertainty the same values as in figure 5.2

can be used. The total uncertainty is

$$\sigma_{\text{tot}} = \sqrt{\sigma_{\text{sys,tot}}^2 + \sigma_{\text{stat}}^2} \quad (5.8)$$

$$= \sqrt{\sigma_{\text{remaining}}^2 + \sigma_{\text{sys}}^2 + \sigma_{\text{stat}}^2} \quad (5.9)$$

where the index ‘‘inel’’ has been omitted for readability. Taking this into account the upper limit for the neutrino mass L is

$$L(90\% \text{C. L.}) = \sqrt{1.64 \cdot \sigma_{\text{tot}}}, \quad (5.10)$$

$$\delta L = \sqrt{0.41 \left(\frac{\sigma_{\text{sys}}^2 \cdot (\delta\sigma_{\text{sys}})^2}{\sqrt{(\sigma_{\text{sys}}^2 + \sigma_{\text{stat}}^2 + \sigma_{\text{remaining}}^2)^3}} + \frac{\sigma_{\text{stat}}^2 \cdot (\delta\sigma_{\text{stat}})^2}{\sqrt{(\sigma_{\text{sys}}^2 + \sigma_{\text{stat}}^2 + \sigma_{\text{remaining}}^2)^3}} \right)} \quad (5.11)$$

which is depicted in figure 5.7. This plot emphasizes the importance of the total inelastic cross section: in case that the knowledge on the total inelastic cross section does not improve significantly the design goal might be missed when measuring with an analysis interval with a lower boundary at -30 eV. Above this, figure 5.6 and figure 5.7 yield the same result: for a scenario of an unaccounted for relative shift of $\frac{\Delta\sigma_{\text{inel}}}{\sigma_{\text{inel}}} \approx -2\%$ an analysis interval with a lower boundary at -21 eV is much more favorable than an interval starting at -30 eV as it results in a lower combined uncertainty². The following section will extend the analysis to further values of unaccounted for shifts in the total inelastic cross section.

5.4. Recommended Analysis Intervals

Section 5.3 has stated that for an unaccounted for relative shift of $\frac{\Delta\sigma_{\text{inel}}}{\sigma_{\text{inel}}} \approx -2\%$ an analysis interval starting at -21 eV is optimal. However, this is only true for this special unaccounted for shift. Probing the entire uncertainty interval of the total inelastic cross section reported by [Ase00] shows that different lower boundaries of the analysis intervals are optimal depending on the precision of future measurements of the total inelastic cross section.

It turns out that the lowest combined uncertainty is not always as unambiguous as it is for an unaccounted for relative shift of $\frac{\Delta\sigma_{\text{inel}}}{\sigma_{\text{inel}}} \approx -2\%$. For other analysis intervals statistical error bars (due to Monte Carlo simulations) on the lowest point can overlap with error bars of other points. Furthermore, the best analysis interval for an unaccounted for positive shift might be different from the best interval for a negative relative shift of the same magnitude³. Increasing the number of simulations by one order of magnitude in the course of this work has significantly improved yet not fully cleared out this situation. Therefore, table 5.1 recommends ranges of analysis intervals for various possible uncertainties of future measurements of the total

²Even though it is not visible in figure 5.6 the combined uncertainty for an analysis interval starting at -21 eV is clearly the lowest. The statistical error bar (due to Monte Carlo simulations) on the combined uncertainty does not overlap with any other statistical error bars on other combined uncertainties. This does not hold for all analysis intervals and will be considered in section 5.4.

³For example, this applies for the unaccounted for relative shift of $\frac{\Delta\sigma_{\text{inel}}}{\sigma_{\text{inel}}} \approx -2\%$ where results are not as unambiguous for $+2\%$.

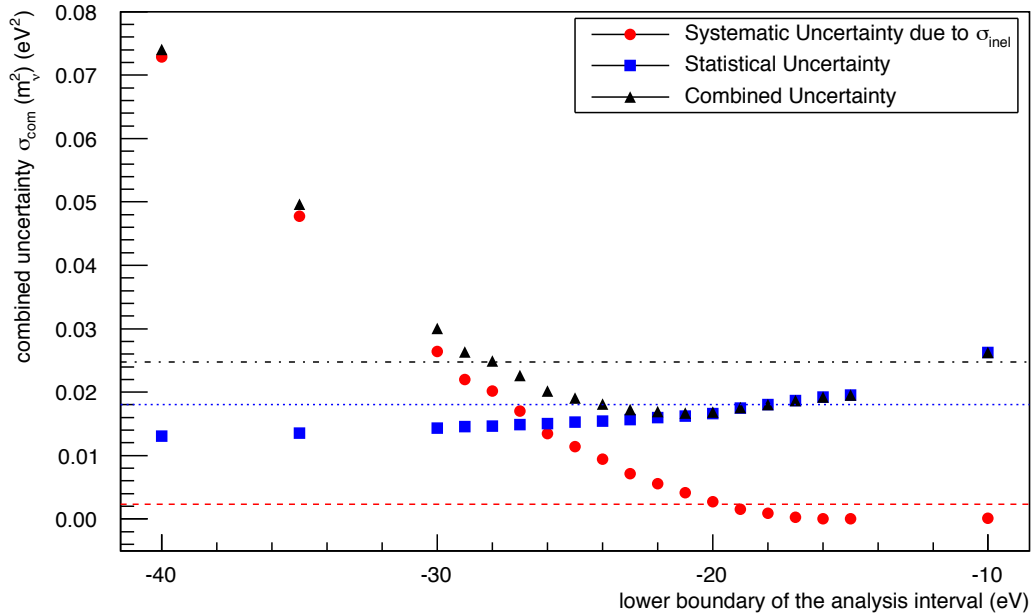


Figure 5.6.: **Systematic, statistical and combined uncertainty for varying lower boundaries of the analysis interval.** The plot combines systematic uncertainties (red dots) and statistical uncertainties (blue squares) by adding them quadratically to a combined uncertainty (black triangles). The dashed red line shows the acceptable systematic uncertainty on the total inelastic cross section (see subsection 4.2.4), the blue dotted line the limit for statistical uncertainty and the black dash-dotted line the total limit of uncertainty (both set by [KC05]). Here, an unaccounted for relative shift of $\frac{\Delta\sigma_{\text{inel}}}{\sigma_{\text{inel}}} = -2\%$ has been assumed. For each analysis interval the systematic and statistical uncertainty are based on 100,000 simulated KATRIN experiments (equivalent to 300,00 full years of measuring time). It can be seen that a lower boundary of the analysis interval of -30 eV is not optimal in this case and that a lower boundary of -21 eV would yield better results with regard to the combined uncertainty.

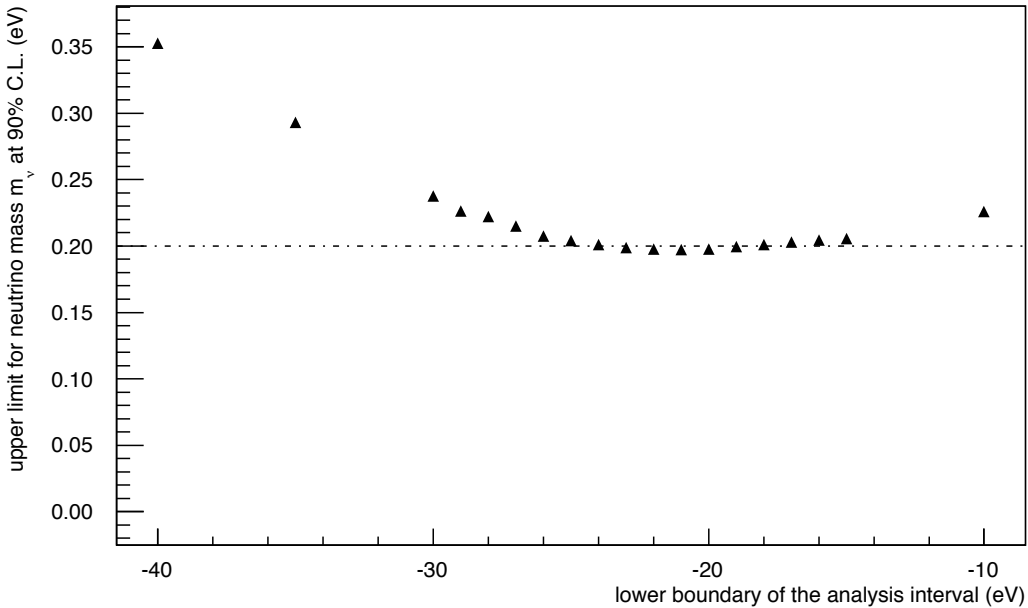


Figure 5.7.: **Upper limit for neutrino mass at 90 %C.L. for varying lower boundaries of the analysis interval.** The plot shows which upper limit for a neutrino mass at 90 %C.L. could be reached given that all systematic effects besides the total inelastic cross section are at their maximum uncertainty budget. The black dash-dotted line depicts the design goal for an upper limit set by [KC05]. Here, an unaccounted for relative shift of $\frac{\Delta\sigma_{\text{inel}}}{\sigma_{\text{inel}}} = -2\%$ has been assumed. For each lower boundary of the analysis interval the systematic and statistical uncertainty are based on 100,000 simulated KATRIN experiments (equivalent to 300,000 full years of measuring time). It can be seen that a lower boundary of the analysis interval of -30 eV would miss the design goal when all systematic effects but the total inelastic cross section are at their maximal uncertainty budget. A lower boundary of -21 eV would yield the best result in this case.

Table 5.1.: **Recommended lower boundaries of the analysis interval in case of different uncertainties on σ_{inel} .** This table summarizes the findings on which lower boundaries of analysis intervals should be considered in case of various outcomes for a measurement of the total inelastic cross section. For further explanations see the main text.

Relative uncertainty on σ_{inel} in a future electron gun measurement	Recommended lower boundary of the analysis interval for a neutrino mass measurement (eV)
0.3 %	-30
0.6 %	-26
0.9 %	-23, -24, -25
1.2 %	-22, -23
1.5 %	-22, -23
1.8 %	-21, -22
2 %	-20, -21, -22

inelastic cross section. Nevertheless, it is important to emphasize that statistical uncertainties due to Monte Carlo simulations are an issue of computation time. Given that a new uncertainty on the total inelastic cross section is reported, simulations could simply be re-run with an even higher number of emulated experimental runs in order to find a definitive recommendation.

5.5. Conclusion and Outlook

In the scope of this chapter the influence of the uncertainty on the total inelastic cross section of tritium in the WGTS on the uncertainty on the neutrino mass measurement at KATRIN has been analyzed. By assuming a conservative scenario for uncertainties of further systematic effects it has been simulated with current models that the uncertainty on the total inelastic cross section [Ase00] and the currently planned analysis interval below the tritium endpoint are not compatible with the envisaged sensitivity of the KATRIN experiment (see figure 5.7). For the currently planned analysis interval of $[-30 \text{ eV}, +5 \text{ eV}]$ around the tritium endpoint a precision on the total inelastic cross section of 0.2 % is required. Furthermore, simulations have been performed which recommend different analysis intervals in the case of various uncertainty levels on the total inelastic cross section (see table 5.1). However, it is important to point out that the performed simulations only account for one systematic effect and ignore any other systematic effect. This is of course an unrealistic scenario. However, in analyzing the systematic effects of the total inelastic cross section an approach has been developed which can be applied to other systematic effects, too. A more holistic approach which the work at hand recommends to be subject of further research could operate through two steps. First, other systematic effects should be analyzed in the same manner as the total inelastic cross section and added to the combined uncertainty presented in figure 5.6. The work at hand can be seen as a blue print for this. With new combined uncertainties, table 5.1 could be re-calculated which would lead to new recommendations for analysis intervals. Additionally, the analysis of further systematic effects would yield more realistic

assumptions for the calculation of an upper limit to the neutrino mass at KATRIN of 0.2 eV at 90 %C.L. than the assumptions made for figure 5.7. This has also been proposed at the 28th KATRIN Collaboration Meeting [SM15]. A subsequent second step should take into account possible correlations between systematic effects which might even lead to desirable situations like two systematic effects partially canceling each other. Preliminary investigations on such an effect have been performed [Hoe12].

6. Simulation of Electron Gun Measurements

Chapter 5 provides an in-depth analysis on why the total inelastic cross section¹ needs to be known with a precision of 0.2%. It is one of the tasks of the Rearsection electron gun to determine the total inelastic cross section with this precision. For this purpose, it generates an electron beam targeting from behind the WGTS into the experimental setup. The beam is guided by magnetic and electric fields just like electrons generated from tritium decay. The response function is measured by stepping the retardation voltage of the spectrometer and counting the electrons which reach the detector. In its shape, the electron gun response function differs from the response function for the KATRIN experiment² shown in figure 3.6. Section 6.1 describes why response functions of the electron gun are different from response functions of electrons with an isotropic angular distribution from the source. The following section 6.2 describes how response functions of the electron gun have been simulated in the course of the work at hand and results are analyzed. Section 6.3 explains how electron gun measurements could be used to determine the total inelastic cross section and estimates how long such a measurement would take. Section 6.4 concludes and gives an outlook on further research.

6.1. The Response Function of the Electron Gun

At first, it is important to understand the differences between the response function of the KATRIN experiment (see figure 3.6) and the response function of the electron gun at various setups (see figures 6.3 to 6.5). It should be noted that figure 3.6 is based on an analytic function while figures 6.3 to 6.5 are based on Monte Carlo

¹For reasons of readability the attribute “scattering” is omitted in the following chapter.

² At this point, it is important not to confuse terminology: There is a transmission function and a response function for electrons emitted by tritium which are usually referred to as *the* transmission function and *the* response function. Since electrons from the electron gun experience the same effects as electrons from the source there is a transmission and a response function for them, too. However, due to their sharp angular distribution, their shape differs from the regular transmission and response function which is why these functions must not be confused.

simulations. Hence, the former is a line while the latter consist of individual points. Beyond this, there are three major arguments for the distinction in the two shapes of response functions:

The first argument is related to the transmission function which is a major component of the response function according to section 3.3. Its rise to the plateau level (see figure 6.1) is much steeper for electrons emitted by an electron gun with a sharp angular distribution than for electrons emitted by the tritium source with an isotropic angular distribution. This can be explained by the relation

$$E_{\text{tr}} = \frac{q(U_A - U_S)}{1 - \sin^2 \theta_S \cdot \frac{B_A \cdot (\gamma_S + 1)}{B_S \cdot (\gamma_A + 1)}} \quad (6.1)$$

for an electron with a starting polar angle θ_S and starting energy E_S (compare subsection 3.3.2). When the combination of starting angle θ_S and starting energy E_S of the electrons exceeds the required transmission energy E_{tr} , electrons are transmitted. Accordingly, the transmission function for the electron gun has the form of a Heaviside function which influences the response function. However, the response function of the electron gun in figures 6.3 to 6.5 does not show a sharp step rise. This is due to uncertainties in the parameters θ_S and E_S which broaden the slope of the electron gun transmission function. Nevertheless, the rise is steeper than for the regular response function (compare figure 6.1).

The second argument for differences between the response functions is also related to the transmission function: for higher starting angles θ_S , transmission does not start at electron surplus energies $E_S - q\Delta U > 0$ eV but at higher energies. This can be explained by the longitudinal momentum component of the electron beam which decreases for increasing starting angles θ_S . For a constant starting energy $E_S = q\Delta U$ transmission is only possible at $\theta_S = 0^\circ$ because the entire momentum is longitudinal and directed towards the retarding potential ΔU . For higher starting angles θ_S , there is a perpendicular component of the momentum which the MAC-E filter can not fully convert into longitudinal momentum due to its limited energy resolution (see equation 3.8). To achieve a transmission, the starting energy E_S needs to be increased which means that transmission starts at higher electron surplus energies $E_S - q\Delta U$ (see the red dashed line in figure 6.1).

Finally, scattering probabilities according to

$$P_i(z, \theta) = \frac{(\lambda(z, \theta) \cdot \sigma_{\text{inel}})^i}{i!} e^{-\lambda(z, \theta) \cdot \sigma_{\text{inel}}} \quad (6.2)$$

also influence the response function (compare subsection 3.3.3). The plateau of the electron gun response function is generally much lower (about half the height) than for a regular response function. This is due to the fact that electrons from the electron gun will always have to pass the entire WGTS. On the other hand, electrons emitted by tritium are on average emitted in the middle of the WGTS. Therefore, they effectively have to cover only half of the distance and the effective tritium column density $\lambda(z, \theta)$ they have to traverse is reduced by about a factor of 2 compared to electrons emitted the electron gun. For a given setting of the retardation potential they are less likely to scatter which means that they are more likely to be transmitted. A comparison of figure 3.6 and figures 6.3 to 6.5 reveals this effect.

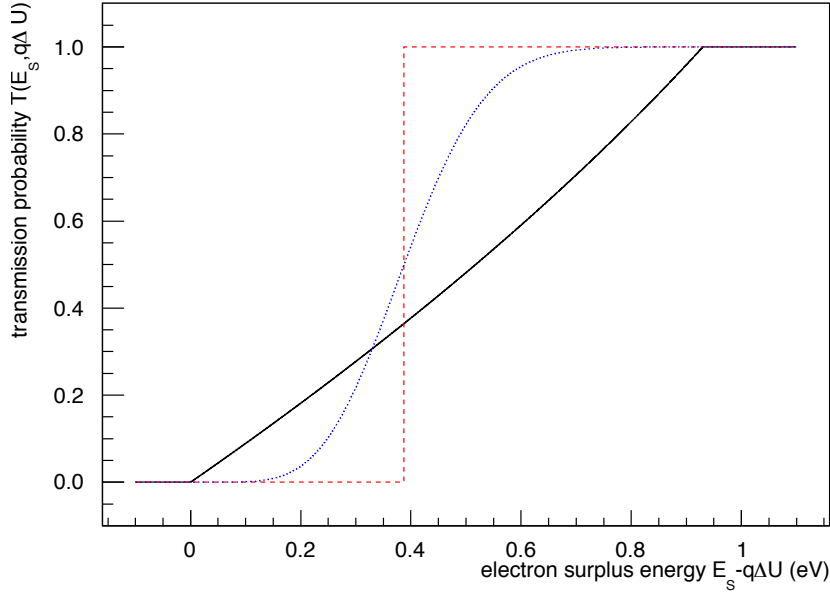


Figure 6.1.: **Comparison of analytic transmission functions.** The illustration compares different transmission functions. The black line illustrates the regular analytic transmission function for the KATRIN experiment as described in figure 3.4. It has been calculated for the isotropic emission of electrons and with a cut-off due to the magnetic mirror effect at $\theta_{\max} \approx 51^\circ$. The red dashed line shows the analytic transmission function of an electron gun at a fixed angle of $\theta_S = 30^\circ$ and at a sharp energy of $E_S = 18600 \text{ keV}$. Due to the sharp energy it has the shape of a Heaviside function. Furthermore, due to the fixed angle, transmission is only possible for electron surplus energies of $E_S - q\Delta U \gtrsim 0.4 \text{ eV}$. More realistic is the blue dotted line which incorporates a spread of the starting angle $\theta_S = (30 \pm 5)^\circ$ and therefore smears out the step function. A similar effect would occur for a smeared energy distribution E_S .

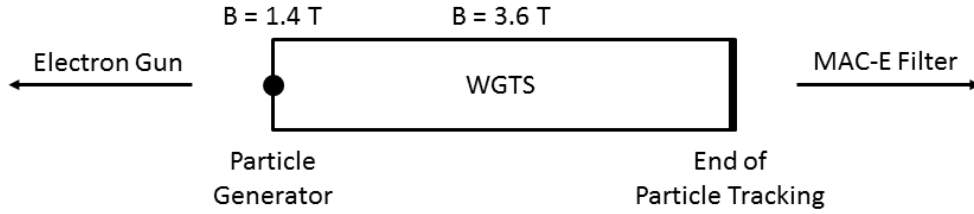


Figure 6.2.: **The schematic setup of KASSIOPEIA simulations for this chapter.**

For simulations particles with polar angles $\theta_S \pm \sigma_{\theta_S}$ and energies $E \pm \sigma_E$ according to table 6.2 are started by a particle generator. Since the electron gun angles have been reported for a magnetic field strength of $B = 3.6$ T [Bab14] they have converted for the magnetic field strength at the position of the particle generator $B = 1.4$ T. In order to save computation time, the simulation is stopped at the end of the WGTS and transmission through the spectrometer is calculated analytically.

6.2. Simulation of Electron Gun Response Functions

The following subsections describe simulations of the electron gun response function which have been simulated using KASSIOPEIA. Subsection 6.2.1 describes which parameters have been used for these simulations and subsection 6.2.2 describes the setup of the simulations. Results are summarized in subsection 6.2.3.

6.2.1. Simulation Parameters

The work at hand uses KASSIOPEIA to simulate response functions of the Rearsection electron gun. To gain an understanding of the transmission behavior of the electron gun various setups are simulated:

- Various values of the column density³ of tritium in the WGTS (see figure 6.3),
- Various starting polar angles of electron gun electrons (see figure 6.4),
- Various spreads of the electron gun beam energy (see figure 6.5)

The parameters for modeling the electron gun have been introduced in subsection 3.3.5. It is important to note that electron polar angles have been simulated for a magnetic field strength of 3.6 T [Bab14]. However, the magnetic field strength at the entrance of the WGTS, where the simulation starts, is only about 1.4 T (see figure 6.2). Therefore, a transformation of the electron angles is required.

The conservation of orbital magnetic moment μ during an adiabatic transition from 3.6 T to 1.4 T causes θ , the angle between electron momentum and field lines, to

³In case of a homogeneous gas distribution within the WGTS, the integral in equation 3.24 simplifies to the product ρL or following a common convention of notation ρd .

Table 6.1.: **Conversion of electron angles due to different magnetic field strengths.** This table shows the conversion of electron emission angles at a magnetic field strength of 3.6 T at the center of the WGTS to angles at 1.4 T at the entrance of the WGTS (see figure 6.2). The spreads of the angles have been linearly interpolated (compare subsection 3.3.5).

$\theta_S \pm \sigma_{\theta_S}$ at 3.6 T ($^\circ$)	$\theta_S \pm \sigma_{\theta_S}$ at 1.4 T ($^\circ$)
1.80 ± 0.73	1.12 ± 0.46
12.50 ± 1.04	7.76 ± 0.64
25.00 ± 1.40	15.28 ± 0.82
37.50 ± 1.76	22.31 ± 0.95
51.20 ± 2.16	29.08 ± 0.98

change. In good approximation, the orbital magnetic moment μ of an electron with cyclotron energy E_\perp is constant

$$\mu = \frac{E_\perp}{B} = \text{const} . \quad (6.3)$$

For a transition between two magnetic fields it follows that

$$\theta_2 = \arcsin \sqrt{\frac{B_2}{B_1} \sin^2 \theta_1} \quad (6.4)$$

which shows how θ transforms. This transformation has been performed for a selection of angles summarized in table 6.1. Uncertainties on the parameter have been transformed by transforming the upper and lower limit of the interval. When the uncertainty resulted into different upper and lower limits at 1.4 T the larger deviation has been used. All simulation parameter setups are summarized in table 6.2.

6.2.2. Simulation Design

To simulate the Rearsection electron gun, KASSIOPEIA has been set up as follows: the electron gun itself has been implemented as a particle generator at the beginning of the WGTS (see figure 6.2) with different parameter setups 1 to 11 which are listed in table 6.2. The parameters have been implemented as their values with their uncertainties as σ -values of a Gaussian distribution. For all response functions in this section approximately 10^6 electrons have been generated, tracked and evaluated. Elastic scattering in the WGTS has been implemented based on experimental data from [Nis85], [Liu94] and [Tra83], while inelastic scattering has been parameterized according to [Ase00] (see subsection 4.3.1). In order to save computation time, tracking is stopped at the exit of the WGTS (see figure 6.2). Here, each simulated particle is analyzed at a set retardation potential. For this purpose

$$\theta_{\text{tr}}(E_F) = \arcsin \sqrt{\frac{E_F - q(U_A - U_S)}{E_F} \frac{B_F \cdot (\gamma_A + 1)}{B_A \cdot (\gamma_S + 1)}} \quad (6.5)$$

is calculated for the final energy E_F of the electron at the end of the WGTS. U_S is the potential of the WGTS and B_F the magnetic field strength at the end of the

Table 6.2.: **Parameter setups for electron gun simulations.** This table summarizes all parameter setups which have been considered for electron gun simulations. About 10^6 electrons have been simulated per setup to sample the shape of the electron gun response function. For an explanation of the uncertainties on the parameters see subsection 3.3.5.

Setup (no.)	Simulation Settings		
	ρd (10^{17} cm^{-2})	$\theta_S \pm \sigma_{\theta_S}$ at 1.4 T ($^\circ$)	$E \pm \sigma_E$ (eV)
1	5.00	1.12 ± 0.46	18600 ± 0.107
2	3.75	1.12 ± 0.46	18600 ± 0.107
3	2.50	1.12 ± 0.46	18600 ± 0.107
4	1.25	1.12 ± 0.46	18600 ± 0.107
5	0.05	1.12 ± 0.46	18600 ± 0.107
6	5.00	7.76 ± 0.64	18600 ± 0.107
7	5.00	15.28 ± 0.82	18600 ± 0.107
8	5.00	22.31 ± 0.95	18600 ± 0.107
9	5.00	29.08 ± 0.98	18600 ± 0.107
10	5.00	1.12 ± 0.46	18600 ± 0.132
11	5.00	1.12 ± 0.46	18600 ± 0.256

WGTS. B_A is the magnetic field strength at the analyzing plane of the spectrometer. γ_S and γ_A are the Lorentz-factors in the source and at the analyzing plane. For a thorough explanation of equation 6.5 see subsection 3.3.2. Due to inelastic scattering E_F can be different from E_S of the same electron and likewise θ_F can be different from θ_S due to elastic and inelastic scattering processes. A transmission through the spectrometer is only possible for $\theta_F < \theta_{tr} \wedge \theta_F < \theta_{max}$, with $\theta_{max} \approx 51^\circ$, the maximum transmission angle for the spectrometer. The transmission probability $T(E_S, q\Delta U)$ for the response function at a given retardation potential is the fraction of electrons which are transmitted through the main spectrometer according to equation 6.5 in relation to the number of started electrons.

The number of retardation potentials has been varied for figures 6.3 to 6.5. This is a compromise between having enough points to model the shape of the response function and few enough points to have lower individual uncertainties. Especially for the plateau region fewer points have been used, as the response function is flat in this region. This approach is applicable as long as only the approximate shape of the response function is of interest. However, future analyses like the deconvolution of the energy loss function (see subsection 3.3.6) will have to put more emphasis on the sampling concept. Previous work [Kra11] recommends a step size of 0.1 eV which would have resulted in a significantly longer computation time for the work at hand. The detailed KASSIOPEIA-configuration in use can be found in appendix B.

For the statistical uncertainty on the simulated events a calculation based on [Ull07] has been used. For a total number of n simulated events the statistical uncertainty on k detected events is

$$\delta k = \sqrt{\frac{(k+1) \cdot (k+2)}{(n+2) \cdot (n+3)} - \frac{(k+1)^2}{(n+2)^2}}. \quad (6.6)$$

The authors show that for Monte Carlo simulations this uncertainty yields more realistic results than the widely used Poissonian and Binomial error. Again, this statistical uncertainty purely arises from the Monte Carlo simulations and can be reduced by increasing the number of simulated electrons. Therefore, it is denoted with a δ . For a complete explanation of the concept of labeling uncertainties in the work at hand see the second paragraph of section 5.2.

6.2.3. Simulation Results

The results of simulations with setups 1 to 11 are depicted in figures 6.3 to 6.5.

The variation of the column density (setups 1 to 5) shown in figure 6.3 influences the height of the overall response function. This is due to the fact that higher column densities ρd increase the effective column density $\lambda(z, \theta)$. For a homogeneous density the effective column density according to equation 3.24 becomes

$$\lambda(z, \theta) = \frac{1}{\cos \theta} \int_0^d \rho(z') dz' = \frac{\rho d}{\cos \theta} = \lambda(\theta). \quad (6.7)$$

As a consequence scattering probabilities according to equation 3.23 increase for higher column densities ρd :

$$P_i(\theta) = \frac{(\lambda(\theta) \cdot \sigma_{\text{inel}})^i}{i!} e^{-\lambda(\theta) \cdot \sigma_{\text{inel}}}. \quad (6.8)$$

Therefore, more electrons scatter, lose energy and are overall less likely to pass the retardation potential. This leads to a decrease in the plateau height of the electron gun response function. Equation 6.8 shows that doubling the column density has the same effect as doubling the path length L in equation 3.24 for an isotropic source. Therefore, it is not surprising that for setup 3 at half the standard column density transmission probabilities for the electron gun are similar to the transmission probabilities for an isotropic source (see figure 3.6). For the latter only half the distance through the WGTS has to be passed on average.

Figure 6.4 shows the influence of varying electron gun angles (setups 1 and 6 to 9). Again, this influences the overall height of the response function of the electron gun since higher angles increase the effective column density according to equation 6.7. Consequently, scattering probabilities according to equation 6.8 increase as well. Despite constant step sizes in the electron starting angle θ_S the distances between the simulated response functions are not constant. This is due to the factor $\frac{1}{\cos \theta}$ in the effective column density and therefore in the scattering probabilities (see equation 6.8). As long as starting angles are low, their influence is weaker than a varying column density. For the maximum starting angle of 51.20° most electrons fail to pass the magnetic mirror, i. e. their polar angle at the end of the WGTS θ_F is higher than $\theta_{\text{max}} \approx 51^\circ$ (see equation 3.11). Accordingly very few electrons are transmitted for setup 9.

Finally, figure 6.5 depicts the influence of different assumed values of the energy spread of the electron gun beam which increases for higher electron gun rates (see subsection 3.3.5). The influence of the energy spread of the electron gun beam on the shape of the response function is rather small and the functions can be barely distinguished visually. This is due to the fact that the mean values of the electron

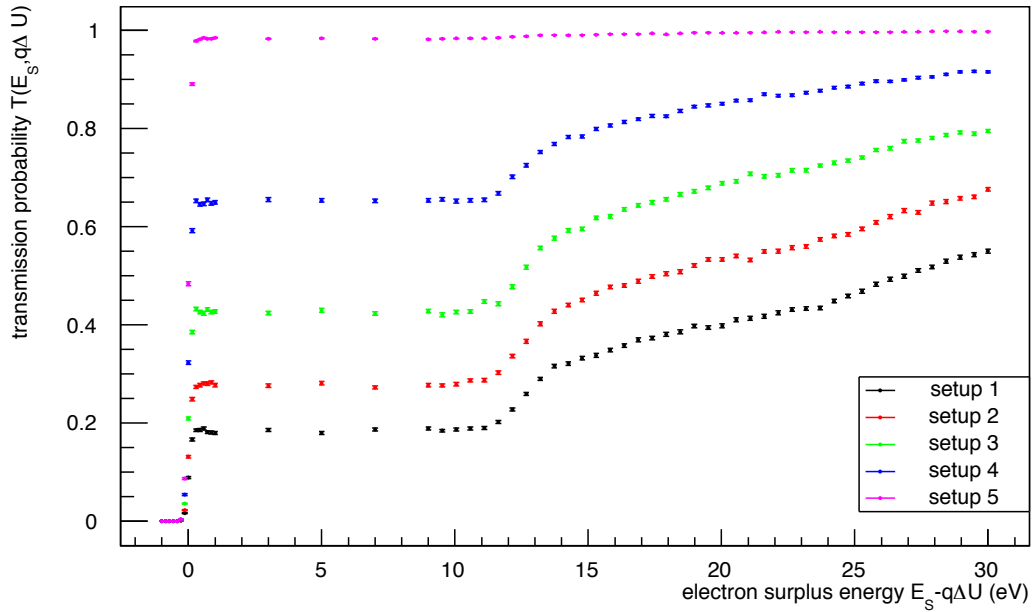


Figure 6.3.: **Simulated electron gun response functions for various column densities.** For this plot, electron gun beams have been simulated at various column densities in the WGTS. From bottom to top these are $\rho d = 5 \cdot 10^{17} \text{ cm}^{-2}$ (setup 1, black), $\rho d = 3.75 \cdot 10^{17} \text{ cm}^{-2}$ (setup 2, red), $\rho d = 2.5 \cdot 10^{17} \text{ cm}^{-2}$ (setup 3, green), $\rho d = 1.25 \cdot 10^{17} \text{ cm}^{-2}$ (setup 4, blue) and $\rho d = 0.05 \cdot 10^{17} \text{ cm}^{-2}$ (setup 5, pink). Other parameters have been set to standard values. For the electron gun this is $\theta_S = (1.12 \pm 0.46)^\circ$ and $E = (18600 \pm 0.107) \text{ eV}$.

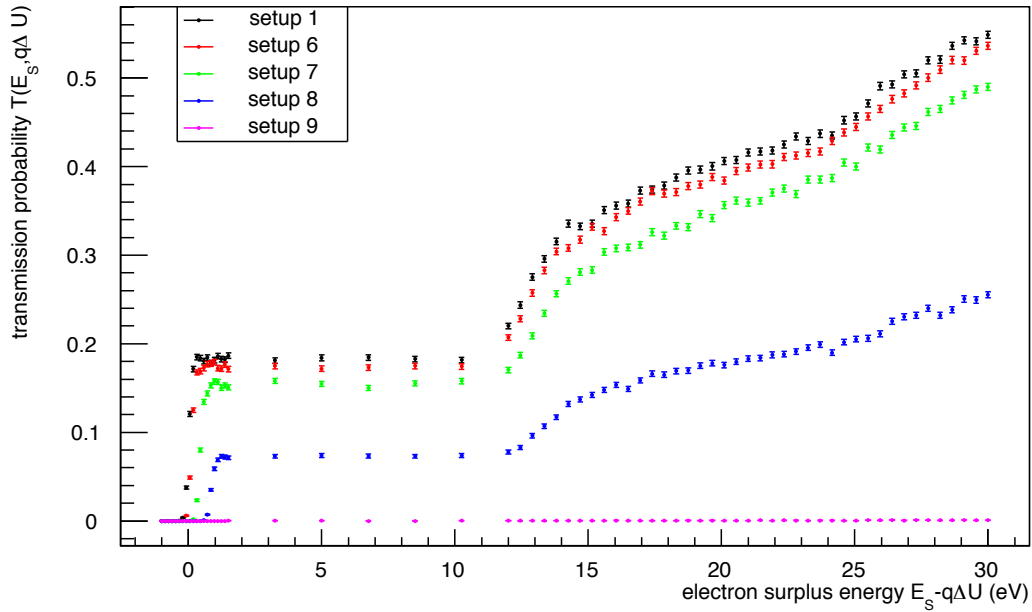


Figure 6.4.: **Simulated electron gun response functions for various electron gun angles.** For this plot, electron gun beams have been simulated at various starting angles. From top to bottom these are $\theta_S = (1.12 \pm 0.46)^\circ$ (setup 1, black), $\theta_S = (7.76 \pm 0.64)^\circ$ (setup 6, red), $\theta_S = (15.28 \pm 0.82)^\circ$ (setup 7, green), $\theta_S = (22.31 \pm 0.95)^\circ$ (setup 8, blue) and $\theta_S = (29.08 \pm 0.98)^\circ$ (setup 9, pink). Other parameters have been set to standard values. For the electron gun this is $E = (18600 \pm 0.107)$ eV and for the column density $\rho d = 5 \cdot 10^{17}$ cm $^{-2}$.

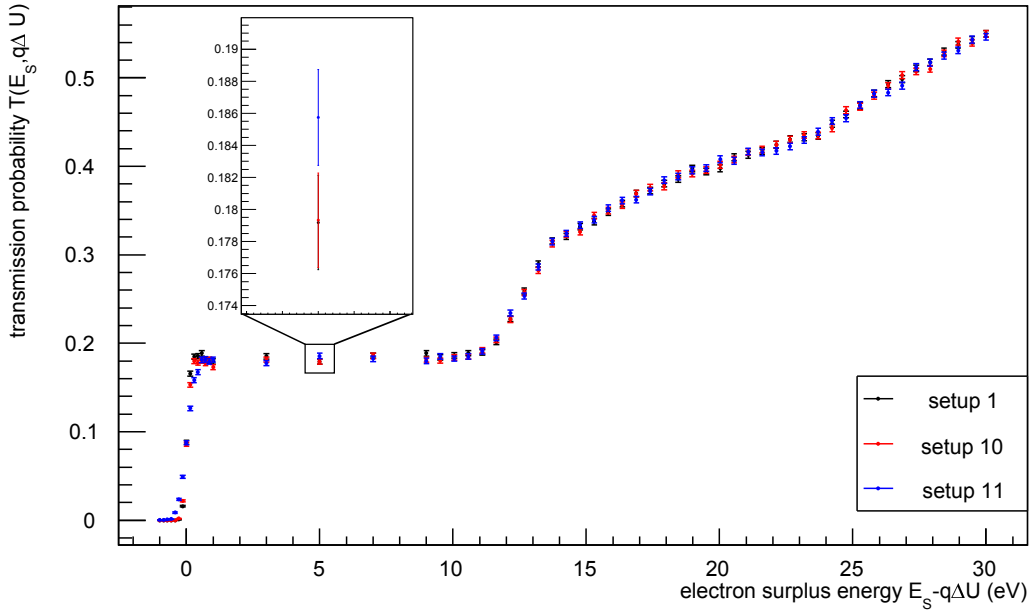


Figure 6.5.: **Simulated electron gun response functions for various spreads of the electron gun beam energy.** For this plot, electron gun beams have been simulated at various spreads of the beam energy. These are $E = (18600 \pm 0.107)$ eV (setup 1, black), $E = (18600 \pm 0.132)$ eV (setup 10, red) and $E = (18600 \pm 0.256)$ eV (setup 11, blue). Other parameters have been set to standard values. For the electron gun this is $\theta_S = (1.12 \pm 0.46)^\circ$ and for the column density $\rho d = 5 \cdot 10^{17} \text{ cm}^{-2}$.

beam energy do not change and the increased energy spread will only result in an additional smearing of the response function. If the plateaus of the response functions were identical, the influence of the energy uncertainty would be negligible and higher electron gun rates could be used. However, the inlay shows that a statistically reliable statement on whether the plateaus are identical is not possible based on the simulated amount of electrons. To further analyze this effect more simulated electrons are necessary.

6.3. Deriving the Total Inelastic Cross Section

As seen in the previous section, the plateau height of the electron gun response function is governed by the effective column density traversed by an electron in the WGTS and by the total inelastic cross section. This is due to the fact that the plateau represents the probability P_0 of an electron not to undergo any inelastic scattering which according to equation 6.8 is

$$P_0 = e^{-\lambda(\theta) \cdot \sigma_{\text{inel}}} = e^{-\frac{\rho d \cdot \sigma_{\text{inel}}}{\cos \theta}} . \quad (6.9)$$

Consequently, if either the column density or the total inelastic cross section are known, the other parameter can be derived from the plateau height of the electron gun response function. Since the work at hand focuses on the total inelastic cross section it will assume the column density to be known and stable. However, the

importance of this interplay between the two factors must not be underestimated: Once the total inelastic cross section has been measured, the same process can be used to repeatedly monitor the column density in the WGTS.

Nevertheless, the plateau of the electron gun response function has to be known to a sufficient degree of statistical and systematic uncertainty. In the simulations for the work at hand, systematic uncertainties of the electron gun to be considered are the angular spread of the electron gun and the spread on the electron beam energy. Statistical uncertainties can be reduced by longer measuring times of the electron gun. However, the measuring time allocated to the calibration program with the electron gun comes at cost of the run time to be spent on the neutrino mass measurement itself. Therefore, electron gun beam measurements should be as long as necessary but as short as possible. The necessary duration of a measurement is governed by the time to measure a plateau level sufficiently well to infer a total inelastic cross section with a precision of 0.2% as demanded in chapter 5. For the simulation of such measurements this means that a plateau simulated with a mean value for the total inelastic cross section has to be clearly distinguishable from another plateau simulated with a total inelastic cross section value deviating by 0.2%.

This measurement is demonstrated through a Monte Carlo simulation: it is reasonable to assume that the overall shape of the electron gun response function is known sufficiently well from previous electron gun measurements in order to know the plateau position along the energy axis. In the course of the simulations for this chapter, an electron surplus energy of 5 eV has always been part of the plateau range. Therefore, this point is arbitrarily chosen as a plateau testing point. For this purpose, the electrons which have been simulated for various retarding potentials in the previous section are now analyzed for an electron surplus energy of 5 eV only. Furthermore, the approximately 10^6 electrons have been divided into 10 samples of 10^5 electrons to simulate 10 individual measurements. Finally, an average on 10 transmission probabilities for the individual simulated measurements is calculated and an error band included. This is illustrated in figure 6.6 where two different inelastic cross sections have been assumed for two simulated measurement series. Only if the error bands can be distinguished, the two assumed total inelastic cross sections can be inferred from the plateau positions. In figure 6.6, the total inelastic cross section can be inferred with a precision of 0.2% at more than 1σ confidence.

In the following, an analytic estimation is given on how many electrons have to be emitted by the electron gun n_{required} to be able to distinguish the plateaus at 68.3% C.L. (1σ), 98.7% C.L. (3σ) and 99.9% C.L. (5σ). This number will be converted into a duration of the electron gun calibration measurement via the electron gun rate.

The transmission probabilities at plateau level for various inelastic scattering cross sections $p_{\sigma_{\text{inel}}}$ are given by equation 6.9. This means that the number of transmitted electrons $k_{\text{required},\sigma_{\text{inel}}}$ is

$$k_{\text{required},\sigma_{\text{inel}}} = n_{\text{required}} \cdot p_{\sigma_{\text{inel}}} \cdot \quad (6.10)$$

Using the uncertainty relation according to [Ull07] (equation 6.6) yields an uncer-

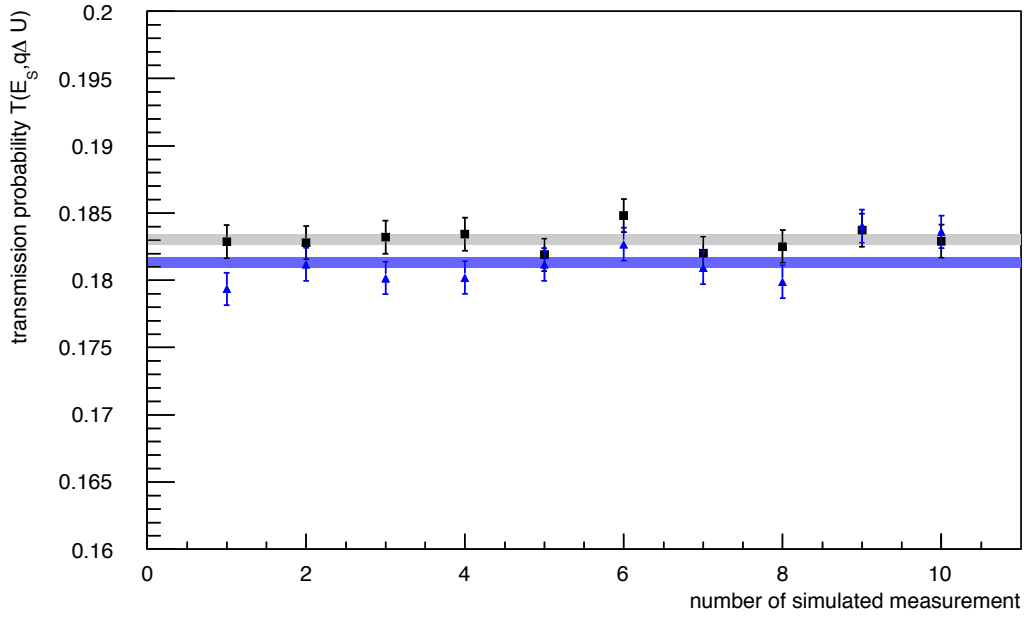


Figure 6.6.: **Simulation of 10 plateau measurements for two assumed total inelastic cross sections.** The diagram depicts 10 simulated measurements of the plateau level of the electron gun response function for setup 1 and $\sigma_{\text{inel}} = 3.4000 \cdot 10^{-18} \text{cm}^2$ (black squares)/ $\sigma_{\text{inel}} = 3.4068 \cdot 10^{-18} \text{cm}^2$ (blue triangles). This is a deviation in the total inelastic cross section of 0.2%. The gray (blue) band at the top (bottom) shows the 1σ error ribbon for an average over measurements for $\sigma_{\text{inel}} = 3.4000 \cdot 10^{-18} \text{cm}^2$ ($\sigma_{\text{inel}} = 3.4068 \cdot 10^{-18} \text{cm}^2$).

Table 6.3.: **Estimation of electron gun electrons required to determine the total inelastic cross section.** This table summarizes estimations on how many emitted electrons are necessary to determine the total inelastic cross section at a precision of 0.2% at various confidence levels (1σ , 3σ , 5σ) for different electron gun setups.

Setup (no.)	Simulation Settings			Required Particles n_{required} for		
	ρd (10^{17} cm^{-2})	θ_S at 1.4 T ($^\circ$)	E (eV)	68.3% C.L. (10^6)	98.7% C.L. (10^6)	99.9% C.L. (10^6)
1	5.00	1.12	18600	1.56	13.97	38.79
2	3.75	1.12	18600	1.59	14.31	39.73
3	2.50	1.12	18600	1.86	16.71	46.42
4	1.25	1.12	18600	2.94	26.42	73.37
5	0.05	1.12	18600	59.38	> 100	> 100
6	5.00	7.76	18600	1.56	14.00	38.88
7	5.00	15.28	18600	1.58	14.17	39.35
8	5.00	22.31	18600	1.65	14.79	41.07
9	5.00	29.08	18600	1.92	17.26	47.95

tainty of

$$(\delta k)_{\text{required}, \sigma_{\text{inel}}} = \sqrt{\frac{(n_{\text{required}} \cdot p_{\sigma_{\text{inel}}} + 1) \cdot (n_{\text{required}} \cdot p_{\sigma_{\text{inel}}} + 2)}{(n_{\text{required}} + 2) \cdot (n_{\text{required}} + 3)} - \frac{(n_{\text{required}} \cdot p_{\sigma_{\text{inel}}} + 1)^2}{(n_{\text{required}} + 2)^2}} \quad (6.11)$$

at 1σ confidence. For setups 1 to 9 the required number of electrons at different confidence levels has been calculated and summarized in table 6.3⁴.

In table 6.3 it becomes clear that setups 4, 5 and 9 require considerably more electrons emitted by the electron gun than other setups, especially at higher confidence levels. Therefore, these setups are not favorable for a determination of the total inelastic cross section. For setups 4 and 5 the column density is so low that scattering barely occurs (compare figure 6.3). To obtain a sufficient amount of unscattered electrons at the detector, more electrons have to be emitted by the electron gun. Setup 9 is unfavorable as too many electrons are reflected at the spectrometer because their polar angle exceeds the maximum angle θ_{max} (compare figure 6.4). The lowest number of electron gun electrons is required for setups 1, 2, 6 and 7. Therefore, these setups are most favorable for a determination of the total inelastic cross section.

As shown in subsection 3.3.5 the rate of the electron gun is directly related to the spread in beam energy. The rate of emitted electrons can be increased (respectively decreased) at the cost (respectively gain) of beam energy precision. If the plateaus for various energy beam spreads were identical, the electron gun could be used at the highest rate to determine the total inelastic cross section. However, analyses performed for figure 6.5 show that more simulations are required to verify

⁴Setups 10 and 11 have only been used to analyze the energy spread of the electron gun beam. They are therefore not considered in table 6.3.

this. Therefore, to convert the number of simulated electrons into a measurement time the rate of 69 kcps for an energy spread of $\sigma_E = 132$ meV is used which fulfills the design requirements for the electron gun [Bab13]. For 68.3% C.L. (1σ) approximately $2 \cdot 10^6$ electrons from the electron gun are required for the recommended electron gun setups. This means that if a calibration measurement with the electron gun is supposed to infer the total inelastic cross section at a precision of 0.2% at 68.3% C.L. (1σ) the measurement takes approximately 30 seconds at an electron gun rate of 69 kcps. However, preliminary simulations have illustrated that this confidence level is not sufficient to determine the plateau levels reliably. For 98.7% C.L. (3σ) approximately $14 \cdot 10^6$ electrons are required which corresponds to a measurement time of approximately 3:20 minutes. Finally, 99.9% C.L. (5σ) requires approximately $39 \cdot 10^6$ electrons and a measurement time of about 9:30 minutes.

6.4. Conclusion and Outlook

In this chapter, the response function of the Rearsection electron gun has been simulated using the Monte Carlo particle tracking of KASSIOPEIA. It has been shown how different settings for the column density in the WGTS, the angle of the electron gun and the energy spread of the electron gun influence the shape of the electron gun response function (see figures 6.3 to 6.5). For small electron gun angles, the influence of an angular change is smaller than for changes in the column density. This is in accordance with the analytic model. The influence of the electron beam spread on the plateau height has been analyzed but simulations with more electrons are necessary to draw reliable conclusions.

To estimate the electron gun measuring time required for a determination of the total inelastic cross section the column density has been assumed to be known and stable. Furthermore, the rate of the electron gun has been assumed to be 69 kcps. In this case, the total inelastic cross section can be inferred from a measurement of the plateau level of the response function. Most favorable for this procedure are four specific electron gun setups (1, 2, 6 and 7 in table 6.2). For any of these setups the required measurement time for a determination of the total inelastic cross section with a precision of 0.2% at 68.3% C.L. (1σ) is about 30 seconds. This result is very similar to the estimation of the design report for a determination of the product of column density and total inelastic cross section. For this determination, the measuring time was estimated to be at least 25 seconds. Nevertheless, the column density is subject to fluctuations and has to be monitored repeatedly. The determination of the total inelastic cross section is a one-time calibration measurement since the total inelastic cross section is a physics parameter which is not subject to temporal variation. For this reason, the work at hand recommends to invest more measuring time on its determination to achieve an optimal degree of precision.

To verify the analytic estimations on required measuring times, Monte Carlo simulations with more electrons should be performed to emulate these measurements. Furthermore, a promising approach to reduce all measurement times is to further investigate the behavior of the electron gun at higher rates. Higher rates lead to a wider spread of the electron beam energy. If this spread does not significantly influence the plateau level of the electron gun response function, higher rates could be used and measuring times considerably reduced.

7. Conclusion and Outlook

The work at hand has been composed in the scope of the KATRIN experiment at the Karlsruhe Institute of Technology. It is the goal of KATRIN to improve the neutrino mass sensitivity of the direct measurement method by one order of magnitude to 0.2 eV at 90 % C.L.. Since the measured parameter at β -decay experiments such as KATRIN is the squared neutrino mass, uncertainties on the measured value even have to be reduced by two orders of magnitude. An important source of systematic uncertainties at the KATRIN experiment is the tritium source (WGTS) where electrons may scatter off gaseous tritium and lose energy. Any unaccounted for energy loss of the signal electrons will cause a systematic uncertainty on the determination of the neutrino mass. Besides the column density of tritium gas, the most important parameter to determine energy loss is the total inelastic scattering cross section σ_{inel} . In the course of this thesis the systematic influence of the total inelastic scattering cross section has been analyzed in two steps: first, the requirements on the precision of this parameter have been determined. Second, the calibration program to measure the total inelastic scattering cross section with an electron gun has been simulated.

Currently, the total inelastic scattering cross section used for the analytic model of the KATRIN experiment is $\sigma_{\text{inel}} = (3.40 \pm 0.07) \cdot 10^{-18} \text{ cm}^2$ [Ase00]. This precision of approximately 2 % is known not to be sufficient to meet the requirements of the KATRIN technical design report, since it induces a too large systematic shift on the squared neutrino mass Δm_ν^2 . For this thesis, an acceptable shift induced by the total inelastic scattering cross section has been estimated to be $\sigma_{\text{sys,max},\sigma_{\text{inel}}} \approx 2.3 \cdot 10^{-3} \text{ eV}^2$. While not considering any other systematic effects, it has been found that in order not to exceed the acceptable systematic shift, the total inelastic scattering cross section has to be determined with a precision of 0.2 % for an analysis interval of $[-30 \text{ eV}, +5 \text{ eV}]$ around the tritium endpoint. Since this is a quite ambitious degree of precision it has been analyzed whether the usage of analysis intervals with different lower boundaries can somewhat ease this requirement at the cost of statistical uncertainty. If the total inelastic scattering cross section is known to a lower degree of precision than 0.2 %, it is advisable to use analysis intervals with a lower boundary higher than -30 eV . For given lower degrees of precision on the total inelastic scattering cross section and when other systematic effects are neglected the

Table 7.1.: **Recommended lower boundaries of the analysis interval in case of different uncertainties on σ_{inel} .** This table summarizes the findings on which lower boundaries of analysis intervals should be considered in case of various outcomes for a measurement of the total inelastic cross section.

Relative uncertainty on σ_{inel} in a future electron gun measurement	Recommended lower boundary of the analysis interval for a neutrino mass measurement (eV)
0.3 %	-30
0.6 %	-26
0.9 %	-23, -24, -25
1.2 %	-22, -23
1.5 %	-22, -23
1.8 %	-21, -22
2 %	-20, -21, -22

recommended intervals yield a lower combined uncertainty compared to the standard analysis interval of $[-30 \text{ eV}, +5 \text{ eV}]$. Recommended intervals for various degrees of precision on the total inelastic scattering cross section are summarized in table 7.1.

To investigate the influence of up to date electron gun characteristics on the response function of the KATRIN experiment, calibration measurements with the Rearsetion electron gun have been simulated using KASSIOPEIA. These simulations have been performed with various setups for the column density, the electron gun polar angle and the energy spread of the electron beam. The shape of these response functions is summarized in figures 6.3 to 6.5. For a determination of the column density, the total inelastic scattering cross section in the WGTS was assumed to be known and stable. Furthermore, the electron gun rate was assumed to be 69 kcps based on a analysis of data provided by [Mon15]. The work at hand has identified four specific electron gun setups (1, 2, 6 and 7 in table 6.2) to be most favorable for a determination of the total inelastic scattering cross section. Depending on the required confidence level of such a calibration measurement different measuring times have been estimated in order to achieve a precision of 0.2% on the total inelastic scattering cross section. For a determination at 98.7% C.L. (3σ) a measuring time of 3:20 minutes at the plateau position of the electron gun response function is required. This result is compatible with the KATRIN technical design report [KC05] which estimated a measuring time of at least 25 seconds for a determination of the product of column density and total inelastic scattering cross section at 1σ . Nevertheless, the determination of the total inelastic scattering cross section is a one-time calibration measurement. Therefore, it seems reasonable to spend more measuring time on its determination in order to achieve an optimal degree of precision.

The work at hand recommends two major tasks for further research: First, more systematic effects should be analyzed in the same manner as the total inelastic scattering cross section in the work at hand This would not only allow for an updated overview on the current state of the influence of known systematic effects but also improve the understanding of their correlation with the choice of the β -spectrum

analysis interval. Second, the influence of the electron gun energy spread on the determination procedure of the total inelastic scattering cross section should be further investigated. If it turns out to be negligible, measuring times could be considerably reduced by operating the electron gun at higher rates.

8. German Summary

8.1. Einleitung

Diese Zusammenfassung in deutscher Sprache ist gemäß den Kapiteln des Hauptteils dieser Arbeit gegliedert und verzichtet auf die Nennung von Literaturverweisen, die dort bereits angeführt werden. Die Unterkapitel der Zusammenfassung heben die wichtigsten Punkte aus dem Hauptteil hervor.

Das KATRIN Experiment ist ein Neutrinomassenexperiment der nächsten Generation. Es hat sich das Ziel gesetzt, durch eine Analyse des Tritium- β -Spektrums die Sensitivität direkter Neutrinomassenbestimmungen auf

$$m_{\nu_e} < 0.2 \text{ eV (90 \% C. L.)} \quad (8.1)$$

zu erhöhen. Das ist eine Verbesserung um eine Größenordnung gegenüber den Vorgängerexperimenten in Mainz und Troitsk. Auf Grund des bei KATRIN und den Vorgängerexperimenten angewandten Messprinzips erfordert dies im Hinblick auf die zu messende Größe m_ν^2 sogar eine Verbesserung um zwei Größenordnungen. Das bedeutet, dass verbleibende systematische Unsicherheiten sehr klein und zudem äußerst genau bekannt sein müssen.

Eine der komplexesten Bereiche des KATRIN Experiments im Hinblick auf systematische Unsicherheiten ist die Tritiumquelle (WGTS), die Tritium in Gasform enthält. Die hier emittierten Signalelektronen können am Tritium streuen und dadurch Energie verlieren. Jeder nicht genau bekannte Energieverlust ruft eine systematische Unsicherheit auf die Bestimmung der Neutrinomasse hervor. Neben der Säulendichte des Tritiums in der Quelle ist der totale inelastische Streuquerschnitt von Elektronen an Tritium der wichtigste Einflussfaktor auf Streuprozesse. Derzeit ist der Wert des totalen inelastischen Streuquerschnitts nur bis auf 2% bekannt, was für die Anforderungen an die Sensitivität von KATRIN nicht ausreichend ist.

Der Analyseteil der vorliegenden Arbeit ist deshalb in zwei Teile gegliedert: Zunächst wird untersucht, wie genau der totale inelastische Streuquerschnitt bekannt sein muss, um die Anforderungen des technischen Design Reports von KATRIN an systematische Unsicherheiten zu erfüllen. Im Anschluss wird das zur Bestimmung des totalen inelastischen Wirkungsquerschnitts vorgesehene Messverfahren simuliert.

Der Hauptteil dieser Arbeit bietet zunächst einen Überblick zur Neutrinophysik, wobei ein Schwerpunkt auf Themen von besonderem Interesse für das KATRIN Experiment liegt. Dies schließt auch eine Vorstellung weiterer Neutrinomassenexperimente ein (s. Kapitel 2). Im Weiteren wird das KATRIN Experiment selbst vorgestellt. Dabei wird zunächst das Messprinzip erläutert, bevor die Dimensionen des experimentellen Aufbaus und darüber hinaus die analytischen Grundlagen für die Neutrinomassenbestimmung vorgestellt werden (s. Kapitel 3). Das Schätzverfahren für die Neutrinomasse ist unter anderem Inhalt von Kapitel 4. Weiterhin wird dort die KASPER Softwareumgebung vorgestellt, mit der sämtliche Analysen für diese Arbeit durchgeführt wurden. Erweiterungen, die im Rahmen der vorliegenden Arbeit ergänzt wurden, werden dort ebenfalls erläutert. Im darauf folgenden Kapitel 5 wird untersucht, welchen Einfluss der totale inelastische Streuquerschnitt auf die systematische Unsicherheit der Neutrinomassenbestimmung hat. Hieraus wird eine minimale Präzision abgeleitet, mit der der totale inelastische Streuquerschnitt bestimmt werden sollte. Für eine solche Bestimmung verwendet KATRIN eine Elektronenkanone, die einen wohldefinierten Elektronenstrahl in die Tritiumquelle emittiert. Diese Kalibrationsmessung mit der Elektronenkanone zur Bestimmung des totalen inelastischen Streuquerschnitts wird in Kapitel 6 simuliert. Aufbauend hierauf werden Empfehlungen für die Einstellungen der Elektronenkanone gegeben und es wird geschätzt, wie lange eine Kalibrationsmessung zur Bestimmung des totalen inelastischen Streuquerschnitts dauern sollte. Kapitel 7 fasst Ergebnisse zusammen und gibt einen Ausblick zum Ausbau der gewonnenen Erkenntnisse.

8.2. Neutrinophysik

Seinen Anfang nahm das weite Feld der Neutrinophysik 1930 mit der Postulierung des Neutrinos durch W. Pauli. Bis heute wurden drei Neutrinoarten (Neutrino-Flavors) nachgewiesen und es gibt starke experimentelle Hinweise darauf, dass sich diese durch Neutrinooszillation ineinander umwandeln können. Dieser Prozess setzt eine Unterscheidung von sogenannten Neutrino-Masseneigenzuständen und Flavor-Eigenzuständen voraus, sowie dass zwei der drei Masseneigenwerte von null verschieden sind. Dies geht über das Standardmodell der Teilchenphysik hinaus, in dem Neutrinos als masselos angenommen werden.

Bei der Suche nach der Neutrinomasse werden verschiedene Ansätze verfolgt. Modellabhängige Methoden, wie die Suche nach dem neutrinolosen Doppel-Betazerfall, setzen voraus, dass das Neutrino ein Majorana- und kein Dirac-Teilchen ist. Derzeit geht das Standardmodell von einem Dirac-Teilchen aus. Kosmologische Modelle können durch das Einbeziehen der Neutrinomasse in ihre Multiparametermodelle obere Limits auf die Summe der Masse leichter Neutrinos setzen. Allerdings sind solche Limits stark abhängig vom angewandten Modell und der Art der genutzten Daten. KATRIN gehört zu den Modell-unabhängigen und direkten Neutrinomassenexperimenten. Das bedeutet, dass das genutzte Prinzip sowohl auf Majorana- als auch auf Dirac-Neutrinos anwendbar ist. “Direkt” bedeutet in diesem Zusammenhang, dass das dem KATRIN Experiment zu Grunde liegende Messprinzip auf rein kinematischen Zusammenhängen beruht.

8.3. Das KARlsruher TRitium Neutrino (KATRIN) Experiment

Ziel des KATRIN Experiments ist die Verbesserung der Sensitivität direkter Neutrinomassenbestimmungen um eine Größenordnung im Vergleich zu vorangegangenen Experimenten auf

$$m_{\nu_e} < 0.2 \text{ eV (90 \% C. L.)} . \quad (8.2)$$

Die direkte und Modell-unabhängige Neutrinomassenbestimmung beim KATRIN Experiment basiert auf einer genauen Analyse des Elektronenspektrums beim β -Zerfall von Tritium. Bei KATRIN ist hierzu die Tritiumquelle (WGTS) vom Detektor getrennt, so dass als Spektrometer ein sogenannter MAC-E Filter genutzt werden kann. Dieser bietet eine einzigartige Energieauflösung im Vergleich zu anderen Spektroskopieansätzen bei der Bestimmung der Neutrinomasse.

Eine spektroskopische Bestimmung der Neutrinomasse ist möglich, da das Spektrum nahe der Endpunktsenergie von Tritium unterschiedliche Formen für den Fall einer verschwindenden und für den Fall einer nicht verschwindenden Neutrinomasse annimmt. Hierzu wird ein analytisches Modell an experimentelle Daten gefittet, was schließlich, bedingt durch die Kinematik des β -Zerfalls, das Quadrat der Neutrinomasse liefert. Diese Eigenheit erfordert, dass die Sensitivität für die Messgröße beim KATRIN Experiment sogar um zwei Größenordnungen verbessert werden muss.

Grundlegende Elemente des analytischen Modells für KATRIN sind die Transmissionsfunktion und die Energieverlustfunktion. Die Transmissionsfunktion beschreibt, ob isotrop emittierte Elektronen mit gegebener Energie und beschränktem Maximalwinkel zum Magnetfeld in der WGTS das Spektrometer passieren können. Die Energieverlustfunktion beschreibt, wie wahrscheinlich ein bestimmter Energieverlust durch inelastische Streuung für ein Elektron in der Quelle ist. Dieser Prozess wird maßgeblich durch die Säulendichte des Tritiumgases in der Quelle und durch den totalen inelastischen Streuquerschnitt bestimmt. Die Antwortfunktion fasst schließlich beide Funktionen zusammen und repräsentiert somit alle experimentellen Einflüsse auf das β -Spektrum.

8.4. Die KASPER Softwareumgebung

Die KASPER Softwareumgebung liefert große Teile der Software, die für die Vorbereitung und Analyse des KATRIN Experiments erforderlich sind. Dies beinhaltet die analytische Beschreibung von Vorgängen in der Tritiumquelle (SSC), statistische Analysetools (KAFIT) sowie Monte Carlo Bahnverfolgungsrechnungen (KASSIOPEIA). Die Beschreibung der Quelle durch SSC wird im Rahmen dieser Arbeit erweitert. KAFIT wird für die Durchführung von Ensemblesimulationen in Kapitel 5 verwendet, um die systematischen Einflüsse des totalen inelastischen Streuquerschnitts zu untersuchen. Hierbei wird eine theoretische Zählrate am Detektor berechnet und an eine simulierte experimentelle Rate gefittet, um die quadratische Neutrinomasse zu erhalten. Wenn dieser Prozess mehrfach wiederholt wird (in der Größenordnung 10^5), kann der Einfluss eines systematischen Effekts ermittelt werden. KASSIOPEIA wird in Kapitel 6 zur Simulation von Kalibrationsmessungen mit der Elektronenkanone genutzt.

Table 8.1.: **Empfohlene untere Grenzen für das Analyseintervall im Tritiumspektrum im Falle verschiedener Unsicherheiten auf den totalen inelastischen Streuquerschnitt.** Diese Tabelle fasst zusammen, welche Untergrenzen für ein Analyseintervall verwendet werden sollten, für den Fall dass der totale inelastische Streuquerschnitt nach der Messung mit verschieden großen Unsicherheiten behaftet ist.

Relative Unsicherheit auf σ_{inel} in einer zukünftigen Messung mit der Elektronenkanone	Empfohlene Untergrenze für das Analyseintervall bei einer Neutrinomassenbestimmung (eV)
0.3 %	−30
0.6 %	−26
0.9 %	−23, −24, −25
1.2 %	−22, −23
1.5 %	−22, −23
1.8 %	−21, −22
2 %	−20, −21, −22

8.5. Systematische Effekte von Streuung in der WGTS

Im Hinblick auf systematische Effekte ist die WGTS eines der komplexesten Elemente des KATRIN Experiments. Von Tritium emittierte Elektronen streuen hier inelastisch an weiteren Tritium-Molekülen und verlieren Energie. Der neben der Säulendichte von Tritium wichtigste Parameter dieses Prozesses ist der inelastische Streuquerschnitt, wobei sich diese Arbeit auf dessen integrierte Form, den totalen inelastischen Streuquerschnitt fokussiert. Aus Messungen bei vorangegangenen Experimenten ist dieser lediglich mit einer Präzision von 2 % bekannt. Dies ruft eine systematische Unsicherheit auf die quadratische Neutrinomasse hervor, die die Limits des technischen Designreports für KATRIN übersteigt. Im Rahmen dieser Arbeit wird eine durch den totalen inelastischen Streuquerschnitt hervorgerufenen Unsicherheit von $\sigma_{\text{sys,max},\sigma_{\text{inel}}} \approx 2.3 \cdot 10^{-3} \text{ eV}^2$ als akzeptabel angesehen. Es wird gezeigt, dass der totale inelastische Streuquerschnitt bis auf 0.2 % genau bekannt sein muss, um die geforderte Unsicherheit auf die Neutrinomasse nicht zu übersteigen. Weitere systematische Effekte werden hierbei vernachlässigt.

Diese Forderung gilt für ein Analyseintervall des β -Spektrums von $[-30 \text{ eV}, +5 \text{ eV}]$ um den Spektrumsendpunkt. Dies ist das vom technischen Designreport angenommene Standardanalyseintervall. Es wird gezeigt, dass eine Verkürzung der Intervalllänge dazu führt, dass die systematische Unsicherheit, die durch den totalen inelastischen Wirkungsquerschnitt hervorgerufen wird, abnimmt. Allerdings geschieht dies auf Kosten der statistischen Unsicherheit, die zunimmt. Die im Rahmen dieser Arbeit durchgeführten Analysen haben gezeigt, dass es von der Präzision abhängt, mit der der totale inelastische Streuquerschnitt bekannt ist, welches Analyseintervall die geringste kombinierte Unsicherheit aufweist. Die entsprechenden Empfehlungen für Analyseintervalle sind in Tabelle 8.1 zusammengefasst.

8.6. Simulation von Messungen mit der Elektronenkanone

Zur Bestimmung des totalen inelastischen Streuquerschnitts wird die Elektronenkanone verwendet. Diese emittiert einen wohldefinierten Elektronenstrahl in die WGTS, wobei die so emittierten Elektronen den selben elektromagnetischen Einflüssen und Streuprozessen unterliegen wie Elektronen, die isotrop und mit einem kontinuierlichen Spektrum von Tritium emittiert werden. Durch die Energiefilterung am Spektrometer kann für diese Elektronen, genau wie für die Elektronen aus dem Tritiumzerfall eine Antwortfunktion aufgenommen werden. Solche Antwortfunktionen sind für verschiedene Winkeleinstellungen und Energieunschärfen der Elektronenkanone, sowie für verschiedene Säulendichten simuliert worden und in den Abbildungen 6.3 bis 6.5 dargestellt. Es ist erkennbar, dass der Einfluss des Winkels für kleine Winkel geringer ist als der Einfluss der Säulendichte. Dies ist in Übereinstimmung mit den Erwartungen aus analytischen Formeln.

Für die Bestimmung des totalen inelastischen Streuquerschnitts genügt eine Messung der Transmissionswahrscheinlichkeit am Plateau der Antwortfunktion. Unter der Annahme, dass die Säulendichte bekannt und stabil ist und bei einer verwendeten Elektronenkanonerate von 69kcps kann die erforderliche Messzeit für die Bestimmung des totalen inelastischen Streuquerschnitts geschätzt werden. Hierfür wird eine Messung mit einem der Setups 1, 2, 6 oder 7 für die Elektronenkanone und Säulendichte empfohlen. Diese Setups sind in Tabelle 6.2 beschrieben. Bei einer solchen Kalibrationsmessung sollte gemäß Kapitel 5 eine Präzision von 0.2% erreicht werden. Um dies mit 68.3% C.L. (1σ) zu realisieren, sind etwa 30 Sekunden Messzeit erforderlich. Dieses Ergebnis steht in Übereinstimmung mit der Schätzung des technischen Design Reports für eine Messung des Produkts aus Säulendichte und totalem inelastischem Streuquerschnitt von 25 Sekunden. Für 98.7% C.L. (3σ) sind circa 3:20 Minuten und für 99.9% C.L. (5σ) etwa 9:30 Minuten Messzeit erforderlich. Da es sich bei der Bestimmung des totalen inelastischen Streuquerschnitts um eine einmalige Kalibrationsmessung handelt sollte für diesen wichtigen Parametern genug Messzeit aufgewandt werden, um höhere Konfidenzniveaus zu erreichen.

8.7. Ausblick

Zum Ausbau der Ergebnisse dieser Arbeit können vor allem zwei weiterführende Fragestellungen identifiziert werden. Zunächst sollten weitere systematische Einflüsse in der gleichen Weise untersucht werden, wie bei der Untersuchung des totalen inelastischen Streuquerschnitts in dieser Arbeit. Dies würde nicht nur eine aktualisierte Übersicht über den Einfluss bekannter Systematiken liefern, sondern auch das Verständnis für ihre Korrelation mit der Wahl des Analyseintervalls für das β -Spektrum verbessern. Zweitens sollte der Einfluss der Energiepräzision der Elektronenkanone auf die Bestimmung des totalen inelastischen Streuquerschnitts weiter untersucht werden. Falls dieser Einfluss vernachlässigbar ist, könnten die erforderlichen Messzeiten deutlich verkürzt werden, da die Elektronenkanone dann mit höheren Raten betrieben werden kann.

Bibliography

- [Aal04] C. Aalseth et al., *Neutrinoless double beta decay and direct searches for neutrino mass*, arXiv:hep-ph **0412300v1** (2004).
- [Abt04] I. Abt et al., *A New ^{76}Ge Double Beta Decay Experiment at LNGS*, arXiv:hep-ex **0404039v1** (2004).
- [AC12] ATLAS-Collaboration, *Observation of a new particle in the search for the Standard Model Higgs boson with the ATLAS detector at the LHC*, Physics Letters B **716**, 1 (2012) 1–29.
- [Ago13] M. Agostini et al., *Results on Neutrinoless Double- β Decay of ^{76}Ge from Phase I of the GERDA Experiment*, Physical Review Letters **111**, 12 (2013) 122503.
- [Aha13] B. Aharmim et al., *Combined analysis of all three phases of solar neutrino data from the Sudbury Neutrino Observatory*, Physical Review C **88**, 2 (2013) 025501.
- [Ahn14] C. P. Ahn et al., *The Tenth Data Release of the Sloan Digital Sky Survey: First Spectroscopic Data from the SDSS-III Apache Point Observatory Galactic Evolution Experiment*, The Astrophysical Journal Supplement Series **211**, 2 (2014) 17.
- [Alp15] B. Alpert et al., *HOLMES*, The European Physical Journal C **75**, 3 (2015) 112.
- [And11] E. Andreotti et al., *^{130}Te Neutrinoless Double-Beta Decay with CUORICINO*, Astroparticle Physics **34**, 11 (2011) 822–831.
- [Arn14] R. Arnold et al., *Search for Neutrinoless Double-Beta Decay of ^{100}Mo with the NEMO-3 Detector*, Physical Review D **89**, 11 (2014) 111101.
- [Arr80] G. Arrighini et al., *A study of the inelastic scattering of fast electrons from molecular hydrogen*, Molecular Physics **41**, 6 (1980) 1501–1514.
- [Ase00] V. Aseev et al., *Energy loss of 18 keV electrons in gaseous T_2 and quenched condensed D_2 films*, The European Physical Journal D **10**, 1 (2000) 39–52.
- [Ase11] V. N. Aseev et al., *Upper limit on the electron antineutrino mass from the Troitsk experiment*, Physical Review D **84**, 11 (2011) 112003.
- [Asn14] D. M. Asner et al., *Single electron detection and spectroscopy via relativistic cyclotron radiation*, arXiv **1408.5362v** (2014).
- [Bab13] M. Babutzka et al., *KATRIN Rearsection system specification document*, Internal Document (2013).

- [Bab14] M. Babutzka, *Design and development for the Rearsection of the KATRIN experiment*, Phd thesis, Karlsruhe Institute of Technology (2014).
- [Bah68] J. N. Bahcall et al., *Present Status of the Theoretical Predictions for the ^{36}Cl Solar-Neutrino Experiment*, Physical Review Letters **20**, 21 (1968) 1209–1212.
- [Bea80] G. Beamson et al., *The collimating and magnifying properties of a superconducting field photoelectron spectrometer*, Journal of Physics E: Scientific Instruments **13**, 1 (1980) 64–66.
- [Bel95] A. Belesev et al., *Results of the troitsk experiment on the search for the electron antineutrino rest mass in tritium beta-decay*, Physics Letters B **350**, 2 (1995) 263–272.
- [Bon01] J. Bonn et al., *The Mainz neutrino mass experiment*, Nuclear Physics B - Proceedings Supplements **91**, 1-3 (2001) 273–279.
- [Bor03] B. Bornschein et al., *Self-Charging of Quench Condensed Tritium Films*, Journal of Low Temperature Physics **131**, 1-2 (2003) 69–88.
- [Bor08] B. Bornschein, *Determination of Neutrino Mass from Tritium Beta Decay*, Fusion Science and Technology **54**, 1 (2008) 59–66.
- [CC12] CMS-Collaboration, *Observation of a new boson at a mass of 125 GeV with the CMS experiment at the LHC*, Physics Letters B **716**, 1 (2012) 30–61.
- [Cha14] J. Chadwick, *Intensitätsverteilung im magnetischen Spectrum der β -Strahlen von radium B + C*, Verhandlungen der Deutschen Physikalischen Gesellschaft **16** (1914) 383.
- [Che95] Z. Chen et al., *Calculation of the excitation cross sections for the $B^1\Sigma_u^+$ and $C^1\Pi_u^+$ states in $e - \text{H}_2$ scattering at 60 eV*, Physical Review A **51**, 5 (1995) 3745–3750.
- [Col05] S. Cole et al., *The 2dF Galaxy Redshift Survey: power-spectrum analysis of the final data set and cosmological implications*, Monthly Notices of the Royal Astronomical Society **362**, 2 (2005) 505–534.
- [Cow98] G. Cowan, *Statistical Data Analysis*, Oxford University Press, New York, first edition (1998).
- [Cro99] R. Croft et al., *Cosmological Limits on the Neutrino Mass from the Ly α Forest*, Physical Review Letters **83**, 6 (1999) 1092–1095.
- [Dan62] G. Danby et al., *Observation of high-energy neutrino reactions and the existence of two kinds of neutrinos*, Physical Review Letters **9**, 36 (1962) 36–44.
- [Dav94] R. Davis, *A review of the homestake solar neutrino experiment*, Progress in Particle and Nuclear Physics **32** (1994) 13–32.
- [De 82] A. De Rújula et al., *Calorimetric measurements of $^{163}\text{holmium}$ decay as tools to determine the electron neutrino mass*, Physics Letters B **118**, 4-6 (1982) 429–434.

- [Ein05] A. Einstein, *Über einen die Erzeugung und Verwandlung des Lichtes betreffenden heuristischen Gesichtspunkt*, Annalen der Physik **322**, 6 (1905) 132–148.
- [Ell27] C. D. Ellis et al., *The Average Energy of Disintegration of Radium E*, Proceedings of the Royal Society of London A **117**, 776 (1927).
- [Eng64] F. Englert et al., *Broken Symmetry and the Mass of Gauge Vector Mesons*, Physical Review Letters **13**, 9 (1964) 321–323.
- [EXO14] EXO-200 Collaboration, *Search for Majorana neutrinos with the first two years of EXO-200 data*, Nature **510**, 7504 (2014) 229–234.
- [Gas14] L. Gastaldo et al., *The Electron Capture ^{163}Ho Experiment ECHo*, Journal of Low Temperature Physics **176**, 5-6 (2014) 876–884.
- [Gro15] S. Groh, *Modeling of the response function and measurement of transmission properties of the KATRIN experiment*, Phd thesis, Karlsruhe Institute of Technology (2015).
- [Hig64] P. W. Higgs, *Broken Symmetries and the Masses of Gauge Bosons*, Physical Review Letters **13**, 16 (1964) 508–509.
- [Hoe12] M. Hoetzel, *Simulation and Analysis of Source-related Effects for KATRIN*, Phd thesis, Karlsruhe Institute of Technology (2012).
- [Jan15] A. Jansen, *The Cryogenic Pumping Section of the KATRIN Experiment - Design Studies and Experiments for the Commissioning*, Phd thesis, Karlsruhe Institute of Technology (2015).
- [Kae12] W. Kaefer, *Sensitivity studies of the KATRIN experiment*, Phd thesis, Karlsruhe Institute of Technology (2012).
- [KC05] KATRIN-Collaboration, *KATRIN Design Report*, FZKA Scientific Report 7090 (2005).
- [Kle14] M. Kleesiek, *A Data-Analysis and Sensitivity-Optimization Framework for the KATRIN Experiment*, Phd thesis, Karlsruhe Institute of Technology (2014).
- [Kod01] K. Kodama et al., *Observation of tau neutrino interactions*, Physics Letters B **504**, 3 (2001) 218–224.
- [Kom11] E. Komatsu et al., *Seven-Year Wilkinson Microwave Anisotropy Probe (WMAP) Observations: Cosmological Interpretation*, The Astrophysical Journal Supplement Series **192**, 2 (2011) 18.
- [Kra05] C. Kraus et al., *Final results from phase II of the Mainz neutrino mass search in tritium β decay*, The European Physical Journal C **40**, 4 (2005) 447–468.
- [Kra11] C. Kranz, *Optimierung der Methoden und Messprozeduren zur Entfaltung der Energieverlustfunktion beim KATRIN-Experiment*, Diploma thesis, Karlsruhe Institute of Technology (2011).
- [LEP06] LEP Electroweak Working Group et al., *Precision Electroweak Measurements on the Z Resonance*, Phys. Rept. **427** (2006).

- [Les06] J. Lesgourgues et al., *Massive neutrinos and cosmology*, Physics Reports **429**, 6 (2006) 307–379.
- [Liu94] J. Liu et al., *Dissociative cross sections of H₂ by electron impact*, Physical Review A **50**, 4 (1994) 3181–3185.
- [Luk12] S. Lukić et al., *Measurement of the gas-flow reduction factor of the KATRIN DPS2-F differential pumping section*, Vacuum **86**, 8 (2012) 1126–1133.
- [Mac05] H. Machner, *Einführung in die Kern- und Elementarteilchenphysik*, WILEY-VCH, Weinheim, first edition (2005).
- [Mak62] Z. Maki et al., *Remarks on the Unified Model of Elementary Particles*, Progress of Theoretical Physics **28**, 5 (1962) 870–880.
- [Mon06] A. Monfardini et al., *The microcalorimeter arrays for a rhenium experiment (MARE): A next-generation calorimetric neutrino mass experiment*, Nuclear Instruments and Methods in Physics Research Section A: Accelerators, Spectrometers, Detectors and Associated Equipment **559**, 2 (2006) 346–348.
- [Mon09] B. Monreal et al., *Relativistic cyclotron radiation detection of tritium decay electrons as a new technique for measuring the neutrino mass*, Physical Review D **80**, 5 (2009) 051301.
- [Mon15] B. Monreal et al., *UCSB EGun testing summary*, KATRIN Internal Report (2015).
- [Nis85] H. Nishimura et al., *Differential Cross Sections of Electron Scattering from Molecular Hydrogen I. Elastic Scattering and Vibrational Excitation ($X^1\Sigma_g^+$, $v = 0 \rightarrow 1$)*, Journal of the Physical Society of Japan **54**, 5 (1985) 1757–1768.
- [Pau30] W. Pauli, *Offener Brief an die Gruppe der Radioaktiven bei der Gauvereins-Tagung zu Tübingen*, in R. Kronig et al., editors, *Collected scientific papers*, Interscience, New York (1964), second edition (1930).
- [Pla13] Planck Collaboration, *Planck 2013 results. XVI. Cosmological parameters*, Astronomy & Astrophysics **571**, A16 (2013).
- [Pom14] C. Pommranz, *Implementation and Monte Carlo simulation of the KATRIN response function using Kassiopeia 3.0*, Bachelor thesis, Karlsruhe Institute of Technology (2014).
- [Pon67] B. Pontecorvo, *Neutrino Experiments and the Problem of Conservation of Leptonic Charge (translated)*, Zh. Eksp. Teor. Fiz. **53** (1967) 1717 [Sov. Phys. JETP **26** (1968) 984].
- [Rei56] F. Reines et al., *The neutrino*, Nature **178**, 4531 (1956) 446–449.
- [ROO15] ROOT Development Team, *The ROOT Software Framework* (2015).
- [Rud91] M. Rudd, *Differential and total cross sections for ionization of helium and hydrogen by electrons*, Physical Review A **44**, 3 (1991) 1644–1652.

- [Sch14] J. S. Schwarz, *The Detector System of the KATRIN Experiment - Implementation and First Measurements with the Spectrometer*, Phd thesis, Karlsruhe Institute of Technology (2014).
- [SM15] H. Seitz-Moskaliuk et al., *KATRIN STS: What we need, what we have*, Presentation at the 28th KATRIN Collaboration Meeting (2015).
- [Tra83] S. Trajmar et al., *Electron scattering by molecules II. Experimental methods and data*, Physics Reports **97**, 5 (1983) 219–356.
- [Ull07] T. Ullrich et al., *Treatment of Errors in Efficiency Calculations*, arXiv:physics **0701199v2** (2007).
- [Wen10] R. Wendell et al., *Atmospheric neutrino oscillation analysis with subleading effects in Super-Kamiokande I, II, and III*, Physical Review D **81**, 9 (2010) 092004.
- [Wil87] J. Wilkerson et al., *Limit on $\bar{\nu}_e$ Mass from Free-Molecular-Tritium Beta Decay*, Physical Review Letters **58**, 20 (1987) 2023–2026.
- [Win11] A. Windberger, *Berechnungen und Simulationen zum Verhalten von Ionen in der differentiellen Pumpstrecke des KATRIN-Experiments*, Diploma thesis, Karlsruhe Institute of Technology (2011).
- [Wol08] I. Wolff, *Entfaltung der Energieverlustfunktion beim KATRIN Experiment*, Diploma thesis, Westfälische Wilhelms-Universität Münster (2008).
- [Zie13] S. Ziegler, *Die Extraktion der Energieverlustfunktion beim KATRIN Experiment*, Diploma thesis, Karlsruhe Institute of Technology (2013).

Appendix

A. Measuring Time Distributions

The following measuring time distributions have been used for the analyses in chapter 5.

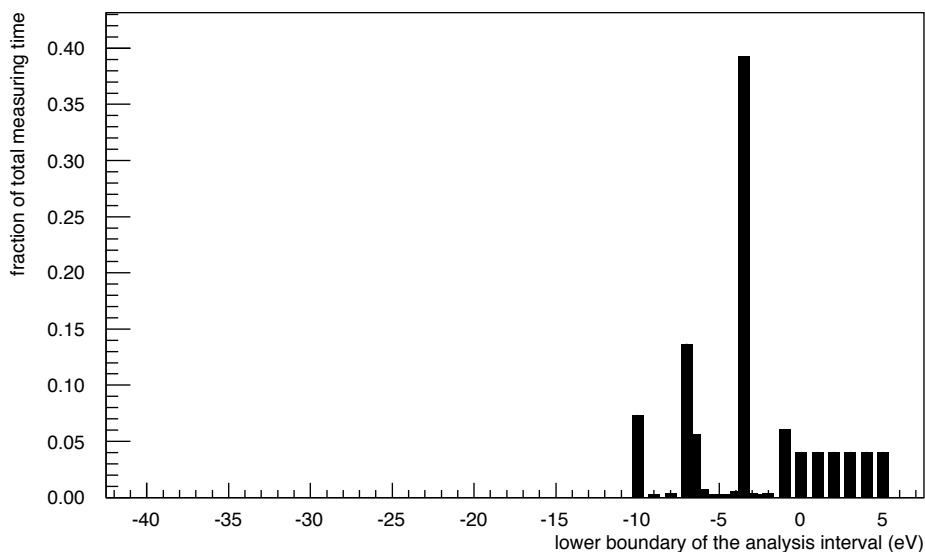


Figure A.1.: **Measuring time distribution optimized for a lower boundary of the analysis interval at -10 eV.** The diagram depicts the distribution of the effective three years of measurement time for a lower boundary of the analysis interval of -10 eV. The four distinct regions to spend most of the available measuring time on (see section 4.2.5) are clearly visible. This measuring time distribution has been optimized according to [Kle14] and has been provided by Dr. Marco Kleesiek.

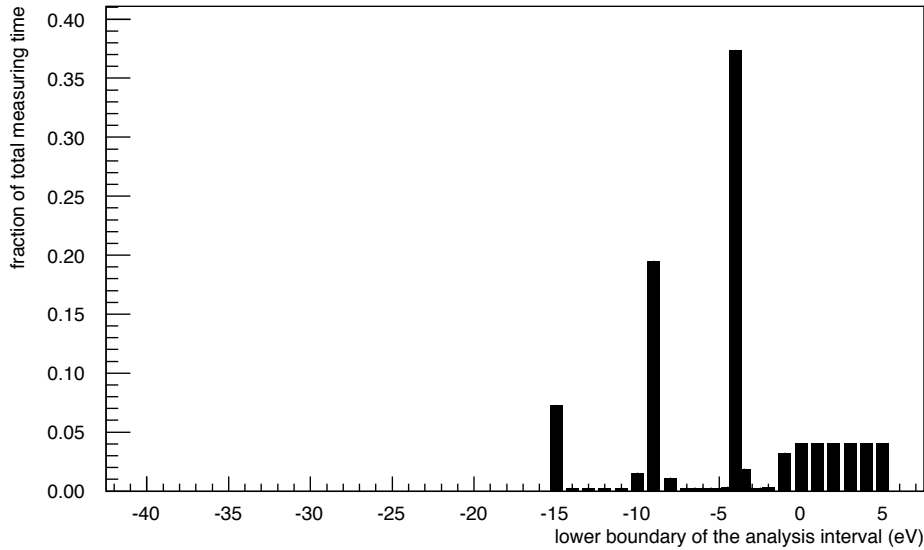


Figure A.2.: **Measuring time distribution optimized for a lower boundary of the analysis interval at -15 eV.** The diagram depicts the distribution of the effective three years of measurement time for a lower boundary of the analysis interval of -15 eV. The four distinct regions to spend most of the available measuring time on (see section 4.2.5) are clearly visible. This measuring time distribution has been optimized according to [Kle14] and has been provided by Dr. Marco Kleesiek.

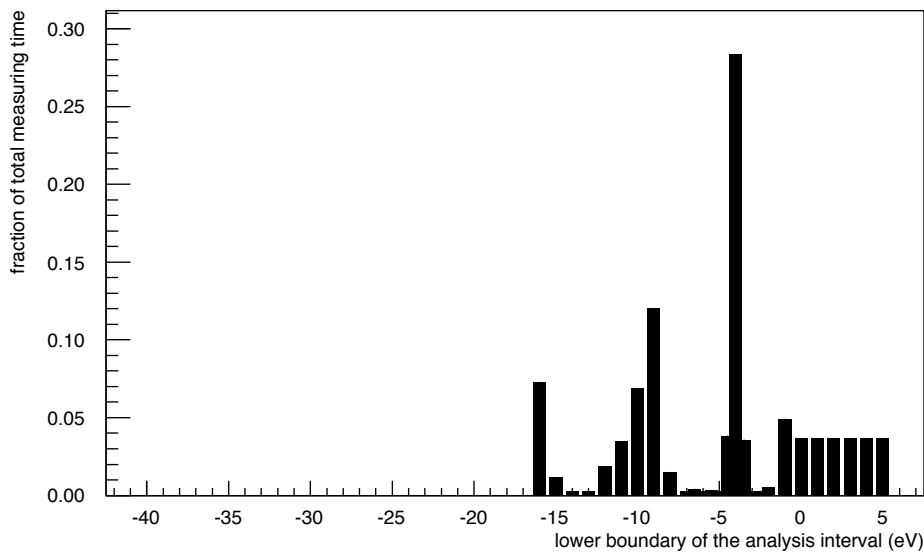


Figure A.3.: **Measuring time distribution optimized for a lower boundary of the analysis interval at -16 eV.** The diagram depicts the distribution of the effective three years of measurement time for a lower boundary of the analysis interval of -16 eV. The four distinct regions to spend most of the available measuring time on (see section 4.2.5) are clearly visible. This measuring time distribution has been optimized according to [Kle14] and has been provided by Dr. Marco Kleesiek.

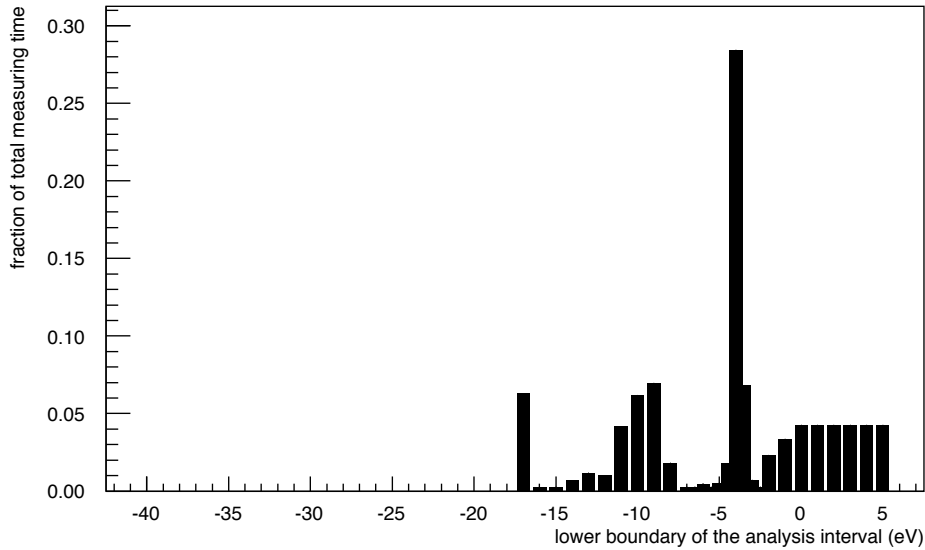


Figure A.4.: **Measuring time distribution optimized for a lower boundary of the analysis interval at -17 eV.** The diagram depicts the distribution of the effective three years of measurement time for a lower boundary of the analysis interval of -17 eV. The four distinct regions to spend most of the available measuring time on (see section 4.2.5) are clearly visible. This measuring time distribution has been optimized according to [Kle14] and has been provided by Dr. Marco Kleesiek.

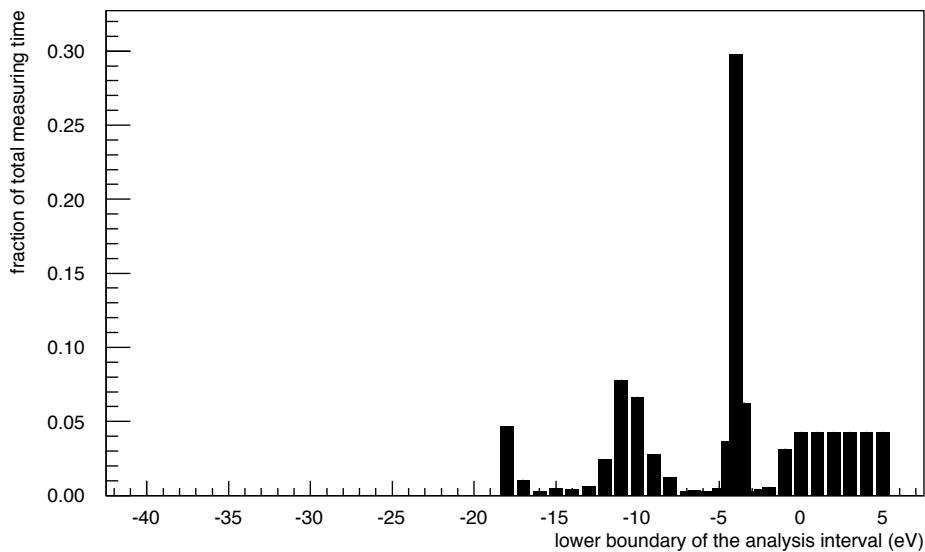


Figure A.5.: **Measuring time distribution optimized for a lower boundary of the analysis interval at -18 eV.** The diagram depicts the distribution of the effective three years of measurement time for a lower boundary of the analysis interval of -18 eV. The four distinct regions to spend most of the available measuring time on (see section 4.2.5) are clearly visible. This measuring time distribution has been optimized according to [Kle14] and has been provided by Dr. Marco Kleesiek.

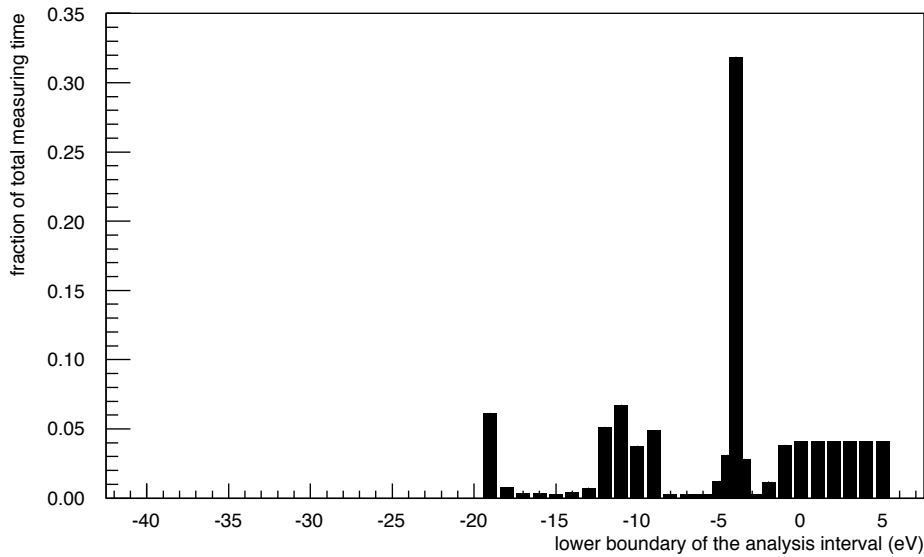


Figure A.6.: **Measuring time distribution optimized for a lower boundary of the analysis interval at -19 eV.** The diagram depicts the distribution of the effective three years of measurement time for a lower boundary of the analysis interval of -19 eV. The four distinct regions to spend most of the available measuring time on (see section 4.2.5) are clearly visible. This measuring time distribution has been optimized according to [Kle14] and has been provided by Dr. Marco Kleesiek.

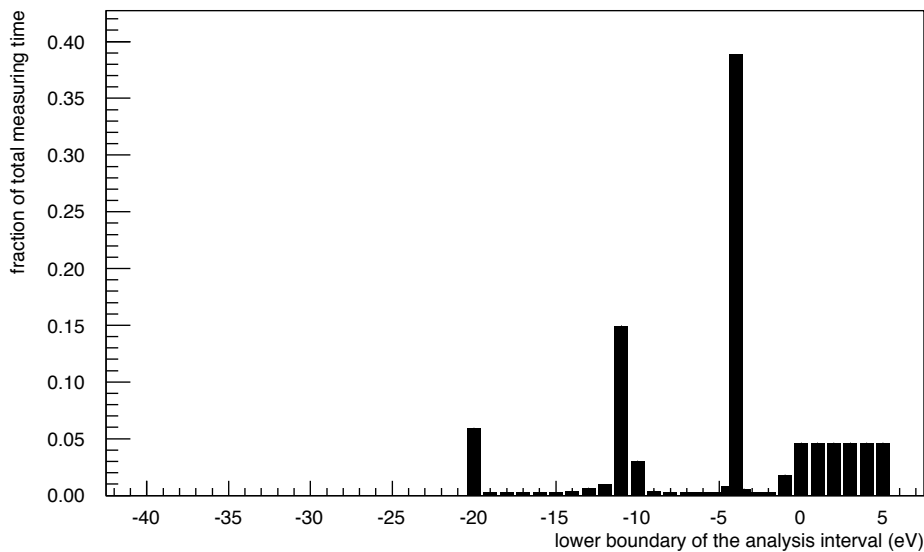


Figure A.7.: **Measuring time distribution optimized for a lower boundary of the analysis interval at -20 eV.** The diagram depicts the distribution of the effective three years of measurement time for a lower boundary of the analysis interval of -20 eV. The four distinct regions to spend most of the available measuring time on (see section 4.2.5) are clearly visible. This measuring time distribution has been optimized according to [Kle14] and has been provided by Dr. Marco Kleesiek.

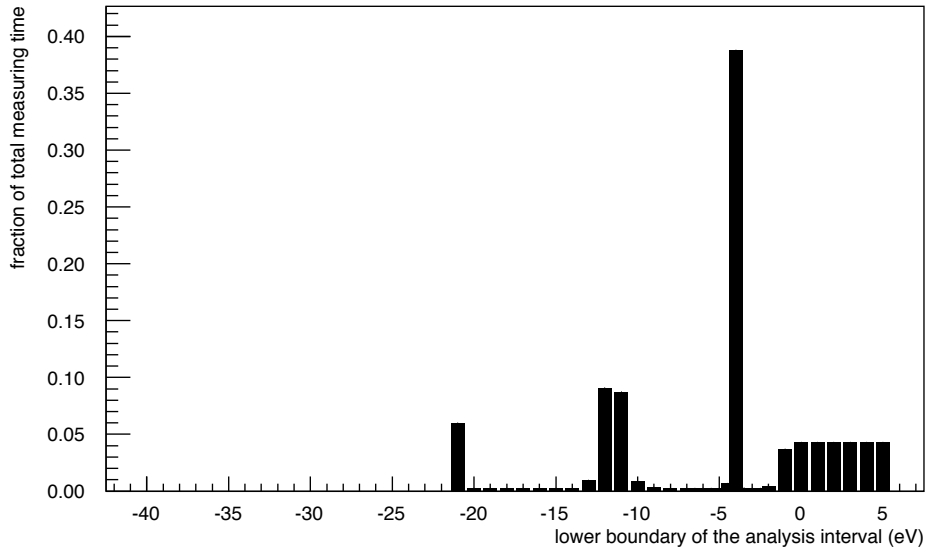


Figure A.8.: **Measuring time distribution optimized for a lower boundary of the analysis interval at -21 eV.** The diagram depicts the distribution of the effective three years of measurement time for a lower boundary of the analysis interval of -21 eV. The four distinct regions to spend most of the available measuring time on (see section 4.2.5) are clearly visible. This measuring time distribution has been optimized according to [Kle14] and has been provided by Dr. Marco Kleesiek.

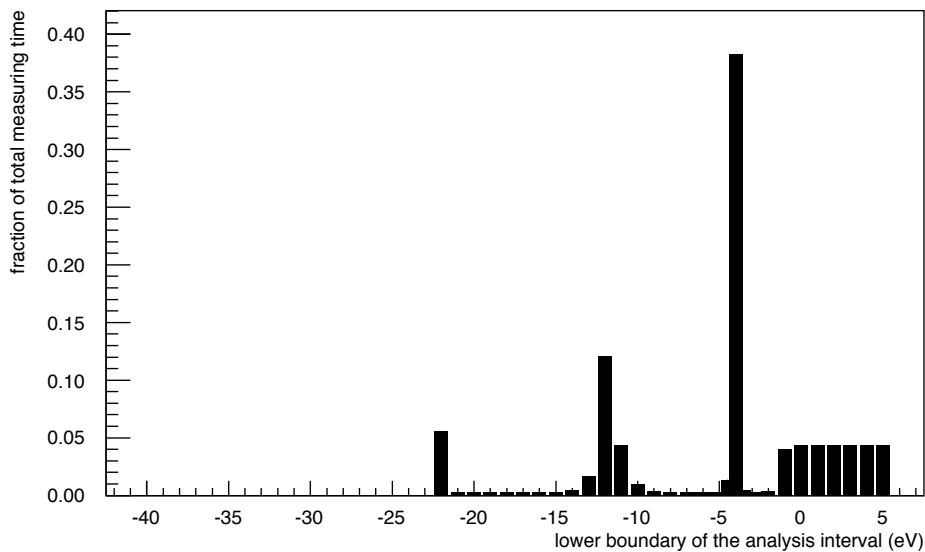


Figure A.9.: **Measuring time distribution optimized for a lower boundary of the analysis interval at -22 eV.** The diagram depicts the distribution of the effective three years of measurement time for a lower boundary of the analysis interval of -22 eV. The four distinct regions to spend most of the available measuring time on (see section 4.2.5) are clearly visible. This measuring time distribution has been optimized according to [Kle14] and has been provided by Dr. Marco Kleesiek.

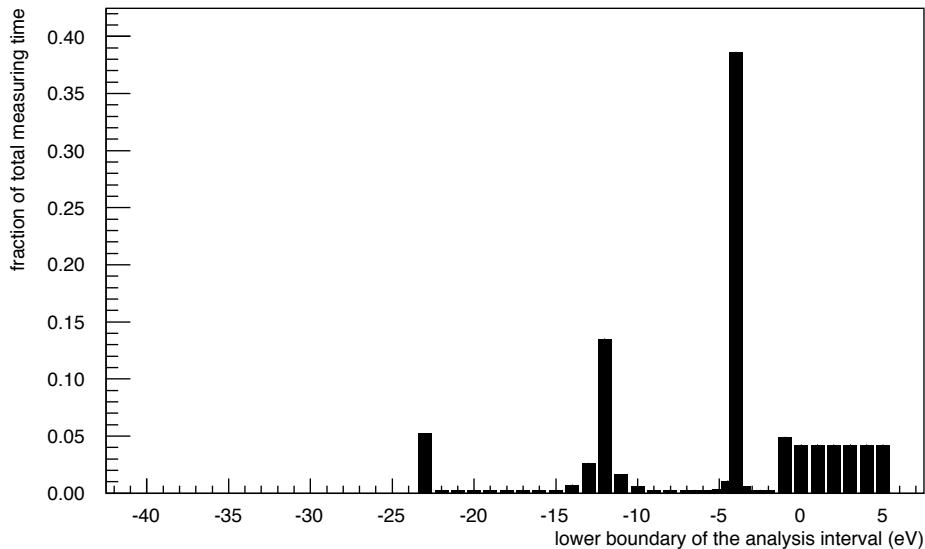


Figure A.10.: **Measuring time distribution optimized for a lower boundary of the analysis interval at -23 eV.** The diagram depicts the distribution of the effective three years of measurement time for a lower boundary of the analysis interval of -23 eV. The four distinct regions to spend most of the available measuring time on (see section 4.2.5) are clearly visible. This measuring time distribution has been optimized according to [Kle14] and has been provided by Dr. Marco Kleesiek.

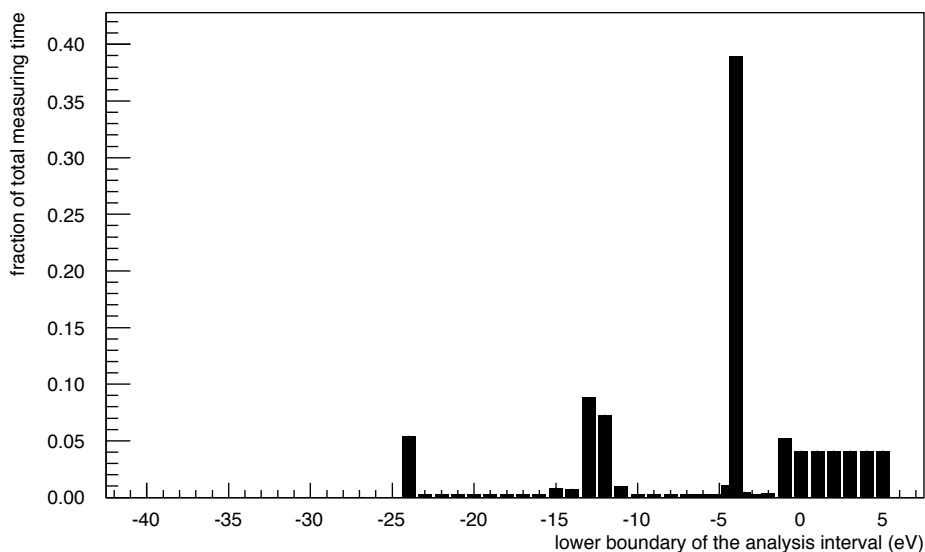


Figure A.11.: **Measuring time distribution optimized for a lower boundary of the analysis interval at -24 eV.** The diagram depicts the distribution of the effective three years of measurement time for a lower boundary of the analysis interval of -24 eV. The four distinct regions to spend most of the available measuring time on (see section 4.2.5) are clearly visible. This measuring time distribution has been optimized according to [Kle14] and has been provided by Dr. Marco Kleesiek.

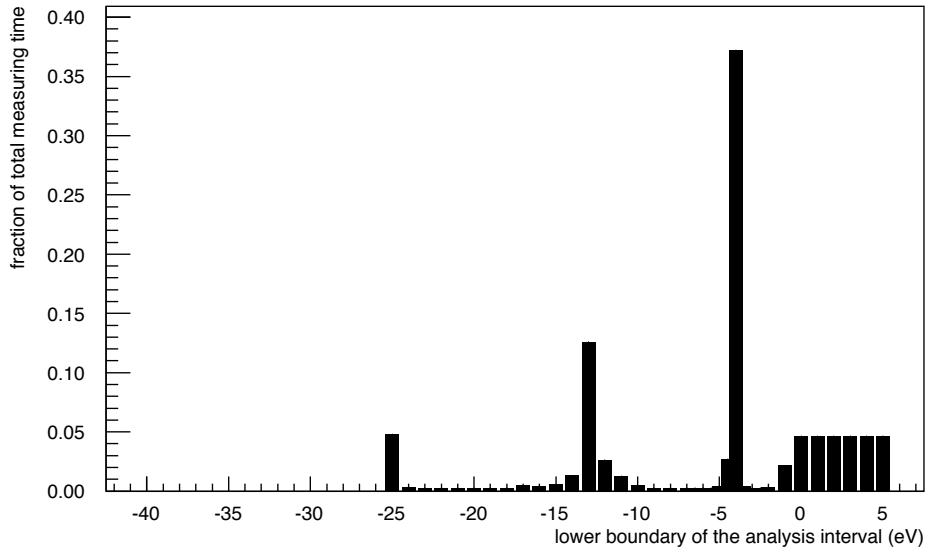


Figure A.12.: **Measuring time distribution optimized for a lower boundary of the analysis interval at -25 eV.** The diagram depicts the distribution of the effective three years of measurement time for a lower boundary of the analysis interval of -25 eV. The four distinct regions to spend most of the available measuring time on (see section 4.2.5) are clearly visible. This measuring time distribution has been optimized according to [Kle14] and has been provided by Dr. Marco Kleesiek.

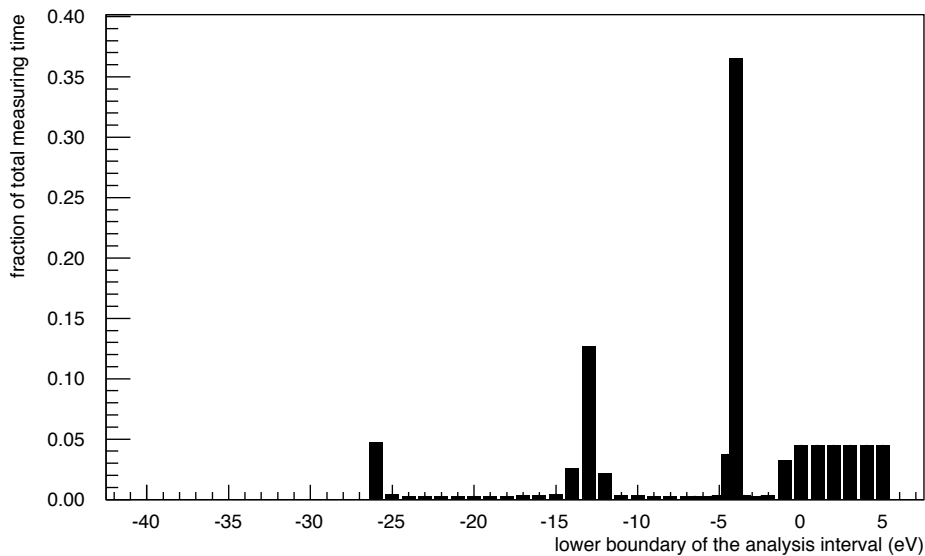


Figure A.13.: **Measuring time distribution optimized for a lower boundary of the analysis interval at -26 eV.** The diagram depicts the distribution of the effective three years of measurement time for a lower boundary of the analysis interval of -26 eV. The four distinct regions to spend most of the available measuring time on (see section 4.2.5) are clearly visible. This measuring time distribution has been optimized according to [Kle14] and has been provided by Dr. Marco Kleesiek.

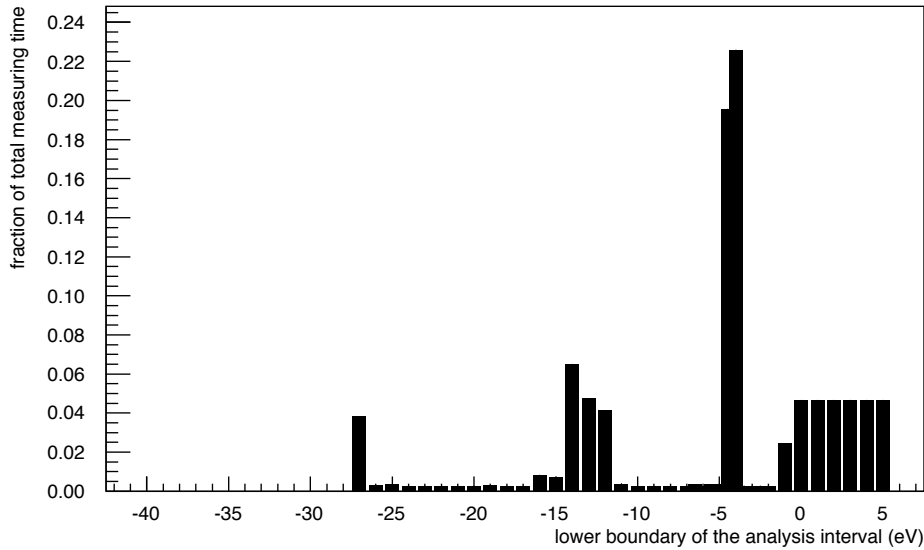


Figure A.14.: **Measuring time distribution optimized for a lower boundary of the analysis interval at -27 eV.** The diagram depicts the distribution of the effective three years of measurement time for a lower boundary of the analysis interval of -27 eV. The four distinct regions to spend most of the available measuring time on (see section 4.2.5) are clearly visible. This measuring time distribution has been optimized according to [Kle14] and has been provided by Dr. Marco Kleesiek.

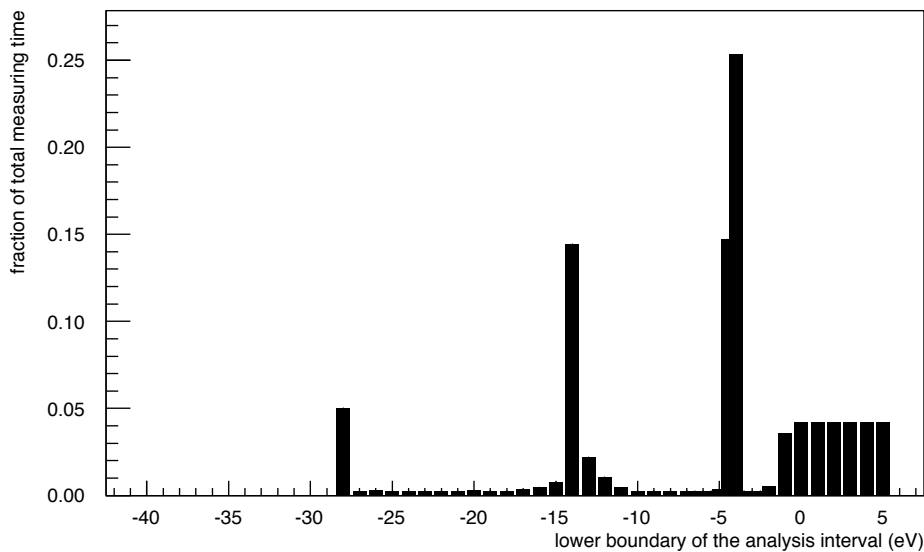


Figure A.15.: **Measuring time distribution optimized for a lower boundary of the analysis interval at -28 eV.** The diagram depicts the distribution of the effective three years of measurement time for a lower boundary of the analysis interval of -28 eV. The four distinct regions to spend most of the available measuring time on (see section 4.2.5) are clearly visible. This measuring time distribution has been optimized according to [Kle14] and has been provided by Dr. Marco Kleesiek.

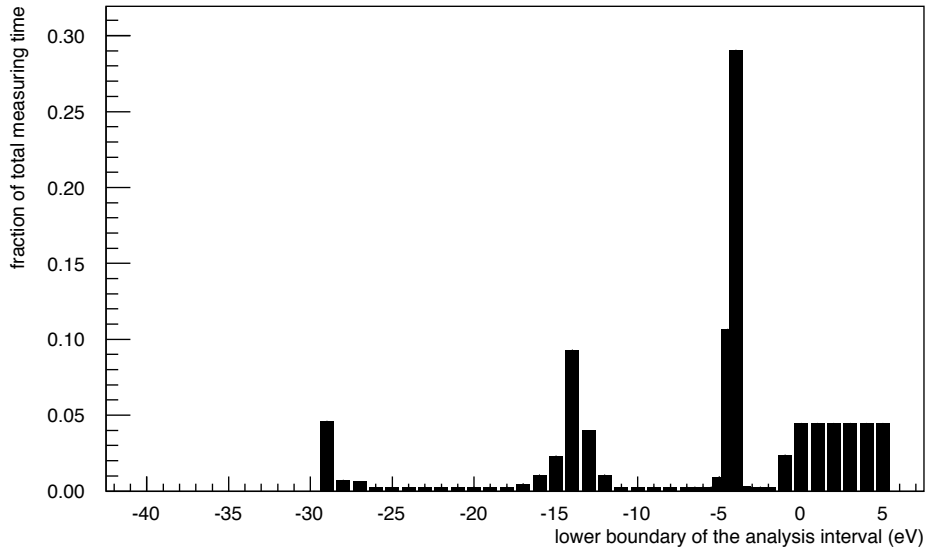


Figure A.16.: **Measuring time distribution optimized for a lower boundary of the analysis interval at -29 eV.** The diagram depicts the distribution of the effective three years of measurement time for a lower boundary of the analysis interval of -29 eV. The four distinct regions to spend most of the available measuring time on (see section 4.2.5) are clearly visible. This measuring time distribution has been optimized according to [Kle14] and has been provided by Dr. Marco Kleesiek.

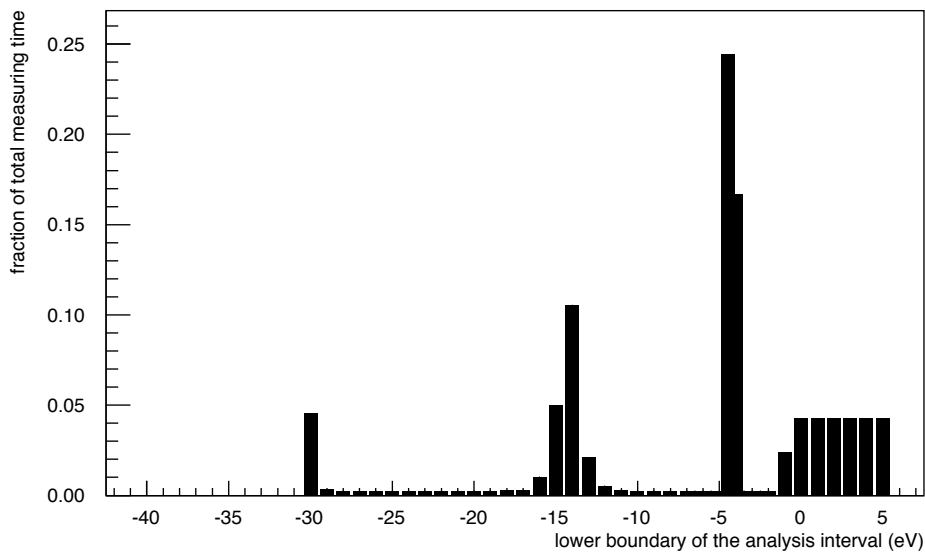


Figure A.17.: **Measuring time distribution optimized for a lower boundary of the analysis interval at -30 eV.** The diagram depicts the distribution of the effective three years of measurement time for a lower boundary of the analysis interval of -30 eV. The four distinct regions to spend most of the available measuring time on (see section 4.2.5) are clearly visible. This measuring time distribution has been optimized according to [Kle14] and has been provided by Dr. Marco Kleesiek.

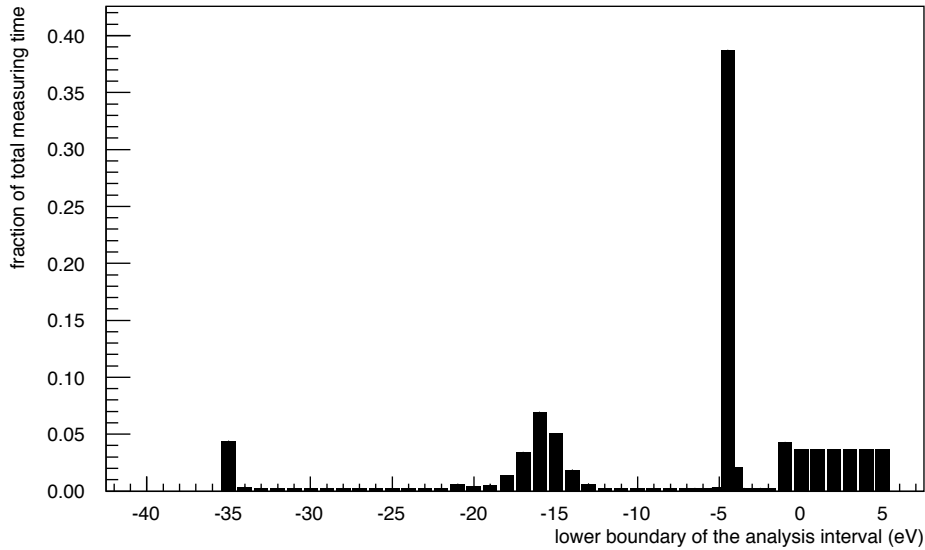


Figure A.18.: **Measuring time distribution optimized for a lower boundary of the analysis interval at -35 eV.** The diagram depicts the distribution of the effective three years of measurement time for a lower boundary of the analysis interval of -35 eV. The four distinct regions to spend most of the available measuring time on (see section 4.2.5) are clearly visible. This measuring time distribution has been optimized according to [Kle14] and has been provided by Dr. Marco Kleesiek.

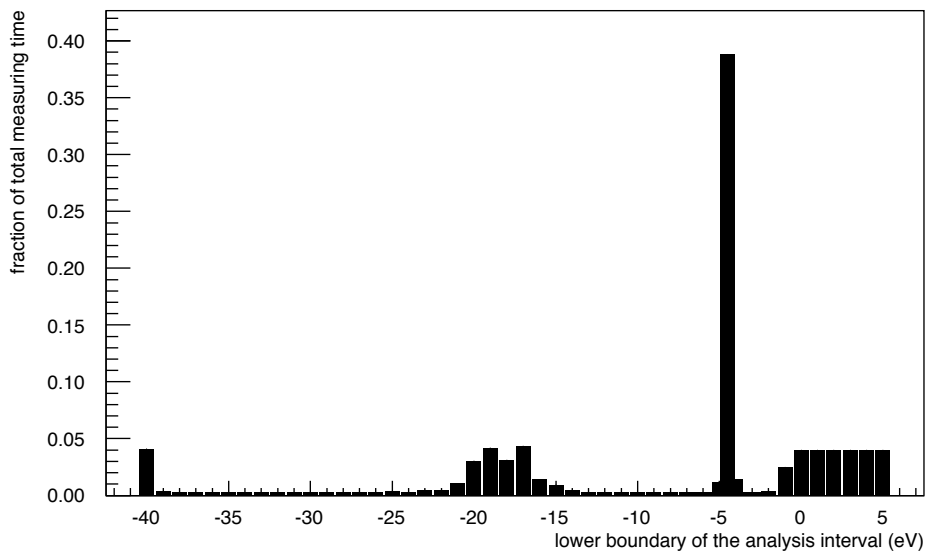


Figure A.19.: **Measuring time distribution optimized for a lower boundary of the analysis interval at -40 eV.** The diagram depicts the distribution of the effective three years of measurement time for a lower boundary of the analysis interval of -40 eV. The four distinct regions to spend most of the available measuring time on (see section 4.2.5) are clearly visible. This measuring time distribution has been optimized according to [Kle14] and has been provided by Dr. Marco Kleesiek.

B. Kassiopia Configuration Files

The following configuration file has been used for the simulations in chapter 6. It is based on the configuration file used by [Gro15] and has been adapted for simulating a Rearsection electron gun.

```
<define name="magnet_sts_path" value="/kalinka/home/antoni-jk/
  workspace/Kasper_globalthesis/install/config/Kassiopia/./
  TheBag/MagnetSTS"/>
<define name="magnet_sds_path" value="/kalinka/home/antoni-jk/
  workspace/Kasper_globalthesis/install/config/Kassiopia/./
  TheBag/MagnetSDS"/>
<define name="global_path" value="/kalinka/home/antoni-jk/workspace
  /Kasper_globalthesis/install/config/Kassiopia/./TheBag/
  AxialGlobal"/>
<define name="axial_pre_spec_path" value="/kalinka/home/antoni-jk/
  workspace/Kasper_globalthesis/install/config/Kassiopia/./
  TheBag/AxialPreSpec"/>
<define name="axial_main_spec_path" value="/kalinka/home/antoni-jk/
  workspace/Kasper_globalthesis/install/config/Kassiopia/./
  TheBag/AxialMainSpec"/>
<define name="axial_detector_path" value="/kalinka/home/antoni-jk/
  workspace/Kasper_globalthesis/install/config/Kassiopia/./
  TheBag/AxialDetector"/>

<external_define name="output_path" value="/kalinka/home/antoni-jk/
  workspace/Kasper_globalthesis/install/output/Kassiopia"/>
<external_define name="output_base" value="GlobalSimulation.root"/>
<external_define name="log_path" value="/kalinka/home/antoni-jk/
  workspace/Kasper_globalthesis/install/output/Kassiopia"/>
<external_define name="log_base" value="LogGlobalSimulation.txt"/>

<external_define name="events" value="100"/>
<external_define name="seed" value="123"/>
<external_define name="energyEGun" value="18600."/>
<external_define name="SigmaEnergyEGun" value=".07"/>
<external_define name="thetaEGun" value="1.8"/>
<external_define name="sigmaThetaEGun" value="0.73"/>
<external_define name="ColumnDensity" value="5E21"/>
<external_define name="inelastic_crosssection" value="3.40E-22"/>

<!-- define verbosity level of messages -->
<messages>

  <file path="[log_path]" base="[log_base]"/>

  <message key="k_file" terminal="normal" log="warning"/>
  <message key="k_initialization" terminal="normal" log="warning"
    />

  <message key="kg_core" terminal="normal" log="warning"/>
  <message key="kg_shape" terminal="normal" log="warning"/>
  <message key="kg_mesh" terminal="normal" log="warning"/>
  <message key="kg_axial_mesh" terminal="normal" log="warning"/>
  <message key="kg_vis" terminal="normal" log="warning"/>

  <message key="ks_object" terminal="normal" log="normal"/>
  <message key="ks_operator" terminal="normal" log="normal"/>
  <message key="ks_field" terminal="normal" log="normal"/>
```



```

<external_define name="steep_cone_additional_offset" value="0"/>

<!-- include geometry files of magnets and electrodes -->
<include name="[magnet_sts_path]/MagnetSTSMoel.xml"/>
<include name="[magnet_sds_path]/MagnetSDSMoel.xml"/>

<include name="[axial_main_spec_path]/AxialMainSpecMoel.xml"/>
<include name="[axial_detector_path]/AxialDetectorMoel.xml"/>
<include name="[axial_pre_spec_path]/AxialPreSpecMoel.xml"/>
<include name="[global_path]/AxialGlobalMoel.xml"/>

<!-- put together geometry -->
<geometry>
  <!-- define a world space, and put spectrometer and
  detector inside -->
  <cylinder_space name="world_space" z1="-50" z2="50" r="20"/>

  <cylinder_space name="transport_space" z1="-45" z2="-16.2" r="
  10"/>
  <cylinder_space name="pre_spec_space" z1="-1.75" z2="1.75" r="1
  "/>
  <cylinder_space name="main_spec_space" z1="-11.6" z2="11.6" r="
  5"/>
  <cylinder_space name="pae_space" z1="12.8" z2="13.3" r="1"/>

  <cylinder_space name="wgts_space" z1="-5.0" z2="5.0" r="0.075"
  /> <!-- increased artificially from 0.045, because of big
  flux at end -->

  <space name="world" node="world_space">
    <space name="magnet_sts" tree="magnet_sts_assembly"/>
    <space name="magnet_sds" tree="magnet_sds_assembly"/>

    <space name="axial_pre_spec" tree="axial_pre_spec_assembly"
    >
      <transformation displacement="0. 0. -14.28375"/>
    </space>

    <space name="pre_spec" node="pre_spec_space">
      <transformation displacement="0. 0. -14.28375"/>
    </space>

    <space name="axial_main_spec" tree="
    axial_main_spec_assembly"/>

    <space name="main_spec" node="main_spec_space"/>

    <space name="axial_detector" tree="axial_detector_assembly"
    />

    <space name="pae" node="pae_space"/>

    <space name="transport_section" node="transport_space">
      <space name="wgts" node="wgts_space">
        <transformation displacement="0. 0. -38.871
        "/>
      </space>
    </space>
  </space>

```

```

        <space name="axial_global" tree="axial_global_assembly"/>
    </space>
</geometry>
<kassiopeia>
    <!-- fields -->
    <ksfield_electromagnet
        name="field_magnets_global"
        file="MagnetGlobalMagnets.kbd"
        system="world/magnet_sds"
        spaces="world/magnet_sts/@magnet_tag"
        spaces="world/magnet_sds/@magnet_tag"
    >
        <zonal_harmonic_field_solver
            number_of_bifurcations="-1"
            convergence_ratio=".99"
            convergence_parameter="1.e-15"
            proximity_to_sourcepoint="1.e-12"
            number_of_central_coefficients="500"
            use_fractional_central_sourcepoint_spacing="true"
            central_sourcepoint_fractional_distance="1.e-2"
            central_sourcepoint_spacing="1.e-3"
            number_of_remote_coefficients="200"
        />
    </ksfield_electromagnet>
    <ksfield_electrostatic
        name="field_axial_global"
        file="AxialGlobalElectrodes.kbd"
        system="world"
        surfaces="world/axial_main_spec/@electrode_tag"
        surfaces="world/axial_pre_spec/@electrode_tag"
        surfaces="world/axial_detector/@electrode_tag"
        surfaces="world/axial_global/@beam_tube_tag"
        symmetry="axial"
    >
        <robin_hood_bem_solver
            tolerance="1.e-8"
            check_sub_interval="100"
            display_interval="1"
            cache_matrix_elements="true"
        />
        <zonal_harmonic_field_solver
            number_of_bifurcations="-1"
            convergence_ratio=".99"
            convergence_parameter="1.e-15"
            proximity_to_sourcepoint="1.e-12"
            number_of_central_coefficients="500"
            use_fractional_central_sourcepoint_spacing="true"
            central_sourcepoint_fractional_distance="1.e-2"
            central_sourcepoint_spacing="1.e-2"
            number_of_remote_coefficients="200"
        />
    </ksfield_electrostatic>

```

```

        <!-- constant 3.6 T field, faster than real wgts magnetic
            field -->
<ksfield_magnetic_constant name="wgts_constant" field="0_0_0-3.6
"/>

<!-- earth magnetic field -->
<ksfield_magnetic_constant name="earth_magnetic_field_z" field=
"0_0_0_200.e-7"/>

</kassiopeia>

<ssc>
    <!-- SSC -->
    <SSCTemperature1D
        Name="Temperature1D"
        T0="30."
        DeltaT="0"
    />

    <SSCDensity1D
        Name="Density1D"
        TemperatureName="Temperature1D"
        ColumnDensity="[ColumnDensity]"
        RatioP="0.04"
        CalculateDensity="ColumnDensity"
    />

    <SSCGasDynamics1D
        Name="GasDynamicsCalculator"
        TemperatureName="Temperature1D"
        DensityName="Density1D"
    />

    <SSCWGTS
        Name="WGTS1"
        MagfieldName="field_magnets_global"
        GasDynamicsName="GasDynamicsCalculator"
        BeamtubeRadius="0.045"
        NSlices="100" NRings="13" NSegments="1" NCenterSegments="1"
        SegmentationType="detector"
        Flux="0.0191"
    />

    <SSCElossAseev
        Name="myElossAseev"
        NConvolutions="0"
        NSteps="3000"
        StepWidth="0.1" />

</ssc>

<kassiopeia>
    <!-- generators -->

    <ksgen_generator_composite name="eGun_generator">

        <energy_composite>

```

```

        <energy_gauss value_mean="[energyEGun]" value_sigma="[
SigmaEnergyEGun]"/>
    </energy_composite>

    <direction_spherical_composite>
        <theta_gauss value_mean="[thetaEGun]" value_sigma="[
sigmaThetaEGun]"/>
        <phi_uniform value_min="0." value_max="360."/>
    </direction_spherical_composite>

    <position_cylindrical_composite>
        <r_fix value="0."/>
        <z_fix value="-43.871"/> <!-- Beginning of
            WGTS -->
        <phi_fix value="0."/>
    </position_cylindrical_composite>

    <time_composite>
        <time_fix value="0."/>
    </time_composite>

</ksgen_generator_composite>

<ksgen_generator_composite name="wgts_generator">
    <!-- energy creation -->
    <energy_composite>
        <!-- U_AP (r=0) = -18544.14198 -->
        <energy_uniform value_min="18544" value_max="18575"/>
        <!--energy_uniform value_min="18544" value_max="18546"/
            -->
        <!--energy_fix value="18601"/-->
    </energy_composite>

    <position_ssc name="position_ssc" wgts_name="WGTS1"
        use_only_axis="false"/>

    <!-- direction creation -->
    <direction_spherical_composite>
        <!--theta_spherical angle_min="0." angle_max="50.77"/
-->
        <theta_spherical angle_min="0." angle_max="60.00"/>
        <!--theta_fix value="0."/-->
        <phi_uniform value_min="0." value_max="360."/>
    </direction_spherical_composite>

    <!-- time creation (not used here) -->
    <time_composite>
        <time_fix value="0."/>
    </time_composite>
</ksgen_generator_composite>

<ksgen_generator_composite name="fix_generator">
    <!-- energy creation -->
    <energy_composite>
        <energy_fix value="18575"/>
    </energy_composite>

    <!--position_flux_tube flux="0.0191" only_surface="true">
        <phi_uniform value_min="0.0" value_max="359"/>

```

```

    <z_fix value="-38.5"/>
  </position_flux_tube-->

<position_cylindrical_composite>
  <r_fix value="0.00"/>
  <phi_fix value="90.0"/>
  <z_fix value="-38.8"/>
</position_cylindrical_composite>

<!-- direction creation -->
<direction_spherical_composite>
  <theta_fix value="50."/>
  <phi_fix value="0."/>
</direction_spherical_composite>

<!-- time creation (not used here) -->
<time_composite>
  <time_fix value="0."/>
</time_composite>
</ksgen_generator_composite>

<ksgen_generator_composite name="fpd_generator">
  <energy_composite>
    <energy_fix value="18600."/>
  </energy_composite>
  <position_cylindrical_composite surface="world/
    axial_detector/axial_detector_preassembly/PAE_assembly/
    flange/silicon/bottom">
    <r_fpd_wafer_set use_ring_centers="false"/>
    <phi_set value_start="0." value_stop="180." value_count
      ="2"/>
    <z_fix value="1.264943"/>
  </position_cylindrical_composite>
  <direction_spherical_composite surface="world/
    axial_detector/axial_detector_preassembly/PAE_assembly/
    flange/silicon/bottom">
    <theta_fix value="0."/>
    <phi_fix value="0."/>
  </direction_spherical_composite>
  <time_composite>
    <time_fix value="0."/>
  </time_composite>
</ksgen_generator_composite>

<!-- trajectories -->

  <!-- exact trajectory -->
<kstraj_trajectory_exact name="trajectory_exact">
  <integrator_rk8 name="integrator_rk8"/>
  <term_propagation name="term_propagation"/>
  <control_cyclotron name="control_cyclotron" fraction="{1.□/
    □32.}">
</kstraj_trajectory_exact>

<!-- adiabatic trajectory -->
<kstraj_trajectory_adiabatic name="trajectory_adiabatic">
  <integrator_rk8 name="integrator_rk8"/>
  <term_propagation name="term_propagation"/>
  <term_drift name="term_drift"/>

```

```

    <term_gyration name="term_gyration"/>
</kstraj_trajectory_adiabatic>

<kstraj_term_synchrotron name="synchrotron"/>

<kstraj_control_cyclotron name="control_cyclotron_1_4" fraction
="{1.0/4.0}"/>
<kstraj_control_cyclotron name="control_cyclotron_1_2" fraction
="{1.0/2.0}"/>
<kstraj_control_cyclotron name="control_cyclotron_1" fraction="
{1.0/1.0}"/>
<kstraj_control_cyclotron name="control_cyclotron_2" fraction="
{2.0/1.0}"/>
<kstraj_control_cyclotron name="control_cyclotron_4" fraction="
{4.0/1.0}"/>
<kstraj_control_cyclotron name="control_cyclotron_8" fraction="
{8.0/1.0}"/>
<kstraj_control_cyclotron name="control_cyclotron_16" fraction="
"{16.0/1.0}"/>
<kstraj_control_cyclotron name="control_cyclotron_20" fraction="
"{20.0/1.0}"/>
<kstraj_control_cyclotron name="control_cyclotron_32" fraction="
"{32.0/1.0}"/>

<kstraj_trajectory_magnetic name="trajectory_magnetic">
  <integrator_rk8 name="integrator_rk8"/>
  <term_propagation name="term_propagation" direction="
backward"/>
  <control_time name="control_time" time="1.e-2"/>
</kstraj_trajectory_magnetic>

<!-- interactions -->
  <ksint_calculator_tritium_endpoint name="
tritium_endpoint_calculator" inelastic_crosssection="[
inelastic_crosssection]" eloss="myElossAseev"/>

<ksint_scattering name="hydrogen_scattering" calculator="
tritium_endpoint_calculator">
  <calculator_hydrogen name="hydrogen_calculators" elastic="
true" excitation="false" ionisation="false" molecule="
tritium"/>
</ksint_scattering>

<ksint_density_calculator_ssc name="wgts_density" wgts="WGTS1"
/>
<ksint_density_constant name="zero_density" density="0.0"/>

<!-- navigators -->
<ksnav_space name="nav_space" tolerance="{1.e-3}"/>
<ksnav_surface name="nav_surface"/>

<!-- terminators -->
  <ksterm_max_z name="term_max_z" z="-30."/> <!-- wafer at
13.925841 -->
  <ksterm_min_z name="term_min_z" z="-48.0"/>
  <ksterm_death name="term_front_death"/>
  <ksterm_death name="term_rear_death"/>
  <ksterm_death name="term_wgts_tube_death"/>
  <ksterm_death name="term_detector_death"/>

```

```

<ksterm_death name="term_world_death"/>
<ksterm_trapped name="term_trapped" max_turns="1"/>
<ksterm_max_r name="term_max_r" r="0.045"/>
<ksterm_secondaries name="term_kill_secondaries"/>
  <ksterm_max_steps name="term_max_steps" steps="{1e6}"/>
  <ksterm_min_energy name="term_min_energy" energy="18540"/>

<!-- writers -->
<!-- define a root writer for the data -->
<kswrite_root name="write_root" path="[output_path]" base="[
  output_base]"/>

<!-- output -->
<!-- output of step level -->
<!-- special scattering output -->

<ks_component_member name="output_step_final_particle" field="
  final_particle" parent="step"/>

<ks_component_group name="output_step_world">
  <component_member name="step_id" field="step_id" parent="
    step"/>
  <component_member name="time" field="time" parent="
    output_step_final_particle"/>
  <component_member name="position" field="position" parent="
    output_step_final_particle"/>
  <component_member name="momentum" field="momentum" parent="
    output_step_final_particle"/>
  <component_member name="magnetic_field" field="
    magnetic_field" parent="output_step_final_particle"/>
  <component_member name="electric_potential" field="
    electric_potential" parent="output_step_final_particle"
  />
  <component_member name="kinetic_energy" field="
    kinetic_energy_ev" parent="output_step_final_particle"/>
  <component_member name="polar_angle_to_b" field="
    polar_angle_to_b" parent="output_step_final_particle"/>
</ks_component_group>

  <!-- output of track level -->
<ks_component_member name="output_track_initial_particle" field="
  initial_particle" parent="track"/>
<ks_component_member name="output_track_final_particle" field="
  final_particle" parent="track"/>
<ks_component_member name="initial_position" field="position"
  parent="output_track_initial_particle"/>

<ks_component_group name="output_track_world">
  <component_member name="track_id" field="track_id" parent="
    track"/>
  <component_member name="creator_name" field="creator_name"
    parent="track"/>
  <component_member name="terminator_name" field="
    terminator_name" parent="track"/>
  <component_member name="total_steps" field="total_steps"
    parent="track"/>
  <component_member name="track_energy_loss" field="
    discrete_energy_change" parent="track"/>

```

```

<component_member name="initial_time" field="time" parent="
  output_track_initial_particle"/>
<component_member name="initial_position" field="position"
  parent="output_track_initial_particle"/>
<component_member name="initial_radius" field="perp" parent
  ="initial_position"/>
<component_member name="initial_momentum" field="momentum"
  parent="output_track_initial_particle"/>
<component_member name="initial_magnetic_field" field="
  magnetic_field" parent="output_track_initial_particle"/>
<component_member name="initial_electric_potential" field="
  electric_potential" parent="
  output_track_initial_particle"/>
<component_member name="initial_kinetic_energy" field="
  kinetic_energy_ev" parent="output_track_initial_particle
  "/>
<component_member name="initial_azimuthal_angle_to_x" field
  ="azimuthal_angle_to_x" parent="
  output_track_initial_particle"/>
<component_member name="initial_polar_angle_to_b" field="
  polar_angle_to_b" parent="output_track_initial_particle"
  />
<component_member name="final_time" field="time" parent="
  output_track_final_particle"/>
<component_member name="final_position" field="position"
  parent="output_track_final_particle"/>
<component_member name="final_momentum" field="momentum"
  parent="output_track_final_particle"/>
<component_member name="final_magnetic_field" field="
  magnetic_field" parent="output_track_final_particle"/>
<component_member name="final_electric_potential" field="
  electric_potential" parent="output_track_final_particle"
  />
<component_member name="final_kinetic_energy" field="
  kinetic_energy_ev" parent="output_track_final_particle"
  />
<component_member name="final_azimuthal_angle_to_x" field="
  azimuthal_angle_to_x" parent="
  output_track_final_particle"/>
<component_member name="final_polar_angle_to_b" field="
  polar_angle_to_b" parent="output_track_final_particle"/>
</ks_component_group>

<ks_component_group name="output_track_mc">
  <component_member name="creator_name" field="creator_name"
    parent="track"/>
  <component_member name="terminator_name" field="
    terminator_name" parent="track"/>
  <component_member name="track_energy_loss" field="
    discrete_energy_change" parent="track"/>
  <component_member name="initial_position" field="position"
    parent="output_track_initial_particle"/>
  <component_member name="initial_magnetic_field" field="
    magnetic_field" parent="output_track_initial_particle"/>
  <component_member name="initial_electric_potential" field="
    electric_potential" parent="
    output_track_initial_particle"/>
  <component_member name="initial_kinetic_energy" field="
    kinetic_energy_ev" parent="output_track_initial_particle

```

```

    />
    <component_member name="initial_polar_angle_to_b" field="
      polar_angle_to_b" parent="output_track_initial_particle"
    />
    <component_member name="final_position" field="position"
      parent="output_track_final_particle"/>
    <component_member name="final_magnetic_field" field="
      magnetic_field" parent="output_track_final_particle"/>
    <component_member name="final_electric_potential" field="
      electric_potential" parent="output_track_final_particle"
    />
    <component_member name="final_kinetic_energy" field="
      kinetic_energy_ev" parent="output_track_final_particle"
    />
    <component_member name="final_polar_angle_to_b" field="
      polar_angle_to_b" parent="output_track_final_particle"/>
  </ks_component_group>

<!--
<ks_component_group name="detailed_h2_step_output">
  <!-- number of interactions on step level -->
  <component_member name="step_n_h2_elastic" field="
    step_number_of_interactions" parent="
    hydrogen_calculators_elastic"/>
    <component_member name="step_n_h2_vib" field="
      step_number_of_interactions" parent="
      hydrogen_calculators_vib"/>
    <component_member name="step_n_h2_rot_02" field="
      step_number_of_interactions" parent="
      hydrogen_calculators_rot_02"/>
    <component_member name="step_n_h2_rot_13" field="
      step_number_of_interactions" parent="
      hydrogen_calculators_rot_13"/>
    <component_member name="step_n_h2_rot_20" field="
      step_number_of_interactions" parent="
      hydrogen_calculators_rot_20"/>
    <component_member name="step_n_h2_exc_b" field="
      step_number_of_interactions" parent="
      hydrogen_calculators_exc_b"/>
    <component_member name="step_n_h2_exc_c" field="
      step_number_of_interactions" parent="
      hydrogen_calculators_exc_c"/>
    <component_member name="step_n_h2_diss_10" field="
      step_number_of_interactions" parent="
      hydrogen_calculators_diss_10"/>
    <component_member name="step_n_h2_diss_15" field="
      step_number_of_interactions" parent="
      hydrogen_calculators_diss_15"/>
    <component_member name="step_n_h2_exc_el" field="
      step_number_of_interactions" parent="
      hydrogen_calculators_exc_el"/>
    <component_member name="step_n_h2_ionisation" field="
      step_number_of_interactions" parent="
      hydrogen_calculators_ionisation"/>
  <!-- energy loss on step level -->
  <component_member name="step_elloss_h2_elastic" field="
    step_energy_loss" parent="hydrogen_calculators_elastic"
  />

```

```

    <component_member name="step_eloss_h2_vib" field="
      step_energy_loss" parent="hydrogen_calculators_vib"
    />
    <component_member name="step_eloss_h2_rot_02" field="
      step_energy_loss" parent="
      hydrogen_calculators_rot_02"/>
    <component_member name="step_eloss_h2_rot_13" field="
      step_energy_loss" parent="
      hydrogen_calculators_rot_13"/>
    <component_member name="step_eloss_h2_rot_20" field="
      step_energy_loss" parent="
      hydrogen_calculators_rot_20"/>
    <component_member name="step_eloss_h2_exc_b" field="
      step_energy_loss" parent="hydrogen_calculators_exc_b
    "/>
    <component_member name="step_eloss_h2_exc_c" field="
      step_energy_loss" parent="hydrogen_calculators_exc_c
    "/>
    <component_member name="step_eloss_h2_diss_10" field="
      step_energy_loss" parent="
      hydrogen_calculators_diss_10"/>
    <component_member name="step_eloss_h2_diss_15" field="
      step_energy_loss" parent="
      hydrogen_calculators_diss_15"/>
    <component_member name="step_eloss_h2_exc_el" field="
      step_energy_loss" parent="
      hydrogen_calculators_exc_el"/>
    <component_member name="step_eloss_h2_ionisation" field
      ="step_energy_loss" parent="
      hydrogen_calculators_ionisation"/>
  </ks_component_group>

<ks_component_group name="output_step_h2">
  <!-- summation of all scattering output in elastic,
  excitation and ionisation -->
    <component_math name="step_n_h2_elastic" term="x0+
      x1+x2+x3+x4" group="detailed_h2_step_output"
      component="step_n_h2_elastic" component="
      step_n_h2_vib" component="step_n_h2_rot_02"
      component="step_n_h2_rot_13" component="
      step_n_h2_rot_20"/>
    <component_math name="step_n_h2_excitation" term="
      x0+x1+x2+x3+x4" group="detailed_h2_step_output"
      component="step_n_h2_exc_b" component="
      step_n_h2_exc_c" component="step_n_h2_diss_10"
      component="step_n_h2_diss_15" component="
      step_n_h2_exc_el"/>
    <component_member name="step_n_h2_ionisation" field="
      step_number_of_interactions" parent="
      hydrogen_calculators_ionisation"/>
    <component_math name="step_eloss_h2_elastic" term="
      x0+x1+x2+x3+x4" group="detailed_h2_step_output"
      component="step_eloss_h2_elastic" component="
      step_eloss_h2_vib" component="
      step_eloss_h2_rot_02" component="
      step_eloss_h2_rot_13" component="
      step_eloss_h2_rot_20"/>
    <component_math name="step_eloss_h2_excitation"
      term="x0+x1+x2+x3+x4" group="

```

```

        detailed_h2_step_output" component="
        step_eloss_h2_exc_b" component="
        step_eloss_h2_exc_c" component="
        step_eloss_h2_diss_10" component="
        step_eloss_h2_diss_15" component="
        step_eloss_h2_exc_el"/>
    <component_member name="step_eloss_h2_ionisation" field="
        step_energy_loss" parent="
        hydrogen_calculators_ionisation"/>
</ks_component_group>

<ks_component_group name="output_track_h2">
    <!-- integrate step scattering output -->
    <component_integral name="track_n_h2_elastic" group="
        output_step_h2" component="step_n_h2_elastic"/>
    <component_integral name="track_n_h2_excitation" group="
        output_step_h2" component="step_n_h2_excitation"/>
    <component_integral name="track_n_h2_ionisation" group="
        output_step_h2" component="step_n_h2_ionisation"/>
    <component_integral name="track_eloss_h2_elastic" group="
        output_step_h2" component="step_eloss_h2_elastic"/>
    <component_integral name="track_eloss_h2_excitation" group="
        output_step_h2" component="step_eloss_h2_excitation"/>
    <component_integral name="track_eloss_h2_ionisation" group="
        output_step_h2" component="step_eloss_h2_ionisation"/>
</ks_component_group>
-->

<ks_component_member name="step_n_h2_elastic" field="
    step_number_of_interactions" parent="
    hydrogen_calculators_elastic"/>
<ks_component_member name="step_eloss_h2_elastic" field="
    step_energy_loss" parent="hydrogen_calculators_elastic"/>
<ks_component_member name="step_n_h2_inelastic" field="
    step_number_of_interactions" parent="
    tritium_endpoint_calculator"/>
<ks_component_member name="step_eloss_h2_inelastic" field="
    step_energy_loss" parent="tritium_endpoint_calculator"/>

<ks_component_group name="output_track_h2">
    <!-- integrate step scattering output -->
    <component_integral name="track_n_h2_elastic" component="
        step_n_h2_elastic"/>
    <component_integral name="track_eloss_h2_elastic"
        component="step_eloss_h2_elastic"/>
    <component_integral name="track_n_h2_inelastic" component="
        step_n_h2_inelastic"/>
    <component_integral name="track_eloss_h2_inelastic"
        component="step_eloss_h2_inelastic"/>
</ks_component_group>

<!-- navigation -->
<ksgeo_space name="space_world" spaces="world">
    <command parent="root_trajectory" field="set_trajectory"
        child="trajectory_adiabatic"/>
    <command parent="trajectory_adiabatic" field="add_control"
        child="control_cyclotron_4"/>
    <!--command parent="trajectory_adiabatic" field="add_term"
        child="synchrotron"/-->

```

```

<command parent="root_terminator" field="add_terminator"
  child="term_max_steps"/>
<command parent="root_terminator" field="add_terminator"
  child="term_min_z"/>
<command parent="root_terminator" field="add_terminator"
  child="term_max_z"/>
<command parent="root_terminator" field="add_terminator"
  child="term_trapped"/>
<command parent="root_terminator" field="remove_terminator"
  child="term_world_death"/>

<command parent="root_magnetic_field" field="
  add_magnetic_field" child="earth_magnetic_field_z"/>
<command parent="root_magnetic_field" field="
  add_magnetic_field" child="field_magnets_global"/>
<!-- <command parent="root_electric_field" field="
  add_electric_field" child="field_axial_global"/> -->
<command parent="write_root" field="add_track_output" child
  ="output_track_world"/>
<!-- <command parent="write_root" field="add_step_output"
  child="output_step_world"/> -->

<command parent="root_space_interaction" field="
  add_space_interaction" child="hydrogen_scattering"/>
<command parent="hydrogen_scattering" field="set_density"
  child="zero_density"/>
<command parent="write_root" field="add_track_output" child
  ="output_track_h2"/>

<geo_space name="space_transport" spaces="world/
  transport_section">

  <command parent="trajectory_adiabatic" field="
    remove_control" child="control_cyclotron_4"/>
  <command parent="trajectory_adiabatic" field="
    add_control" child="control_cyclotron_20"/>

  <geo_space name="space_wgts" spaces="world/
    transport_section/wgts">
    <command parent="hydrogen_scattering" field="
      clear_density" child="zero_density"/>
    <command parent="hydrogen_scattering" field="
      set_density" child="wgts_density"/>
    <command parent="root_terminator" field="
      add_terminator" child="
        term_kill_secondaries"/>
    <command parent="root_terminator" field="
      add_terminator" child="term_min_energy"
      />
    <geo_side name="wgts_front" surfaces="world
      /transport_section/wgts/top">
      <command parent="root_terminator"
        field="add_terminator" child="
          term_front_death"/>
    </geo_side>
    <!--geo_side name="wgts_rear" surfaces="
      world/transport_section/wgts/bottom">

```

```

        <command parent="root_terminator"
            field="add_terminator" child="
            term_rear_death"/>
    </geo_side-->
    <geo_side name="wgts_jacket" surfaces="
        world/transport_section/wgts/jacket">
        <command parent="root_terminator"
            field="add_terminator" child="
            term_wgts_tube_death"/>
    </geo_side>
</geo_space>
</geo_space>

<geo_space name="space_prespec" spaces="world/pre_spec">
    <command parent="trajectory_adiabatic" field="
        remove_control" child="control_cyclotron_4"/>
    <command parent="trajectory_adiabatic" field="
        add_control" child="control_cyclotron_1_2"/>
</geo_space>

<geo_space name="space_mainspec" spaces="world/main_spec">
    <command parent="trajectory_adiabatic" field="
        remove_control" child="control_cyclotron_4"/>
    <command parent="trajectory_adiabatic" field="
        add_control" child="control_cyclotron_1_2"/>
</geo_space>

<!--geo_space name="space_pae" spaces="world/pae">
    <command parent="trajectory_adiabatic" field="
        remove_control" child="control_cyclotron_4"/>
    <command parent="trajectory_adiabatic" field="
        add_control" child="control_cyclotron_1"/>
</geo_space-->

<geo_space name="space_silicon" spaces="world/
    axial_detector/axial_detector_preassembly/PAE_assembly/
    flange/silicon">
    <geo_side name="detector_surface" surfaces="world/
        axial_detector/axial_detector_preassembly/
        PAE_assembly/flange/silicon/bottom">
    <command parent="root_terminator" field="
        add_terminator" child="term_detector_death"/>
    </geo_side>
</geo_space>

</ksgeo_space>

<!-- simulation -->

<ks_simulation
    run="1"
    seed="[seed]"
    events="[events]"
    space="space_world"
    generator="eGun_generator"
    space_navigator="nav_space"
    surface_navigator="nav_surface"
    writer="write_root"

```

```

        terminator="term_world_death"
    />

</kassiopeia>
<!--
<root_window
    name="track_plot"
    canvas_width="1000"
    canvas_height="600"
    active="false"
>
    <root_geometryPainter
        name="root_geometryPainter"
        spaces="world/magnet_sds/@magnet_tag"
        spaces="world/magnet_sts/@magnet_tag"
        surfaces="world/transport_section/wgts/jacket"
        surfaces="world/transport_section/wgts/bottom"
        surfaces="world/transport_section/wgts/top"

        surfaces="world/axial_global/@beam_tube_tag"

        surfaces="world/axial_pre_spec/@electrode_tag"
        surfaces="world/axial_main_spec/@electrode_tag"
        surfaces="world/axial_detector/@electrode_tag"
        spaces="world/axial_detector/
            axial_detector_preassembly/PAE_assembly/flange/
            silicon"
        plane_normal="0 1 0"
        plane_point="0 0 0"
        swap_axis="false"
    />

    <root_trackPainter
        name="root_trackPainter"
        base="GlobalSimulation.root"
        x_axis="z"
        y_axis="x"
        step_output_group_name="output_step_world"
        position_name="position"
        color_mode="track"
        track_output_group_name="output_track_world"
        color_variable="initial_radius"
    />

</root_window>
<root_window
    name="detector distribution"
    canvas_width="660"
    canvas_height="600"
>
    <root_fpdPainter
        name="root_fpdPainter"
        base="GlobalSimulation.root"
        track_output_group_name="output_track_world"
        terminator_name="terminator_name"
        terminator_value="term_detector_death"
        final_position_name="final_position"
    />
</root_window> -->

```

Acknowledgments

At the end of this thesis, I would like to thank the KATRIN collaboration for integrating me into their team and for supporting me in writing my thesis. In particular I would like to express my gratitude to

- Prof. Dr. Guido Drexlin for inviting me to join the KATRIN collaboration and for suggesting the interesting scope of this thesis,
- Prof. Dr. Günter Quast for reviewing and evaluating this thesis,
- Dr. Kathrin Valerius for her invitation to join the Young Investigator Group, for advising and supervising me throughout my research and for her efforts in proofreading this thesis,
- Dr. Marco Kleesiek for introducing me to the KATRIN experiment and especially the KASPER framework, for advising and supervising me throughout my research and for his efforts in proofreading this thesis,
- Laura Kuckert for supervising me during my first months at KATRIN and for introducing me to the WGTS,
- Dr. Stefan Groh for his introduction to KASSIOPEIA, for his patient programming support and for his advise on the structure of this thesis,
- Hendrik Seitz-Moskaliuk for sharing my office, for patiently answering all my questions which came up during the writing of this thesis and for proofreading this thesis,
- Dr. Martin Babutzka for his explanations about the Rearsection electron gun, for his KALINKA support and for proofreading this thesis,
- the Young Investigator Group for atmospheric meetings and for input to my research,
- Dr. Johannes Schwarz for his patient support in using ROOT,
- Robert Huber for sharing my office and for his profound advice on bikes,
- Anton Huber for sharing my office and for sharing insights to the political landscape of Wolfartsweier.

Finally, very special thanks goes to my father and mother who enabled me to study physics and who made this thesis even possible. Also special thanks goes to my family, girlfriend and friends who supported me throughout my studies and throughout the writing of this thesis.